

DESIGN ANALYSIS AND STRUCTURAL  
OPTIMISATION OF A RIGID ANKLE FOOT  
ORTHOSIS



MOHD YASHIM WONG PAUL TZE

Master of Science

UNIVERSITI MALAYSIA PAHANG

## UNIVERSITI MALAYSIA PAHANG

### DECLARATION OF THESIS AND COPYRIGHT

Author's Full Name : MOHD YASHIM WONG PAUL TZE

Date of Birth : 21 MARCH 1990

Title : DESIGN ANALYSIS AND STRUCTURAL OPTIMISATION  
OF A RIGID ANKLE FOOT ORTHOSIS

Academic Session : SEM 2 2017/2018

I declare that this thesis is classified as:

- CONFIDENTIAL (Contains confidential information under the Official Secret Act 1997)\*
- RESTRICTED (Contains restricted information as specified by the organization where research was done)\*
- OPEN ACCESS I agree that my thesis to be published as online open access (Full Text)

I acknowledge that Universiti Malaysia Pahang reserves the following rights:

1. The Thesis is the Property of Universiti Malaysia Pahang
2. The Library of Universiti Malaysia Pahang has the right to make copies of the thesis for the purpose of research only.
3. The Library has the right to make copies of the thesis for academic exchange.

Certified by:

\_\_\_\_\_  
(Student's Signature)

\_\_\_\_\_  
(Supervisor's Signature)

\_\_\_\_\_  
MOHD YASHIM WONG PAUL TZE  
Date:

\_\_\_\_\_  
PROF DR ZAHARI BIN TAHA  
Date:

### **SUPERVISOR'S DECLARATION**

I hereby declare that I have checked this thesis and in my opinion, this thesis is adequate in terms of scope and quality for the award of the degree of Master of Science.

---

(Supervisor's Signature)

Full Name : PROF DR ZAHARI BIN TAHA

Position : PROFESSOR

Date :

---

(Co-supervisor's Signature)

Full Name :

Position :

Date :

**UMP**

### **STUDENT'S DECLARATION**

I hereby declare that the work in this thesis is based on my original work except for quotations and citations which have been duly acknowledged. I also declare that it has not been previously or concurrently submitted for any other degree at Universiti Malaysia Pahang or any other institutions.

---

(Student's Signature)

Full Name : MOHD YASHIM WONG PAUL TZE

ID Number : MFM14001

Date :



UMP

DESIGN ANALYSIS AND STRUCTURAL OPTIMISATION OF A RIGID  
ANKLE FOOT ORTHOSIS

The logo of the University of Malaysia Pahang (UMP) is a shield-shaped emblem. It features a central white vertical band with a yellow diamond at the top. The shield is divided into four quadrants: top-left is light blue, top-right is light purple, bottom-left is light purple, and bottom-right is light blue. A stylized, overlapping circular graphic in light blue and purple surrounds the top portion of the shield.

MOHD YASHIM WONG PAUL TZE

Thesis was submitted in fulfillment of the requirements  
for the award of the degree of  
Master of Science

UMP

Faculty of Manufacturing  
UNIVERSITI MALAYSIA PAHANG

AUGUST 2018

## ACKNOWLEDGEMENTS

First and foremost, my gratitude to Allah SWT the Cherisher and Sustainer of worlds, Most Gracious, Most Merciful for His countless blessings which had enabled me to perform this research and to write this thesis to completion. Alhamdulillah.

Deepest gratitude to my supervisor Prof. Dr. Zahari bin Taha for his guidance and continuous support throughout my Masters research. His insight and advice had altered the way I perceive research as well as altered my habits to be the best version of a researcher I could possibly be. Thank you for being patient with my antics throughout my studies and for not giving up on me when I was at my lowest.

Thank you to all the members of the Innovative Manufacturing, Mechatronics and Sports (iMAMS) lab be it members of the past and especially present members for their continuous assistance along the journey of this research. The members have provided much-needed assistance as well as moral support during the journey and I cannot imagine completing this study without their assistance.

Special thanks to Universiti Malaya for awarding the High Impact Research Grant which had provided financial support for this research project.

I would like to extend my heartfelt gratitude to my family; my mother Rosnah binti Mohd Yassin as well as my father Mohd Yaacob Wong Yong Wen for their continuous encouragement and financial support throughout my studies.

My wife, Nur Suhaila for always being the light in my darkness, for being there during all the ups and downs.

## ABSTRAK

Ortosis sendi-buku lali (AFO) yang ideal bagi merawat masalah anggota bawah badan adalah ortosis yang diperbuat mengikut acuan antropometri pemakai. Ortosis yang terdapat dipasaran sedia ada kebanyakannya tidak memenuhi ciri ideal tersebut. Namun begitu tidak dinafikan ortosis dipasaran kini mempunyai kos yang rendah. Penghasilan ortosis yang ideal pula, selain melibatkan kos yang tinggi, turut memerlukan masa pembuatan yang panjang kerana darjah kerumitan yang tinggi. Ia juga turut memerlukan kecekapan, ketelitian dan pengalaman yang tinggi seorang tukang ortosis. Bagi menyelesaikan masalah yang dinyatakan tadi, tesis ini mencadangkan satu metodologi rangkakerja menyeluruh bagi pembangunan suatu ortosis dari peringkat rekabentuk hinggalah peringkat pembuatan. Metodologi rangka kerja ini bertujuan untuk menyelesaikan permasalahan kos dan kerumitan proses pembuatan orthosis dengan mengintegrasikan solusi berkos rendah ke dalam fasa reka bentuk dan pembuatan. Dalam fasa reka bentuk, untuk mendapatkan ukuran antropometri yang jitu pemakai ortosis satu mesin pengimbas 3D berkos rendah telah digunakan. Data antropometri ini seterusnya digunakan untuk merekabentuk satu prototaip didalam perisian reka bentuk bantuan computer (CAD) komersial Autodesk Inventor. Sebelum prototaip ini direalisasikan melalui mesin pembentukan pengendapan terlakur (FDM), sifat mekanik bahan berdasarkan parameter cetakan perlu dikaji untuk memastikan hasil cetakan yang optimum. Hasil cetakan (Zortrax Acrylonitrile Butadiene Styrene (ABS)) menggunakan parameter cetakan yang berbeza seperti orientasi komponen, ketumpatan dan ketebalan lapisan diuji dengan ujian tegangan untuk mengenal pasti integriti struktur yang signifikan bagi pembuatan ortosis. Berdasarkan hasil ujian ini, parameter percetakan yang optimum dilaksanakan ke dalam Model Unsur Terhad (FEM) untuk mengkaji integriti struktur reka bentuk ortosis tersebut. Penilaian integriti struktur ortosis adalah penting untuk mengkaji ketersauran penggunaan mesin pembentukan pengendapan terlakur (FDM) dalam menghasilkan ortosis. Kajian Model Unsur Terhad (FEM) turut menjalankan pengoptimuman topologi bagi mengurangkan berat ortosis serta meminimumkan penggunaan bahan ketika penghasilan ortosis tanpa menjejaskan integriti struktur ortosis tersebut. Hasil daripada pengoptimuman topologi ini, pengurangan kos sebanyak 3% dan peningkatan kekuatan struktur dari faktor keselamatan dari 0.289 ke 4.671 telah dicapai. Berdasarkan keputusan kajian ini, metodologi rangka kerja yang dicadangkan adalah terbukti lebih efisien dalam mengurangkan kos serta meningkatkan kekuatan bagi penghasilan ortosis yang spesifik kepada ukuran antropometri individu.

## ABSTRACT

The ideal type of Ankle Foot Orthosis (AFO) for treating patients with lower limb impairments are those that closely follow the wearer's anthropometry. Most mass-produced AFO that are available in the market does not cater the aforementioned requirements nonetheless it is cost-effective. Conversely, the existing AFO that does conform to individual anthropometry is expensive due to complex geometry, requiring skilled and experienced orthotist. Adding to this cost is the long lead time required to produce a unit of orthosis. In order to mitigate the aforementioned problems of mass produced and individual-specific AFO, this thesis proposes a methodological framework that addresses these issues from the design phase to the fabrication phase. This methodological framework aims to rectify the cost and complexity issue by integrating inexpensive solutions into the design and fabrication stage. In the design phase, a low-cost 3D scanning is adopted to obtain an accurate 3D capture of an individual's anthropometry. An initial AFO prototype is modelled based on this 3D capture data through the use of a commercially available Computer Aided Design (CAD) software package, Autodesk Inventor. Subsequently a tensile test was performed to investigate different mechanical properties arising from varying printing parameters namely; material orientation, build density and print layer thickness of Zortrax Acrylonitrile Butadiene Styrene (ABS) material which is the material used in the fabrication stage employing the use of a low cost Zortrax M200 3D printer. This experimental investigation is not trivial as it provides significant insight on the mechanical characteristics of the varying parameters mentioned above. Based upon the experimental investigation, the best printing parameters were fed into the Finite Element Model to further investigate the structural integrity of the design as well as to carry out the proposed Topology Optimisation method. The evaluation of the structural integrity is important in order to weigh the feasibility of using the Fused Deposition Modelling (FDM) process in the manufacture of tailor made AFO. A structural optimisation is carried out to reduce the weigh and subsequently the cost of production without comprising the structural integrity of the AFO. From the study, by the implementing structural optimisation, specifically the topology method, the end design exhibits a cost reduction 3% and an actual improvement in structural integrity particularly the factor of safety from 0.289 before optimization to 4.671 after optimization suggesting a marked improvement. Therefore, this study has contributed to the body of knowledge by demonstrating that the proposed methodological framework is sound in the manufacture of individually customised AFO.



## TABLE OF CONTENT

<b>DECLARATION</b>	
<b>TITLE PAGE</b>	
<b>ACKNOWLEDGEMENTS</b>	<b>ii</b>
<b>ABSTRAK</b>	<b>iii</b>
<b>ABSTRACT</b>	<b>iv</b>
<b>TABLE OF CONTENT</b>	<b>v</b>
<b>LIST OF TABLES</b>	<b>viii</b>
<b>LIST OF FIGURES</b>	<b>x</b>
<b>LIST OF SYMBOLS</b>	<b>xiv</b>
<b>LIST OF ABBREVIATIONS</b>	<b>xvi</b>
<b>CHAPTER 1 INTRODUCTION</b>	<b>1</b>
1.1 Background of Research	1
1.2 Problem Statement	3
1.3 Objective of Study	4
1.4 Hypothesis of Study	4
1.5 Thesis Outline	5
<b>CHAPTER 2 LITERATURE REVIEW</b>	<b>6</b>
2.1 Introduction	6
2.2 General Characteristics of Ankle Foot Orthosis	7
2.3 Traditional AFO Design and Fabrication Methods	9
2.4 Additive Manufacturing Methods in AFO Fabrication	11

2.4.1	Selective Laser Sintering (SLS)	13
2.4.2	Fused Deposition Modelling (FDM)	16
2.4.3	Stereolithography (SLA)	18
2.4.4	Comparison of SLS, FDM and SLA Processes in Efficacy of AFO Fabrication	21
2.5	Structural Optimization	22
2.5.1	Types of Structural Optimization	24
2.5.2	Application of Structural Optimisation in AFO Design	25
2.5.3	Considerations for Implementation of Structural Optimisation for Parts Fabricated using Fused Deposition Modelling	27
<b>CHAPTER 3 METHODOLOGY</b>		<b>30</b>
3.1	Introduction	30
3.2	Ankle-Foot Region Scanning	31
3.3	FDM Material Characterization	34
3.3.1	Fabrication and Preparation of Specimens	34
3.3.2	Tensile Test Procedures	38
3.4	Modelling of the AFO	40
3.4.1	Geometrical Model	40
3.4.2	Material Properties	44
3.4.3	Boundary Conditions – Loads and Constraints	45
3.5	Topology Optimisation	54
3.6	Cost Model for Fabrication of AFO using the FDM Process	55
<b>CHAPTER 4 RESULTS AND DISCUSSION</b>		<b>60</b>
4.1	Scanned Limb 3D Geometry and Initial AFO Design	60

4.2	Tensile Test Results of FDM Printed Specimens for Different Printing Parameters	63
4.2.1	Tensile Test Results for Specimens of Different Layer Thickness	63
4.2.2	Tensile Test Results for Specimens of Different Infill Densities	73
4.2.3	Summary of Tensile Test Findings and Selection of Process Parameters for Fabrication of AFO	79
4.3	AFO Finite Element Analysis	84
4.3.1	Heel Strike Gait Phase AFO FEA Results	84
4.3.2	Midstance Gait Phase AFO FEA Results	86
4.3.3	Push Off Gait Phase AFO FEA Results	89
4.4	AFO Topology Optimization Results	91
4.5	AFO Cost Estimation	94
	<b>CHAPTER 5 CONCLUSION</b>	<b>96</b>
5.1	Conclusion	96
5.2	Limitation of Research Work	97
5.3	Recommendations for Future Works	97
	<b>REFERENCES</b>	<b>99</b>
	<b>APPENDIX A BLACK TO WHITE RATIO MATLAB CODE</b>	<b>105</b>
	<b>APPENDIX B ANKLE FOOT ORTHOSIS PROTOTYPE DIMENSIONS</b>	<b>106</b>
	<b>APPENDIX C MODULUS OF ELASTICITY – FILAMENT THICKNESS A</b>	<b>107</b>
	<b>APPENDIX C MODULUS OF ELASTICITY – FILAMENT THICKNESS B</b>	<b>109</b>
	<b>APPENDIX D MODULUS OF ELASTICITY – FILAMENT THICKNESS C</b>	<b>111</b>

## LIST OF TABLES

Table 2.1	Summary of Research on the Application of SLS in AFO Fabrication	14
Table 2.2	Summary of Research on the Application of the FDM Process in AFO Fabrication	17
Table 2.3	Summary of Research on the Application of the SLA Process in AFO Fabrication	20
Table 2.4	Comparison of Process Characteristics between SLS, FDM and SLA. Green table shading denotes desirable properties.	21
Table 2.5	Summary of Research Works Applying Structural Optimisation	26
Table 2.6	Summary on Research Investigating Mechanical Properties of Fused Deposition Modelling Components	28
Table 3.1	Microsoft Kinect 360 Technical Specifications	31
Table 3.2	Build Settings Density Calculation Using Black and White Image Mapping Method	37
Table 3.3	Specimen Build Parameters and Specimen Numbers	38
Table 3.4	INSTRON UTS Machine Testing Parameters	39
Table 3.5	Convergence Analysis Settings	41
Table 3.6	AFO Mesh Parameters	43
Table 3.7	Body Mean Segment Weight (Based on Percentage Value, Adapted from (Plagenhoef et al., 1983) for Lower Limb Segments)	46
Table 3.8	Foot Pressure Profile Adapted from. Park et al.'s (2009)	49
Table 3.9	Force Boundary Condition for Mid-stance Phase	52
Table 3.10	Force Boundary Condition for Mid-stance Phase	53
Table 3.11	Topology Optimization Configuration	54
Table 3.12	Mesh Configuration for Topology Optimisation Process	54
Table 4.1	Comparison of Measurements Between Scanned and Actual Limb	60
Table 4.2	Dimensions for Trimline	61
Table 4.3	A-Build Orientation, Low Density Z-ABS Material Properties for Different Layer Thickness (N = 5 Samples for Each Layer Thickness). Values of Properties are of Average Value for 5 Samples.	64
Table 4.4	B-Build Orientation, Low Density Z-ABS Material Properties for Different Layer Thickness (N = 5 Samples for Each Layer Thickness). Values of Properties are of Average Value for 5 Samples.	68

Table 4.5	C-Build Orientation, Low Density Z-ABS Material Properties for Different Layer Thickness (5 Samples for Each Layer Thickness). Values of Properties are of Average Value for 5 Samples.	71
Table 4.6	A-Build Orientation, Constant Layer Thickness of 0.29 mm Material Properties for Different Infill Densities (5 Samples for Each Infill Density Setting).	74
Table 4.7	B-Build Orientation, Constant Layer Thickness of 0.29 mm Material Properties for Different Infill densities (5 Samples for Each Infill Density Setting).	76
Table 4.8	C-Build Orientation, Constant Layer Thickness of 0.29 mm Material Properties for Different Infill Densities. (5 Samples for Each Layer Thickness). Values are average for 5 Samples.	78
Table 4.9	Mass of Fabricated AFO (Inclusive of Support Material) Calculated by Z-Suite Software for Different Process Parameters	83
Table 4.10	Selected Process Parameter (B-build Orientation, Filament Thickness = 0.14 mm, Medium Infill Density) and Material Properties.	83
Table 4.11	Minimum and Peak Principal Stress Values for Heel Strike Phase	84
Table 4.12	Peak Displacement for AFO FEA of Heel Strike Gait Phase	85
Table 4.13	Minimum and Peak Principal Stress Values for Midstance Phase	87
Table 4.14	Peak Displacement for AFO FEA of Midstance Gait Phase	87
Table 4.15	Peak Displacement for AFO FEA of Midstance Gait Phase	89
Table 4.16	Parameter Values for AFO Prototype Cost Calculation	95



## LIST OF FIGURES

Figure 1.1	Number of 3D Printers (Priced under \$5,000) Sold Worldwide From The Year 2007 to 2015. Source: (Wohlers, 2015)	2
Figure 2.1	Flexible AFO (Left) and Limb Movement that FAFO Assists Upon (Right)	7
Figure 2.2	Rigid Ankle Foot Orthosis	8
Figure 2.3	Fabrication Stages for Customised Foot Orthosis	9
Figure 2.4	Measurement Stage in the Fabrication of AFOs from Negative Cast (A) till Positive Cast (F). Source: Becker Orthopedic Appliance (2003)	10
Figure 2.5	Standard Trim Line Dimension for Rigid AFO Source: ICRC (2010)	11
Figure 2.6	Summary of General Additive Manufacturing Steps Source: European Powder Metallurgy Association (2015)	12
Figure 2.7	Selective Laser Sintering Process Schematics Source: Kalyani & Bansal (2016)	13
Figure 2.8	Rigid AFO with Single Strut Designed using Topology Optimisation (Faustini et al., 2008)	15
Figure 2.9	Fused Deposition Modelling (FDM) Process Schematics	16
Figure 2.10	Stereolithography (SLA) Process Schematics	18
Figure 2.11	Fitting of the AFO Fabricated via the Stereolithography Process Source: Mavroidis et al. (2011).	19
Figure 2.12	Sizing Optimization on a Truss Structure Source: Olason & Tidman (2010)	24
Figure 2.13	Shape Optimization on a Structure with Circular Holes Source: Olason & Tidman (2010)	24
Figure 2.14	Topology Optimization Performed on a Structure with only Boundary Parameters Source: Olason & Tidman (2010)	25
Figure 2.15	Mechanical Properties - Tensile Strength [MPa] caused by (a) building direction, (b) infill percentage, (c) printing speed, (d) infill patterns, (e) extrusion temperature and (f) layer height, where E is young's modulus, $S_y$ is the yield strength and $T_s$ is the tensile strength Source: Ahn et al. ( 2002).	27
Figure 2.16	Standardised Axes Used to Describe Build Orientation Across Literature	29
Figure 3.1	Research Flow Chart	30
Figure 3.2	Major Components of a Microsoft 360 Kinect Device	32
Figure 3.3	Kinect 3D Scanning Setup	32
Figure 3.4	Post-Processed 3D Geometry of Scanned Limb	33

Figure 3.5	Foot Anthropometry Measurements	34
Figure 3.6	Zortrax M200 3D Printer	35
Figure 3.7	Tensile Test Specimen Dimensions for Z-ABS Material	35
Figure 3.8	Build Orientations with Respect to AFO and Coordinate System	36
Figure 3.9	Printing Location of Z-ABS Test Specimens	36
Figure 3.10	Infill Density Settings (From Left; Low, Medium and High Settings Respectively)	37
Figure 3.11	Test Specimens Conditioned in a Dry Cabinet with Temperature Control	38
Figure 3.12	INSTRON 3300 UTS Machine and Test Setup	39
Figure 3.13	Parabolic-Tetrahedron Element Nodes (10 Nodes Total)	40
Figure 3.14	Parabolic-Tetrahedron (CTETRA) Element Coordinate System	41
Figure 3.15	Convergence Plot for different Mesh Iterations (Top – Von Mises Stress, Bottom – Displacement)	42
Figure 3.16	Meshed AFO Geometry (From Left; Isometric, Side, Front and Back View Respectively).	44
Figure 3.17:	Free-Body Diagram for The Heel Strike Gait Phase	46
Figure 3.18	Free-Body Diagram for the Mid Stance Gait Phase	47
Figure 3.19	Free-Body Diagram for the Push Off Gait Phase	48
Figure 3.20	Obtaining Foot Feature Coordinates from 3D Foot Scan	48
Figure 3.21	Traced Geometry of Scanned Foot. The Yellow Dot Represents the Origin of the Coordinates.	49
Figure 3.22	Foot Pressure Boundary Condition Applied on Midstance Gait Phase FE Model (Left – Top View, Right- Isometric View)	50
Figure 3.23	Location of Fixed Constraint in the AFO Model for the Midstance Gait Phase.	50
Figure 3.24	Obtained Shank Profile (Left-Feature Tracing, Right-Resultant Geometry)	51
Figure 3.25	Location of Force FE Model Definition during Heel Strike Gait Phase	51
Figure 3.26	Loadings and Constraints Applied to Heel Strike Phase AFO FE Model (Left - Fixed Constraint , Right – Loads).	52
Figure 3.27	Location of Force FE Model Definition during Push Off Gait Phase	53
Figure 3.28	Push off Gait Phase FE Model Boundary Conditions	53
Figure 3.29	Boundary Condition for AFO Topology Optimisation	55
Figure 4.1	Dimensions for Construction of Trim line (M. A Arnold, 1999)	61
Figure 4.2	AFO Design Process - Splitting of the Geometries	62

Figure 4.3	Initial Prototype of Ankle Foot Orthosis Designed Based on Scanned Geometry.	62
Figure 4.4	A Build Orientation Specimen Stress-Strain Curves for Layer Thickness of 0.09mm, 0.14mm, 0.19mm and 0.29mm (From top to bottom respectively)	63
Figure 4.5	Direction of Forces, $N$ to A-Build Orientation Filament Arrangement	65
Figure 4.6	Failure Mode of A-Build Orientation for Each Layer Thickness	66
Figure 4.7	B Build Orientation Specimen Stress-Strain Curves for Layer Thickness of 0.09mm, 0.14mm, 0.19mm and 0.29mm (From top to bottom respectively)	67
Figure 4.8	Direction of Forces, $N$ to B-Build Orientation Filament Arrangement	69
Figure 4.9	Failure Mode of B-Build Orientation for Each Layer Thickness	69
Figure 4.10	C Build Orientation Specimen Stress-Strain Curves for Layer Thickness of 0.09mm, 0.14mm, 0.19mm and 0.29mm (From top to bottom respectively)	70
Figure 4.11	Direction of Forces, $N$ to C-Build Orientation Filament Arrangement	71
Figure 4.12	Failure Mode of C-Build Orientation for Each Layer Thickness	72
Figure 4.13	A Orientation Specimen Stress Strain Curves for Low, Medium and High Infill Densities (From top to bottom respectively.)	73
Figure 4.14	B Orientation Specimen Stress Strain Curves for Low, Medium and High Infill Densities (From top to bottom respectively.)	75
Figure 4.15	C-Orientation Specimen Stress Strain Curves for Low, Medium and High Densities (From top to bottom respectively.)	77
Figure 4.16	Average Maximum Stress (MPa) Across Varying Layer Thickness (mm)	79
Figure 4.17	Average Elastic Modulus (MPa) Across Varying Layer Thickness Size (mm)	79
Figure 4.18	Tensile Stress Standard Deviation (MPa) Across Varying Filament Thickness (mm)	80
Figure 4.19	Average Maximum Stress (MPa) Across Varying Infill Density Settings ( $\text{kg/m}^3$ )	80
Figure 4.20	Average Elastic Modulus (MPa) Across Varying Infill density Settings ( $\text{kg/m}^3$ )	81



Figure 4.21	Tensile Stress Standard Deviation (MPa) Across Varying Infill density Settings ( $\text{kg/m}^3$ )	81
Figure 4.22	Final Printing Geometry with Support Structure Generated by 3D Printer Software (A, B and C Build Orientation Respectively.)	82
Figure 4.23	Von Misses Stress of AFO During Heel Strike Gait Phase	84
Figure 4.24	Displacement of AFO During Heel Strike Gait Phase	85
Figure 4.25	Factor of Safety Plot of AFO During Heel Strike Gait Phase	86
Figure 4.26	Von Misses Stress of AFO During Midstance Gait Phase	87
Figure 4.27	Displacement of AFO During Midstance Gait Phase	88
Figure 4.28	Factor of Safety Plot of AFO During Midstance Gait Phase	88
Figure 4.29	Von Misses Stress of AFO During Push Off Gait Phase	89
Figure 4.30	Displacement of AFO During Push Off Gait Phase	90
Figure 4.31	Factor of Safety Plot of AFO During Heel Strike Gait Phase	90
Figure 4.32	Front View Element Removal Process of the AFO Geometry Across Simulation Time (From Left) till Convergence (Right)	91
Figure 4.33	Side View Element Removal Process of the AFO Geometry Across Simulation Time (From Left) till Convergence (Right)	91
Figure 4.34	Original AFO Geometry (Left) and Optimised Geometry (Right).	92
Figure 4.35	Support Material for Original Geometry (Left) and Optimised Geometry (Right)	92
Figure 4.36	Optimised AFO Von Misses Stress	93
Figure 4.37	Optimised AFO Displacement (Left) and FOS (Right) Plot	94

UMP

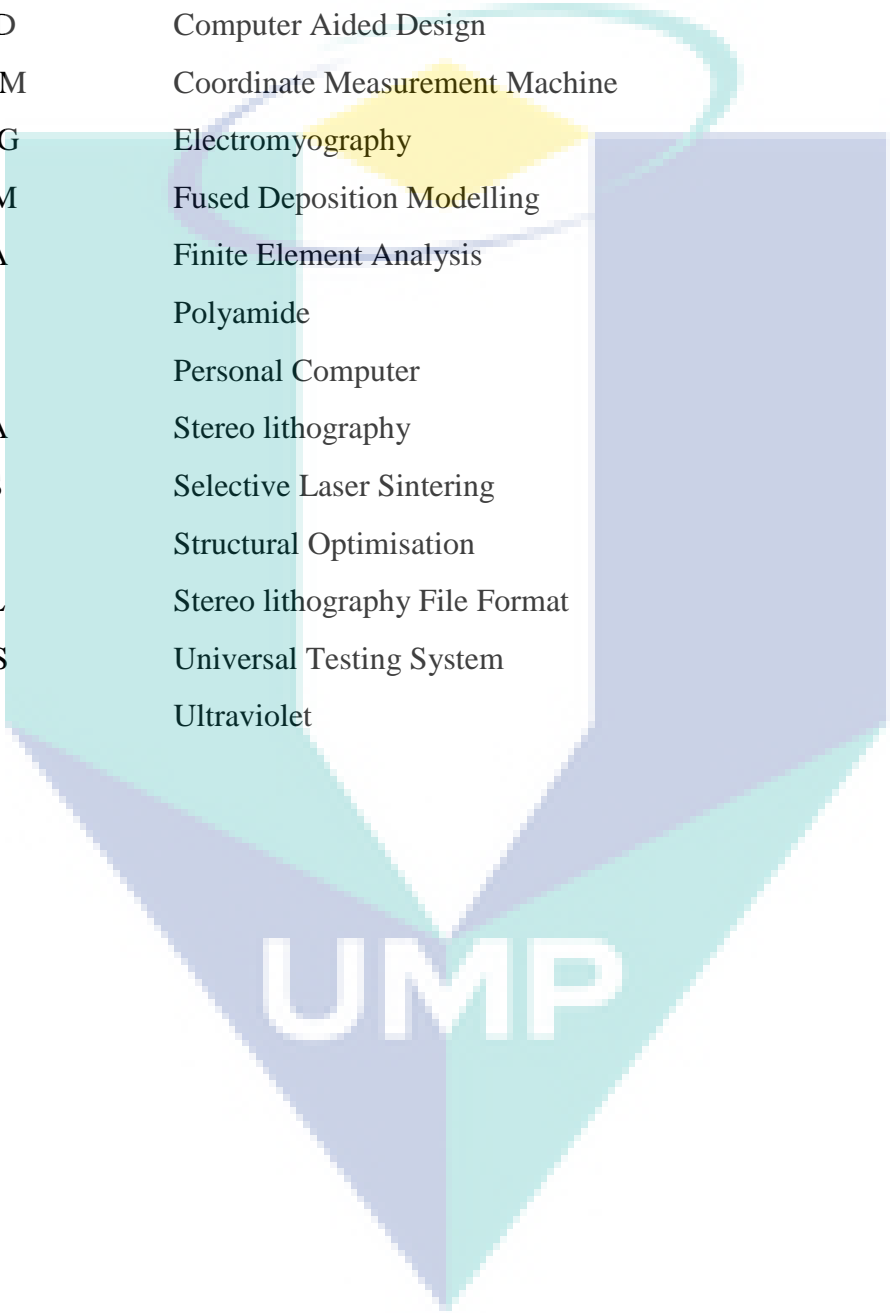
## LIST OF SYMBOLS

$C_e$	Execution Cost
$C_{fp}$	Prototype Cost
$C_m$	Material Cost
$C_p$	Processing Cost
$C_{pc}$	Personal Computer
$C_{pp}$	Post-Processing Cost
$C_{sl}$	Software License Cost
$F_{BW}$	Body Weight Force
$F_{CTC}$	Leg to Shank Contact Force
$F_R$	Ground Reaction Force
$F_a$	Ankle Stabilising Force
$L_{hind}$	End of Heel Moment Length
$M_a$	Ankle Stabilising Moment
$M_b$	Push Off Moment
$M_m$	Maintenance Cost Per Month
$PC_e$	PC Energy Consumption Hour Rate
$P_{bp}$	Bowl Price
$P_e$	Machine Energy Consumption Rate Per Hour
$P_{kh}$	Local Average Energy Specific Cost
$P_{kh}$	Local Average Energy Specific Cost
$P_m$	Specific Cost Per Model Material Volume
$P_{mat}$	Specific Material Cost Per Spool
$P_{mp}$	Machine Price
$P_s$	Specific Cost Per Support Material Volume
$P_{ub}$	Energy Consumption Rate Per Hour for the Ultrasonic Bowl
$R_x$	Rotation in X-Axis
$R_y$	Rotation in Y-Axis
$R_z$	Rotation in Z-Axis
$S_c$	Soap Cost Per Washing Time at Post-Processing
$S_r$	Soap Rate Per Package

$T_p$	Designer Processing Time
$T_{pm}$	Model Permanence Time Inside the Ultrasonic Bowl
$T_x$	Translation in X-Axis
$T_y$	Translation in Y-Axis
$T_z$	Translation in Z-Axis
$V_c$	Model/Support Material Volume Per Cartridge
$V_m$	Model Volume Utilised
$V_s$	Support Volume Utilised
$V_{total}$	Total Weight Per Spool
$V_{util}$	Total Material Utilised
$W_{at}$	Bowl Availability Time Per Year
$W_{at}$	Machine Availability Time Per Year
$W_{at}$	PC Availability
$m_{leg}$	Leg Shank Mass
$r'_f$	Machine Running Cost Per Hour
$\theta_1$	Shank Contact Angel
$\theta_2$	Dorsiflexion Angle
$\sigma_{MAX}$	Maximum Stress
$\sigma_{YIELD}$	Yield Stress
$\omega_0$	Operator Cost Per Hour
$\omega_d$	Designer Cost Per Hour
$L$	Moment Arm Length

UMP

## LIST OF ABBREVIATIONS



ABS	Acrylonitrile Butadiene Styrene
AFO	Ankle Foot Orthosis
AM	Additive Manufacturing
CAD	Computer Aided Design
CMM	Coordinate Measurement Machine
EMG	Electromyography
FDM	Fused Deposition Modelling
FEA	Finite Element Analysis
PA	Polyamide
PC	Personal Computer
SLA	Stereo lithography
SLS	Selective Laser Sintering
SO	Structural Optimisation
STL	Stereo lithography File Format
UTS	Universal Testing System
UV	Ultraviolet

## CHAPTER 1

### INTRODUCTION

#### 1.1 Background of Research

Additive Manufacturing (AM) is a manufacturing process where material is added during the fabrication of a component. This process contrasts that of traditional manufacturing processes which employs cutting tools to remove materials from a given stock material to obtain a desired end shape and is often limited by the geometry of the said tools. This limitation substantially restricts the capability of traditional manufacturing processes to produce complex and intricate parts due to the limitation of tool reach and obstruction between tool holder and work piece. This limitation however, is not apparent in additive manufacturing process where part design complexity does not result in any significant trade-offs whether it is in terms of cost or process time (Wong & Hernandez, 2012).

Charles Hull patented the first AM machine in 1986 in his patent entitled “Apparatus for Production of Three-Dimensional Objects by Stereolithography”. The aforementioned AM machine employed the stereolithography method where components were shaped through adding of layers by layers of thin consecutive layers of liquid photopolymer resin through Ultraviolet (UV) curing (Hull, 1986). The primary objective of Hull’s machine during that time was to produce mock up models and prototypes before actual fabrication of the said component. Though the basis for the technology still remains similar, the technology had seen a surge in adoption popularity (as shown in Figure 1.1) due to exponentially machine lower costs and relative ease of use compared to a few decades before. The AM process had also transitioned in its function from prototype fabrication to fabrication of actual functional products. With the advent of accessible AM processes, many field that requires the fabrication of complex and

sophisticated parts had started adopting AM methods due to its inherent process capabilities as well as cost-saving nature due to the lack of manufacturing waste.

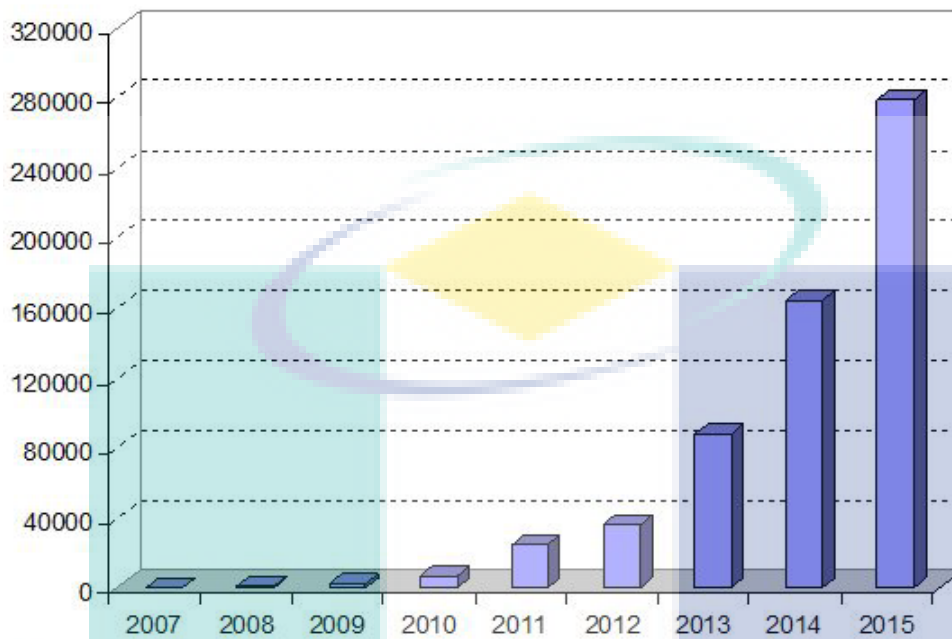


Figure 1.1 Number of 3D Printers (Priced under \$5,000) Sold Worldwide From The Year 2007 to 2015.  
Source: (Wohlers, 2015)

Orthosis are externally applied devices designed to give support, re-align or to remove weight bearing for specific responses as well as to redistribute forces across part of an individual's musculoskeletal system (Organisation Internationale de Normalisation (ISO), 1989). These devices function primarily to either control an individual's biomechanical alignment, correct or accommodate deformity, assist in rehabilitation, reduce pain or increase mobility and independence. There are various types of orthosis and they vary according to their functions but generally, they are divided into two; prefabricated and customised orthosis respectively. Prefabricated orthosis is a pre-made orthosis and is usually prescribed for short term use or non-complex clinical ailments whereas custom-made orthosis is a highly-specialised device that is manufactured from the cast of an individual designed to fit only that individual specifically.

As stated by (Hawke et al., 2008) and (Trotter & Pierrynowski, 2008), custom-made, individual specific orthosis has been found to be the most effective for the treatment of many conditions as the device takes into consideration the individual patient's anatomy and functional requirements during the design process. The main problem of this approach is that the traditional method of producing customised orthosis

takes up time and requires skilled and experienced orthotist. Due to these requirements, the base cost for a customized ankle foot orthosis averages around £700 per unit (Center for Economics and Business Research Ltd, 2011) for the year 2010 which had made these devices highly inaccessible by a majority group of people with lower income levels.

To tackle this problem of high cost, several researches have focused on streamlining the overall process of producing customised orthosis in order to reduce time and cost needed to manufacture orthosis devices. For the design process of the ankle foot orthosis, researchers had looked into implementing automated measurement systems such laser 3D Scanning systems (Telfer & Woodburn, 2010) as well as surface digitisation methods using contact scanners (Saleh, 2013). These automated systems are rapid in their measurement speed and have an acceptable rate of consistency, accuracy, and repeatability. Apart from optimising the design procedures, researchers had also adapted various AM processes such as Selective Laser Sintering (SLS), Stereolithography (SLA) and Fused Deposition Modelling (FDM) which had resulted in large time savings and cost reduction. This contributed to AM's continuing popularity in the fabrication of complex orthosis (Jin et al., 2015). These approaches, however still have a lot of headroom for improvement. In this research, our aim is to further reduce the cost in manufacturing the said orthosis devices by designing a methodological framework that integrates low cost solutions right from the design phase until the fabrication phase.

## **1.2 Problem Statement**

Current fabrication methods of customised orthoses are complex, costly and time-consuming. Traditional methods require experienced orthotist whose design's decisions are often based on experience or trial and error instead of a standardised design procedure that accounts for different anthropometry. In addition to that, the individual's anthropometry is captured via means of setting a cast on top of the individual's limb. This cast is later used to create a positive model which in the end will act as a mould for plastic thermoforming. This thermoformed plastic will become the final AFO after processing. This separate measurement and fabrication stages of the AFO involving multiple model and impressions further lengthens the AFO fabrication process and add up to the final costs. To tackle this problem, several types of research had started adopting AM methods

to overcome process limitations and streamline the manufacturing process of AFOs by replacing certain steps in traditional fabrication with digital prototyping using Computer Aided Design (CAD) software. Although several studies had focused on this topic, none had investigated solutions to the underlying problem of using AM technology for fabrication of functional products which is structural integrity. Structural integrity in this sense, is the ability of the said products to withstand functional loads and forces of the wearer without undergoing permanent deformation or failure.

### **1.3 Objective of Study**

The aim of the research is to develop a low-cost, functional, design optimised, customised to individual Rigid Ankle Foot Orthosis (AFO) fabricated through the Fused Deposition Modelling (FDM) process. To achieve this aim, the research objectives are set as follows:

1. To perform material characterisation on FDM material and analyse the effect of FDM process parameters on the material properties of the produced parts.
2. To apply structural optimisation specifically topology optimisation on the AFO produced by the FDM Process.
3. To analyse the structural integrity and shape of the optimised AFO geometry and compare it with un-optimised design.

### **1.4 Hypothesis of Study**

An orthosis design optimised via the Topology Optimisation (TO) method and cost savings via the implementation of inexpensive measurement device like the one used in this study (Kinect) will reduce the cost required to produce a functional and structurally sound customised rigid AFO.



## 1.5 Thesis Outline

This thesis is divided into 5 chapters, as the following:

Chapter 1 presents the background of research, the problem statement as well as the main objectives of the study.

Chapter 2 presents specific details on ankle foot orthosis as well as current findings on FDM processes and design optimisation.

Chapter 3 describes the methodology employed to achieve the aforementioned objectives. The methodology covers the 3D foot scanning methods, FDM material fabrication and testing standards, Finite Element Analysis (FEA) setup as well as the design optimisation flow.

Chapter 4 demonstrates the components of the methodological framework which encompasses the experimental results of the 3d scanning process as well as its accuracy, material testing, finite element analysis results for before and after design optimisation as well as the functional evaluation results of the optimised AFO. Detailed cost evaluation of said orthosis is also presented in this chapter.

Chapter 5 presents the summary of all the findings that are discussed in Chapter 4 as well as future recommendations for the continuation of this work.



UMP

## CHAPTER 2

### LITERATURE REVIEW

#### 2.1 Introduction

The key objective of this research is to produce a rigid AFO that is low cost, functional, design optimised and customised to an individual. This is mainly attained by streamlining and replacing certain stages in the fabrication process of AFOs with tools and methods that cut development time and cost. To achieve this, an understanding of the functional and structural requirements of AFO devices as well as the whole of AFO fabrication process is necessary to evaluate in which area improvement can be done. As previously mentioned in the introduction chapter, shape optimisation is proposed as a method to fulfil the aforementioned objectives. An understanding of the proposed tool is also necessary to investigate whether it is feasible to implement to the current processes.

In this chapter, a review of the state of the art, as well as background knowledge of the AFO fabrication process are presented. The review starts with the common characteristics and functional requirements of AFOs to the current widely used traditional AFO manufacturing methods. Advancements in the process, mainly the recent adoption of Additive Manufacturing (AM) methods and the efficacy of the said approach are also reviewed and discussed. In the last section of this chapter, a review on shape optimisation, the proposed tool for the improvement in AFO design in this study is performed. This review covers the shape optimisation types, current application and also the efficacy of shape optimisation in reducing cost and improving overall product design.

## 2.2 General Characteristics of Ankle Foot Orthosis

By definition, orthosis is “an externally applied device used to modify the structural or functional characteristics of the neuromuscular system” (Organisation Internationale de Normalisation (ISO), 1989). There are many types of orthosis, each usually named accordingly to their specific region of function in the human body and is commonly classified according to their physical rigidity. The Ankle Foot Orthosis (AFO) is an orthosis that encompasses the region of the ankle and the foot. There are generally three types of AFOs namely the flexible AFO and rigid AFO in which the differentiation of these types depends on the aimed function as well as the physical properties of the AFO.

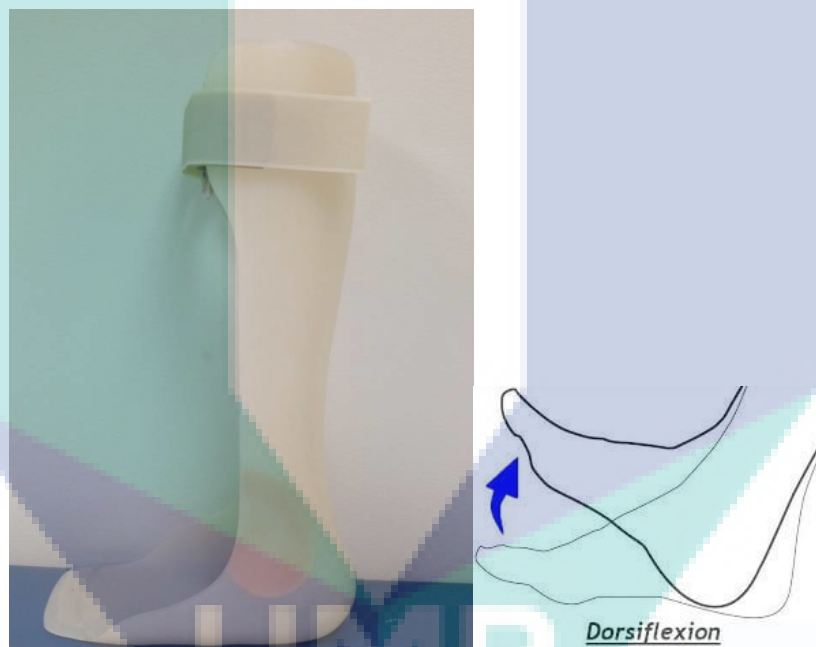


Figure 2.1 Flexible AFO (Left) and Limb Movement that FAFO Assists Upon (Right)

As shown in Figure 2.1, Flexible Ankle Foot Orthosis (FAFO) is an orthosis that is made out of elastic and conforming materials such as polypropylene, ethylene vinyl acetate (EVA) as well as foam. The purpose of FAFOs is to provide propulsion assist for isolated dorsiflexion weakness such as simple swing phase problems (drop foot). The elastic material used in FAFOs help store energy during mid stance and release stored elastic energy during the Heel-Off phase. This energy storage and release mechanism of flexible AFO helps in increasing gait velocity, cadence and stride length of patients when worn (Rao et al., 2014). Due to the nature of the FAFO, this type of orthosis is usually

prescribed for patients with a weakness or semi spasticity as the patient must possess the ability to move their limbs in order for the energy storage and release mechanism to work.

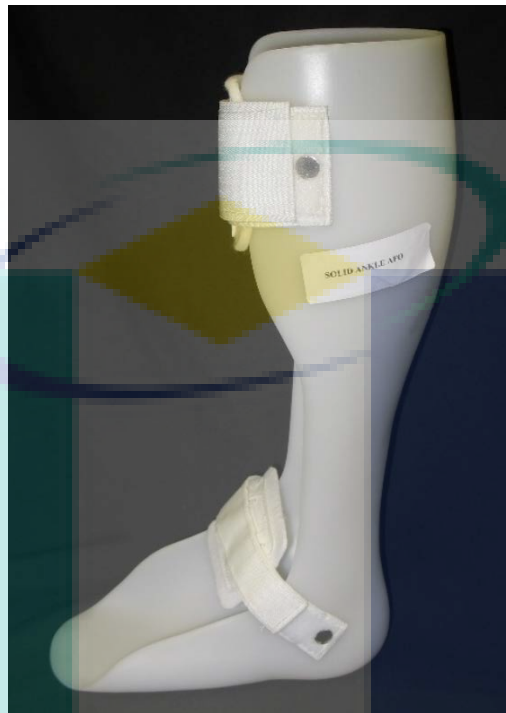


Figure 2.2 Rigid Ankle Foot Orthosis

In contrast with Flexible AFOs, Rigid Ankle Foot Orthosis (RAFO) as shown in Figure 2.2 is mainly made of rigid materials such as reinforced polypropylene, acrylonitrile butadiene styrene (ABS) or carbon fibre. RAFOs function fully as a supportive brace that removes weight bearing from the limb that it is worn upon. RAFOs are usually prescribed to patients with lower limb ailments such as low motion ability of the knee, stiff gastrocnemius (shank) muscle, instabilities of the ankle joint as well as patients with joint control requirements at the hip and knee (M. Wong et al., 2010). Placing joint control requirements in these cases are useful in conditions where certain joint movements will cause injury or lengthen the duration of healing of the lower limb muscle or joint. Due to the rigid and support-bearing nature of the RAFO, fitting is a main priority in its design and fabrication.

## 2.3 Traditional AFO Design and Fabrication Methods

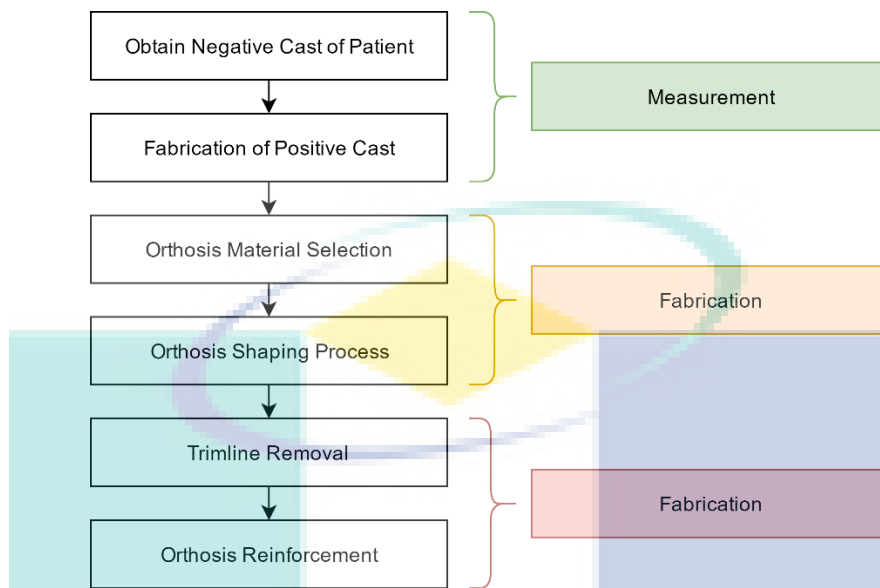


Figure 2.3 Fabrication Stages for Customised Foot Orthosis

There are two types of methods in fabricating AFO. One of it is the prefabricated method where instead of making a custom cast based on the individual's limb, a pre-made positive cast is used. These pre-made positive casts each is designed to cater for a range of anthropometry and manufacturers of AFO commonly resort to this approach as means of cost-cutting. The other type of AFO fabrication method is customised orthosis.

This section focuses specifically on the traditional fabrication methods as it is generally the de facto method used in producing customised Ankle Foot Orthoses. The traditional AFO fabrication method for customised orthosis is mainly divided into three main stages as shown in Figure 2.3; the first stage being the measurement stage where the individual's anthropometry is captured, followed by the fabrication stage where the AFO will be fabricated based on the captured anthropometry and finally the post-processing stage where the final rectification process is performed on the AFO.

In the first stage, the anthropometry features of the individual's lower limb are obtained by creating a replicate model usually made of plaster. This model replicate is made by first wrapping the individual's leg with a plaster bandage cast. Once this cast is hardened, it is removed from the individual's leg forming the negative cast of the patient's leg as shown in Figure 2.4 - A. This negative cast is then filled with liquid plaster (C) and once the filled plaster hardens, the outer shell is removed leaving a rough positive cast. This positive cast is rough (D) due to the bandage seams and will undergo smoothing and

rectifying process (E) to remove creases and to smooth out uneven surfaces. The final form of the positive cast is shown in Figure 2.4 - F.



Figure 2.4 Measurement Stage in the Fabrication of AFOs from Negative Cast (A) till Positive Cast (F).

Source: Becker Orthopedic Appliance (2003)

The plastic selection depends on the specialised purpose of the AFO. There are three common consideration variables for plastic selection; the type, thickness and quality of the plastic (Becker Orthopedic Appliance, 2003). The types of plastic selected for Rigid AFOs as mentioned previously are usually PP, ABS and CF and these plastics used are in the form of plastic sheets (with a thickness of 5 mm to 6 mm in the case of Rigid AFOs).

Before shaping these plastic sheets, the trim line is marked on the positive cast. Trim line is the marking used to determine the portion of the plastic sheet that will be removed which provides a functional shape to the orthosis in the thermoforming mold. There are many types of trim lines each with varying dimensions depending on the type of ailment and how the orthosis is expected to function to cater structurally to these functions. The varying dimensions of AFOs usually only affect the top, ankle and forefoot part marked as A, B and C respectively, as shown in Figure 2.5. In the case of a standard rigid AFO, the A trim line must be 2 cm below the fibula head, B trim line must pass the

ankle 1 cm anterior to the tip of the malleoli and C trim line must leave the sides of the toes and the head of the metatarsus completely clear at the forefoot (ICRC, 2010).



Figure 2.5 Standard Trim Line Dimension for Rigid AFO  
Source: ICRC (2010)

These plastic sheets are subsequently heated and placed on the positive cast. A second layer of plastic is then vacuum-moulded immediately on top of the previously placed plastic as a reinforcement. The thermoforming process melts the plastic sheet and subsequently, the vacuum forming process uses vacuum pressure to press the hot sheet of plastic to take on the shape of the positive cast. Once the plastic sheet cools and cures, the final product is formed which is the orthosis.

#### 2.4 Additive Manufacturing Methods in AFO Fabrication

In this section, the AM methods discussed is only limited to those used in the fabrication of AFOs. The major AM methods that will be discussed and evaluated are Selective Laser Sintering (SLS), Stereolithography (SLA) and Fused Deposition Modelling (FDM). These fabrication methods are used widely in the fabrication of customised orthosis due to their high accuracy, being able to produce sub-millimetre resolution with ease as well as their capability to produce highly complex geometries without substantially increasing cost or fabrication time. This section is performed to evaluate some of the alternatives AM types available in market and evaluate their advantages and disadvantages with one another.

Additive Manufacturing (AM) is a type of manufacturing process that utilises a computer-controlled machine to add layer by layer of material in order to manufacture a desired part or component. It is coined to be “additive” since material is added instead of removed such as in the case traditional manufacturing process such as milling or drilling. As exhibited in Figure 2.6, the AM process generally involves similar steps with differences only on how the layers are added and what type of materials that are used in the fabrication process. At first, a component designed in CAD software is exported into the Stereolithography file format (STL), the most commonly used file for transferring geometry data in AM process. This file is then loaded into a 3D slicer software in which the 3D model is sliced into multiple 2D layers. An NC code for the AM’s machine tool path is then generated based on the topology of the 2D sliced layers and is uploaded to the machine for fabrication.

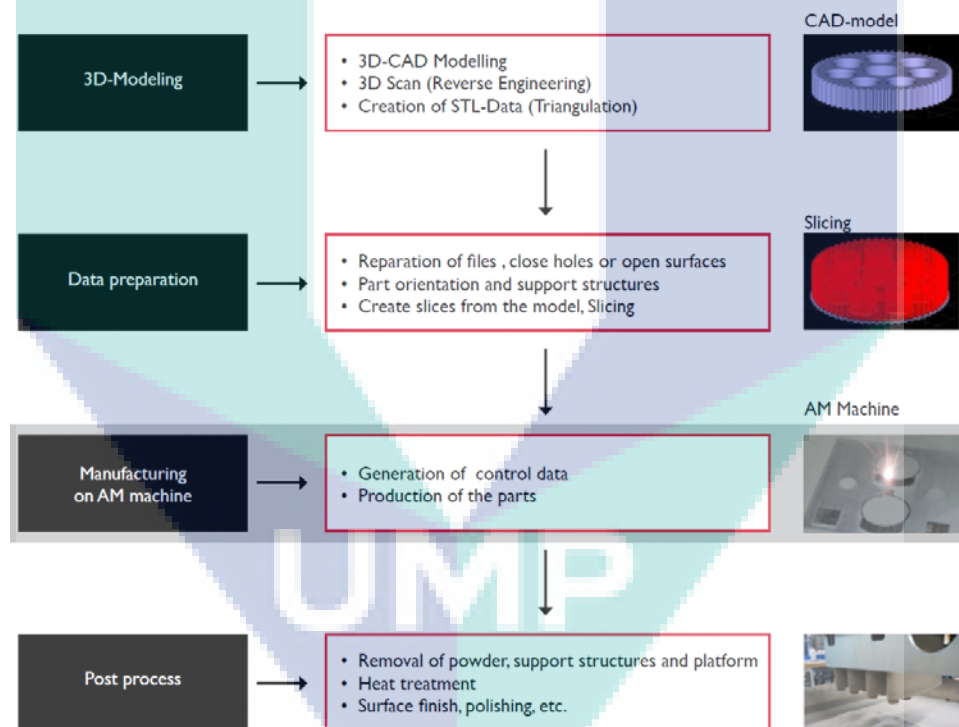


Figure 2.6 Summary of General Additive Manufacturing Steps  
Source: European Powder Metallurgy Association (2015)

AM technology had been continuously developed since its introduction two decades ago. The problem during its initial introduction is that the acquisition of AM machines and ancillary equipment had steep costs and the application of the AM processes are generally limited to a small amount of available material with properties that restrict its application (Telfer et al., 2012). Recently, technological advancements



have been made where AM technologies have taken mass customisation business model, reducing the cost and technical skills required to handle the said technology. The availability of these AM machines especially for the Fused Deposition Modelling (FDM) process has brought AM process to the mainstream, consumer markets. Consumer 3D printers such as Alunar, Makerbot, Kloner3D are now available for a relatively low upfront cost bundled with a simple software that ease fabrication. Even though most of the aforementioned FDM machines are suitable for low volume manufacturing or only producing non-functional prototypes, certain consumer 3D printer is now able to produce parts high in strength and durability using plastics such as polypropylene and acrylonitrile butadiene styrene (ABS) with some being able to print even metal parts.

#### 2.4.1 Selective Laser Sintering (SLS)

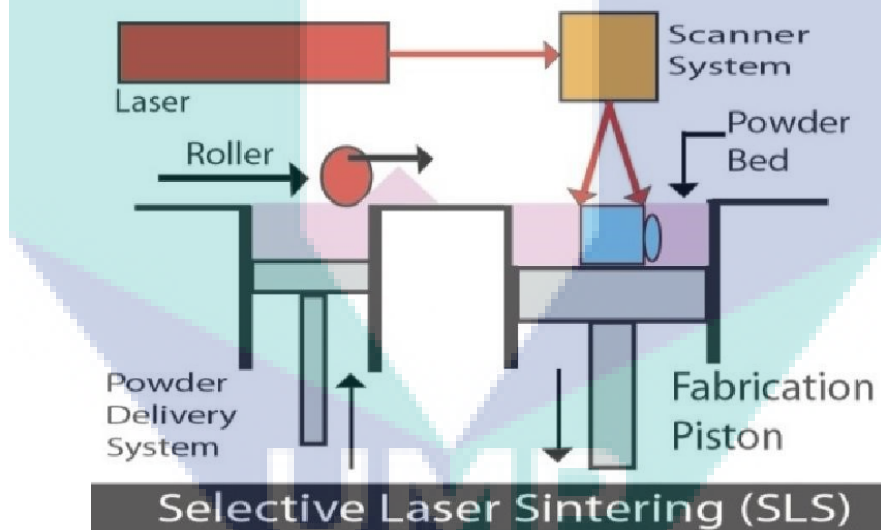


Figure 2.7 Selective Laser Sintering Process Schematics  
Source: Kalyani & Bansal (2016)

Selective Laser Sintering (SLS) is a type of Additive Manufacturing method that fabricates a solid model in sequential cross-sectional layers from a bed of powdery material. These powdered bed is melted or sintered by a high-powered laser into desired cross section model and is later given time to allow solidification as shown in the right schematic in Figure 2.7. The materials used for the powder bed in the case of AFO fabrication are usually different types of thermoplastics which are selected depending on the AFO's desired mechanical properties. The bed is lowered by one unit thickness typically between 0.05 mm and 0.25 mm (Telfer et al., 2012) depending on the accuracy

required and the capability of the bed actuation system of the SLS machine. The aforementioned process is repeated again until all the cross-sectional layers of the model is fully processed.

Table 2.1 Summary of Research on the Application of SLS in AFO Fabrication

No.	Research Title	Author & Year	Material Used	AFO Type	Main Research Findings
1.	Manufacture of Passive Dynamic Ankle-Foot Orthoses Using Selective Laser Sintering	(Faustini et al., 2008)	Rilsan D80 Duraform PA Duraform GF (Nylon 12)	Passive Dynamic Response	Mechanical damping (primary efficacy parameter) is lower than benchmark (Carbon Fibre AFO) by 36% which will affect patient's fatigue level.  Some prototype of SLS AFOs failed the impact resistance test (Fracturing at 2.3 metres)
2.	Mass Customization of Foot Orthoses for Rheumatoid Arthritis Using Selective Laser	(Pallari et al., 2010)	Duraform PA (Nylon 12)	Support Orthosis for Rheumatoid Arthritis	SLS fabricated FO is feasible as it does not exhibit statistic difference in terms of gait parameters when compared with using standard orthoses ( $p < 0.05$ significance level).  Fabricated Foot Orthosis (FO) exhibits rough surfaces due to the noise of scanned 3D Geometry it was designed upon.
3.	Customized 3D printed ankle-foot orthosis with adaptable carbon fibre composite spring joint	(Walbran et al., 2016)	Nylon 12	Passive Dynamic Response	SLS printed AFO component using the Nylon material never fractures in their testing due to high elasticity and exhibits the characteristic of an isotropic material. The disadvantage, however is the high cost of SLS printing.

As listed in Table 2.1, studies shown that the application of SLS AM process to the fabrication of AFOs yielded AFOs that are biomechanically similar to their

traditionally manufactured counterparts. Pallari et al. (2010) performed a gait analysis to evaluate the differences in gait parameters; i.e. walking velocity, cadence, cycle time and stride length between SLS Fabricated Orthosis and standard prescribed orthosis. Based on the results of a one-way ANNOVA test that Pallari performed, they concluded that there were no differences in walking performance of the patients when using the two different types of orthoses. Apart from quantifying walking parameters, Walbran et al. (2016), Faustini et al. (2008) and Pallari et al. (2010) also performed tests to quantify the differences in comfort levels between SLS and standard fabricated orthoses through the use of a standard survey and a Visual Analogue Scale (VAS) scale rating. The conclusion of all mentioned tests is similar with users reporting an acceptable amount of comfort level when wearing the SLS fabricated orthosis.

The most commonly used SLS powder material in these studies is the thermoplastic Polyamide (Nylon 12) with the trade name of DuraForm PA (3D-Systems Company, Rock Hill, SC, USA) and Rilsan D80 (Arkema). These polyamides are widely used due to their biocompatible nature (low irritation to human skin), chemical resistance, toughness and highly durable property (Schmid et al., 2017). In terms of process capabilities, SLS is capable of producing parts with high accuracy due to the fine powder material that it utilises (Singh et al., 2012). Orthosis produced via the SLS process shows high dimensional accuracy as shown in Figure 2.8

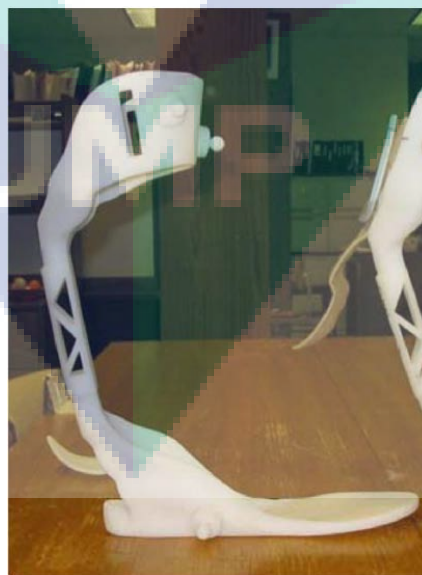


Figure 2.8 Rigid AFO with Single Strut Designed using Topology Optimisation (Faustini et al., 2008)

### 2.4.2 Fused Deposition Modelling (FDM)

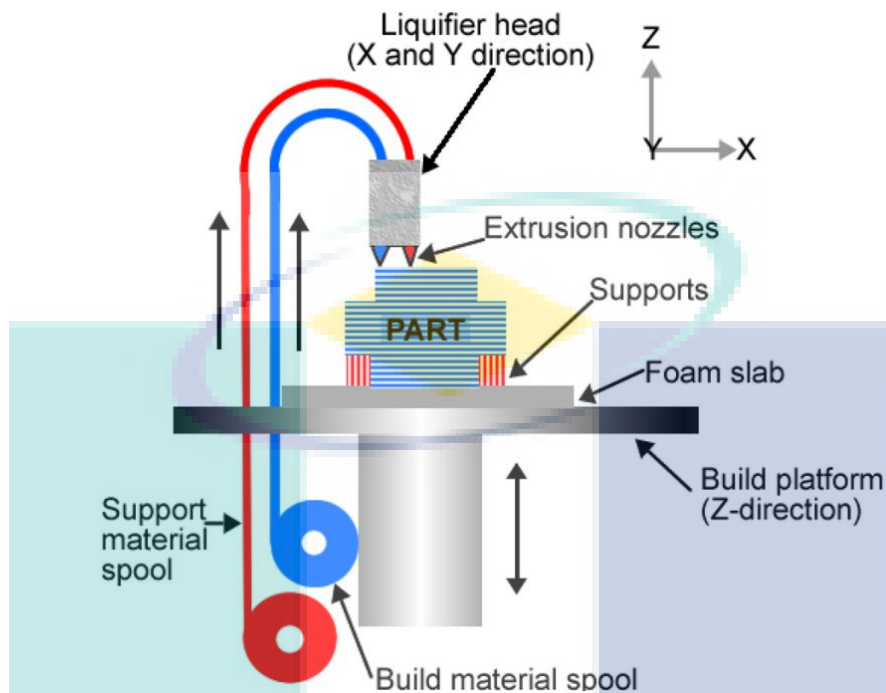


Figure 2.9 Fused Deposition Modelling (FDM) Process Schematics

Fused Deposition Modelling (FDM) is an Additive Manufacturing that involve the use of stock material in the form of plastic filaments, melting them and extruding the melted plastic layer by layer onto a platform to produce a part. The plastic filament is supplied through a spool to a temperature controlled nozzle, in which the temperature is dependent on the respective plastic type. This nozzle travels in a 2D plane (X & Y plane) as shown in Figure 2.9 printing the cross-section of the part. This is repeated layer by layer (by moving the build platform – i.e. the Z-Axis) until the whole part printing process is completed.

Since parts are produced layer by layer, there are problems when producing overhang sections due to their semi-solid state and it will take time for the extruded filament to solidify. These overhang sections have nothing to support their structure with while solidifying which will cause part warping if not rectified. FDM employs support features to support these hanging sections as shown in Figure 2.9 with sections marked in red being the support material. These support feature can be made of other less dense material or of similar material as the build material but printed with lower densities to allow for easier removal.

The FDM process was created by Stratasys Inc. in the 1980s and have grown to be one of the most popular additive manufacturing process due to its many cost-effective applications (Palermo, 2013). With the initial aim of using the FDM process for prototyping purposes, recent trends have shown increasing use in functional applications including the automotive, aerospace, marine, shipbuilding and in the design of medical devices and consumer products. In the fabrication of AFOs, the FDM process have seen an increasing trend in the rate of adaptation for fabrication of ready to use products.

Table 2.2 Summary of Research on the Application of the FDM Process in AFO Fabrication

No.	Research Title	Author & Year	Material Used	AFO Type	Main Research Findings
1.	Dose-response Effects of Customised Foot Orthoses on Lower Limb Muscle Activity and Plantar Pressures in Pronated Foot Types	(Telfer et al., 2013)	Polyactide -PLA (RapMan)	Support AFO for Symptomatic Pronated Foot Type Patients.	The author studied effects of varying angle of posting wearing a customised AFO manufactured using FDM in terms of EMG and foot plantar pressure. Significant desirable results were observed in terms of knee muscle activity as well as posting levels for plantar pressure.
2.	Functionally Optimized Orthoses for Early Rheumatoid Arthritis Foot Disease: A Study of Mechanisms and Patient Experience	(K. S. Gibson et al., 2014)	Polyactide - PLA (RapMan)	Support AFO for Rheumatoid Arthritis.	Efficacy of AFO fabricated using Traditional Methods (SFO) is compared with AFO manufactured via AM (SLS and FDM) via gait parameter (Knee/Ankle Angle and Torque) testing. They found little to no difference (with some test yielding better results in AFOs manufactured via SLS and FDM).
3.	Evaluation of the Walking Performance between 3D-printed and Traditional Fabricated Ankle Foot Orthoses – A Prospective Study	(Lin et al., 2017)	Not specified.	Rigid Support AFO.	Walking parameters (walking speed, stride length, cadence and ROM for knee and ankle joint) were compared between 3D Printed AFO and Traditional AFO. No significant differences were observed.

As exhibited in Table 2.2, there is little to no differences in terms of functional efficacy of AFO between those fabricated using the traditional or standard methods and those fabricated via the Fused Deposition Modelling. To quantify the characteristics of FDM fabricated AFOs, researcher had employed gait parameter testing to quantify the AFO's functionality(Lin et al., 2017), joint torque testing to evaluate the AFO's assistive capabilities (K. S. Gibson et al., 2014) as well as Electromyography (EMG) and foot plantar pressure testing as a measure of comfort (Telfer et al., 2013). In terms of cost, most of reported literature reports cost reduction when switching to FDM methods. However, the downside to the FDM process is that it exhibits strong anisotropic properties (Ahn et al., 2002) depending on the orientation and the print parameters used. Therefore, much attention needs to be placed on knowing the functional forces involved during the use of AFOs.

### 2.4.3 Stereolithography (SLA)

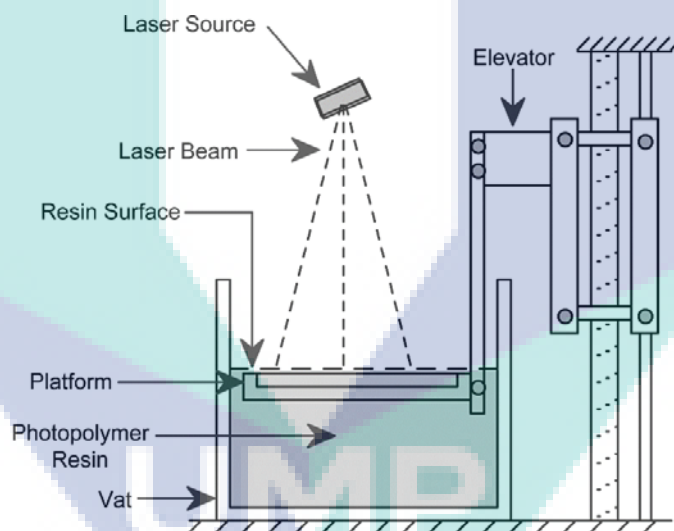


Figure 2.10 Stereolithography (SLA) Process Schematics

Stereolithography (SLA) is a form of AM that involves the use of a light emitting device (which usually emits Ultraviolet light spectrum) to induce photopolymerization in a vat of photopolymer resin (I. Gibson & Bártolo, 2011). Photopolymerization is a process where exposure to light causes chains of molecules to link forming polymers. These formed polymers make up the body of a three-dimensional solid. In the SLA process, the light source is focused to and controlled by CNC to enable high part forming accuracy. Similar to previously reviewed AM processes, SLA process involves the curing of layer by layer of photopolymer resin until the complete product is successfully formed.

CAD is used to drive the light beam to strike selected surface regions of liquid polymer that turns it into solid state forming a solid layer. Once a layer has solidified and adhered to the platform as marked in Figure 2.10, the cycle is repeated for the subsequent layer until the completion of the whole part.

The SLA process possesses high advantage when compared with FDM and SLS AM technologies in terms of build resolution, accuracy and surface finish. Due to this reason, many industries requiring accurate, complex parts to be manufactured such as the micro-electronics industry have resorted to using SLA as their main fabrication method. Beyond its process capabilities, its initial machine cost and equipment cost however is higher than FDM (Marro et al., 2016). Even though its average initial machine cost is lower than the SLS process, the cost for photopolymer or the raw material for the SLA process is the highest among three processes (Pucci et al., 2017). This statement also applies to the fabrication of orthoses where Jumani, Shaikh, & Khaliqdina, 2013 described that the cost of fabrication of AFOs via SLAs is higher than their mass manufactured counterparts.

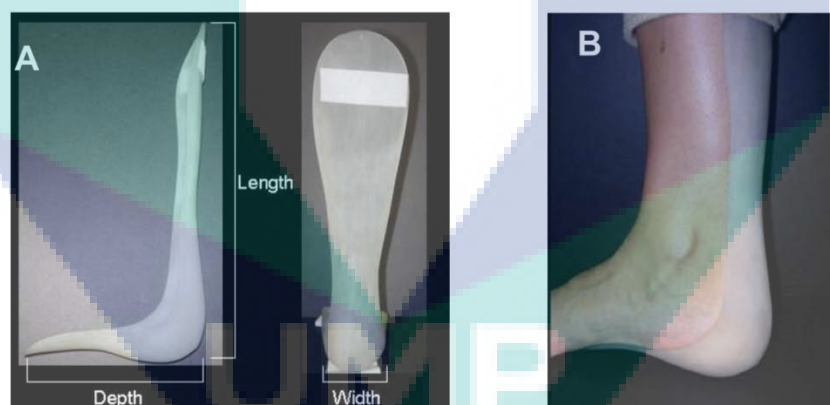


Figure 2.11 Fitting of the AFO Fabricated via the Stereolithography Process  
Source: Mavroidis et al. (2011).

Despite the said cost and drawbacks, many studies have shown significant success when using SLA process to manufacture AFOs as summarised in Table 2.3. Highly customised AFO such as the leaf spring AFO with individually-customised wedges (Mavroidis et al., 2011) is one of the examples where SLA's process capabilities were deemed advantageous. This AFO functions to reposition the limb and provide support which requires a high amount of dimensional accuracy in order for it to perform its task. As shown in Figure 2.11, the AFO fits well to the individual's foot.

Table 2.3 Summary of Research on the Application of the SLA Process in AFO Fabrication

No.	Research Title	Author & Year	Material Used	AFO Type	Main Research Findings
1.	Patient Specific Ankle-Foot Orthoses using Rapid Prototyping	(Mavroidis et al., 2011)	Acura 40 Resin DSM Somos 9120 Epoxy Photopolymer	Flexible Leaf Spring	Using a Leaf Spring Standard Orthosis as benchmark, they found out that RP AFOs are of comparable performance with the advantage of being cost efficient as well allowing more geometric features to be added due to the process capability.
2.	Study of the Design Method of an Ankle Foot Orthosis	(Yasuhiro Mine, Takamichi Takashima, 2006)	Polypropylene Resin reinforced with cords	Flexible AFO	Foot geometry is obtained via scanning a plaster model made from individual's foot.  Near similar gait characteristics with normal AFOs.
3.	Stereolithography Technique for Fabrication of Custom Foot Orthoses: A Cost Benefit Analysis	(Jumani et al., 2013)	Acura 55 Resin	Flexible Arch Support Foot Orthosis (FO)	The FO is designed in CAD software based on measurement obtained from previous researches.  The fabrication time is 6 hours using the iPro 8000 SLA system by 3D systems, inc.  The author concluded that the cost of SLA process is still high during time of publication.

To take advantage of the high dimensional accuracy of the SLA process, researchers also employed 3D scanning to rapidly capture individual's anthropometry (Yasuhiro Mine, Takamichi Takashima, 2006). After obtaining the geometry and processing it in CAD software, the researchers then fabricate it via SLA using Propylene Resins as their fabrication material. Gait characteristics using 3D motion capture and force platform shows near natural walking results when compared with AFO fabricated via traditional methods (Yasuhiro & Takamichi, 2006).



#### 2.4.4 Comparison of SLS, FDM and SLA Processes in Efficacy of AFO Fabrication

As concluded from previous subchapters, all 3 commonly used AM processes are all viable for AFO fabrication with many studies showing the functional performance of AM fabricated AFOs being comparable or in certain cases even better than traditionally manufactured orthoses. However, when compared to each other, these processes have significant differences in a lot of aspects due to their respective process characteristics as described in Table 2.4.

Table 2.4 Comparison of Process Characteristics between SLS, FDM and SLA. Green table shading denotes desirable properties.

Types of AM Process	SLS	FDM	SLA
Types of Material Used	Nylon Polyamide (or combination blended with metal infills)	Widest range of thermoplastic material with varying material properties	Photopolymers
Dimensional Accuracy	Least accurate among listed processes.	Slightly poorer than SLA.	Generally highest part accuracy.
Structural Stability	Stable. Dimension does not change after fabrication.	Stable. Similar to SLS.	Time and Environmental parameters alter size of part or features.
Post-Processing	Requires sanding for better surface quality.	Removal of support structure, commonly with the use of an ultrasonic remover.	Removal of support structures using manual hand sanding.
Surface Finish	Slightly better surface finish than FDM.	Lowest surface finish.	Smoothest surface finish among listed processes.
Part Size	Smallest build size among processes.	Largest. Offers the widest range of build sizes.	Slightly smaller than FDM.
Support Structure	No support structures.	Break away support and water-soluble support.	Breakaway support made from material similar to the build material.

Table 2.4 Continued

Types of AM Process	SLS	FDM	SLA
Run Time	Pre-build warm up and post-build cool down typically adds 2 to 4 hours for each run. Runtimes are material dependant.	Multiple parameters affect FDM run times (layer thickness, print path, Z-Axis height). Generally, FDM takes the longest time to print.	Runtimes are material dependant and are similar to SLS process.
Relative Cost	High Machine Cost. Low Material Cost.	Low Machine Cost. Low Material Cost.	Median Machine Cost. Expensive Resin.

Since low cost fabrication is part of the main objectives for this research, the FDM process proves to be the best candidate, having the lowest cost among the list of AM processes both in terms of initial machine cost and material cost (Schrank & Stanhope, 2011). In terms of process flexibility, FDM is also the most favourable as the process supports a wide range of thermoplastic as printing material. This allow the inclusion of various customised characteristics to the AFO such as variable stiffness and strengthened support at specific regions. Physical shortcomings such as low surface quality could be solved by proper post-processing method such as grinding and coating with a smoother plastic layer. Structural integrity of FDM however is highly irregular, varying from one part to another depending on process parameters. This could be solved by properly modelling the structural properties of FDM printed parts and applying FEA methods to ensure strength is imparted on functional regions (Hopkinson & Dickens, 2003).

## 2.5 Structural Optimization

Structural Optimization (SO) is an optimization process in which the optimal design of a load carrying structure is obtained via modification of the original geometry based on a given set of objective, constraints and limits. Traditionally SO is performed manually using the iterative-intuitive process that generally consist of: suggestion of design, evaluated design requirements (for example via Finite Element Analysis – FEA) and in the end, a new improved design is proposed if the evaluation yields positive results (Christensen, 2009). This approach presents many drawbacks as its efficacy relies on the designer’s knowledge, experience and intuition. Alterations to the design is made using trial and error which can be very time consuming and may sometimes result in a

suboptimal design (Olason & Tidman, 2010). Recent CAD software developments had shown that more and more software packages implementing Structural Optimization toolbox within their system. These implementations have allowed seamless optimization operations be performed on the design as most of them integrates their SO packages with their FEA packages. Although such advancements have been made, they are still based on the same SO fundamentals. Most SO study can be presented mathematically as describe in Equation 2.1 (Peter W. Christensen, 2009). An SO problem can be divided mainly into main items namely objective functions, design variables and state variables.

$$SO \begin{cases} \text{minimize } f(x, y) \text{ with respect to } x \text{ and } y \\ \text{subject to } \begin{cases} \text{behavioral constraints on } y \\ \text{design constraints on } x \\ \text{equilibrium constant} \end{cases} \end{cases} \quad 2.1$$

Objective function( $f$ ). As the name states, objective function is the function formulated based on the desired structural properties. This function returns a number indicating the goodness of the design. The common goal is usually minimization of the return number, i.e. we usually define smaller values having better desirability. The most common parameters used are weight, displacement in a given direction, effective stress and cost of production.

Design variable( $x$ ). A function or vector that describes the design which can be altered during optimization, which can either be the geometry or choice of material. An example of such function is a curve equation used to describe the geometry of a design.

State variable( $y$ ). A function or vector that represents the response of the structure resulting from the optimization process which can either be displacement, stress, strain or force.

### 2.5.1 Types of Structural Optimization

Structural Optimization (SO) are generally classified depending on how the optimisation process affect the design variables or commonly called the geometric features. Structural optimization is mainly divided into three classifications namely Sizing Optimization, Shape Optimization and Topology Optimization.

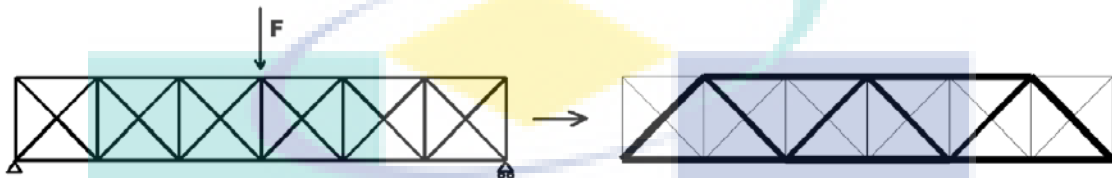


Figure 2.12 Sizing Optimization on a Truss Structure  
Source: Olason & Tidman (2010)

Sizing Optimization focuses on optimizing geometric features which are constrained by length dimensions such as structural thickness and cross-sectional areas. Figure 2.12 is an example of Sizing Optimization on a truss structure with radii as one of the design variable. To accommodate for the load at the middle of the truss structure, the radii of some of the individual truss members are increased. Sizing Optimization is mostly used in designs which are constrained to process capabilities or costs; where certain designs must be made from standard parts.



Figure 2.13 Shape Optimization on a Structure with Circular Holes  
Source: Olason & Tidman (2010)

Shape optimization involves optimizing the form or contour within design boundary. Only the intermediate region within the boundary will be altered usually to promote uniform stress distribution within the part. Similar with sizing optimisation, the geometric features (number of holes, beams, truss and so forth) of the design are already determined when the optimisation is performed. Shape optimisation will not result in the occurrence of new geometric features in the output design. As exhibited in Figure 2.13, In contrast with the two other SO types, shape optimisation's design variable each affect many elements (Olason & Tidman, 2010).

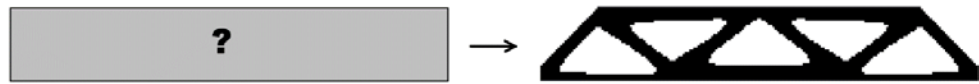


Figure 2.14 Topology Optimization Performed on a Structure with only Boundary Parameters

Source: Olason & Tidman (2010)

Topology Optimization (TO) is the most general form of Structural Optimisation (Rao, 2009). In contrast with both previously mentioned SO method, the design variables in TO are not predefined. The resulting optimised shape or geometry is also hard to predict. In topology optimization, the overall structure is divided into discrete elements (mesh) and is discretised by using the Finite Element Method (FEM). These discrete elements are later assigned integers (0 or 1) based on whether they fulfil the objective functions that is set. The algorithm determines which element to keep or which element to remove based on the assigned integer (0 to remove, 1 to keep) hence the name Isotropic Solid or Empty (ISE) given to the resulting topology. Due to these assignment of these integers, the total numbers of solution when using Topology Optimisation is  $2^N$ , where N is the number of elements. This high complexity limited their application during the earlier years due to the fact that FE-models could easily reach hundreds of thousands of elements (Bendsoe & Bendsoe, 1995). As computational power increases throughout the years, the aforementioned problems of implementing SO ceased to be a problem and many researchers have currently studied on the algorithm's application to real-world product designs.

### 2.5.2 Application of Structural Optimisation in AFO Design

Many research works related to Structural Optimisation have appeared over the last decades in an array of fields ranging from electrical components, medical apparatus to automotive structures. To show the diverse capabilities of the Structural Optimisation, a list of summarised past works on SO Application, their specific goals and methods employed from multiple applied fields are presented in Table 2.5.

Table 2.5 Summary of Research Works Applying Structural Optimisation

No.	Research Title	Author & Year	SO Method Employed	Optimisation Goals
1.	Suspension Modelling and Optimization Using Finite Element Analysis	(Kilian et al., 2003)	Topology Optimisation, Shape Optimisation, Combination of both	Torsion, Bending, Sway Mode Frequencies of Hard Disk Drive (HDD) contact pin for different HDD operating conditions.
2.	Crashworthiness Design of Transient Frame Structures Using Topology Optimisation	(Yasuhiro Mine, Takamichi Takashima, 2006)	Topology Optimisation	Minimisation of acceleration, displacement of car chassis for crash conditions.
3.	Topological Optimization for Designing Patient-Specific Large Craniofacial Segmental Bone Replacements	(Sutradhar et al., 2010)	Topology Optimisation	Output most optimised structure to replace missing bone with the most minimum amount of material. Considerations include: structural integrity, biological considerations as well as functional considerations (such as passages for respiratory airflow).
4.	Integrated Topology and Shape Optimisation Software for Compliant MEMS Mechanism Design	(Jang et al., 2008)	Topology Optimisation Shape Optimisation	Output compliant MEMS actuator; a gripper and a micro force inverter. Constraints include spatial constraints (optimised design must fit stated space requirements) and stress concentrations. For the shape optimisation process, the design is limited to control points set by the researchers.

As shown in most research concluded from Table 2.5 as well as based on exhaustive literature reviews, the most commonly used and most effective Structural Optimisation method is Topology Optimisation. The goal of most of the listed research was to investigate the capabilities of TO methods in producing the most optimised design based on set constraints instead of actual applications to real-world manufacturing and its cost saving feasibility. Generally, Structural Optimization techniques are best applied for products intended for mass production where even a miniscule amount of cost saving per product would accumulate leading over to substantial savings (Belegundu & Chandrupatla, 2011). This however, is also largely dependent on the manufacturing process used. The resulting optimised design from Shape and Topology Optimisation would usually result in more complex shapes due to the shape alteration and material

removal at various regions. For traditional plastic manufacturing methods such as plastic injection moulding and vacuum casting, increasing the complexity of the design would increase the overall production costs due to higher moulding and tooling costs.

As of the writing of this thesis, the number of research applying structural optimisation techniques in AFO fabrication is still small with some applying basic sizing optimisation techniques to actuated ankle foot orthosis (Castiblanco & Shareef, 2017).

### 2.5.3 Considerations for Implementation of Structural Optimisation for Parts Fabricated using Fused Deposition Modelling

As previously mentioned, the process capabilities greatly affect the efficacy of the implementation of Structural Optimisation method (Olason & Tidman, 2010). In the case of Additive Manufacturing process, the FDM process is able to produce extremely complex parts with good accuracy and without incurring additional costs (Wong & Hernandez, 2012). Topology Optimisation in particular provides a mean for intelligently exploiting this high degree of design freedom.

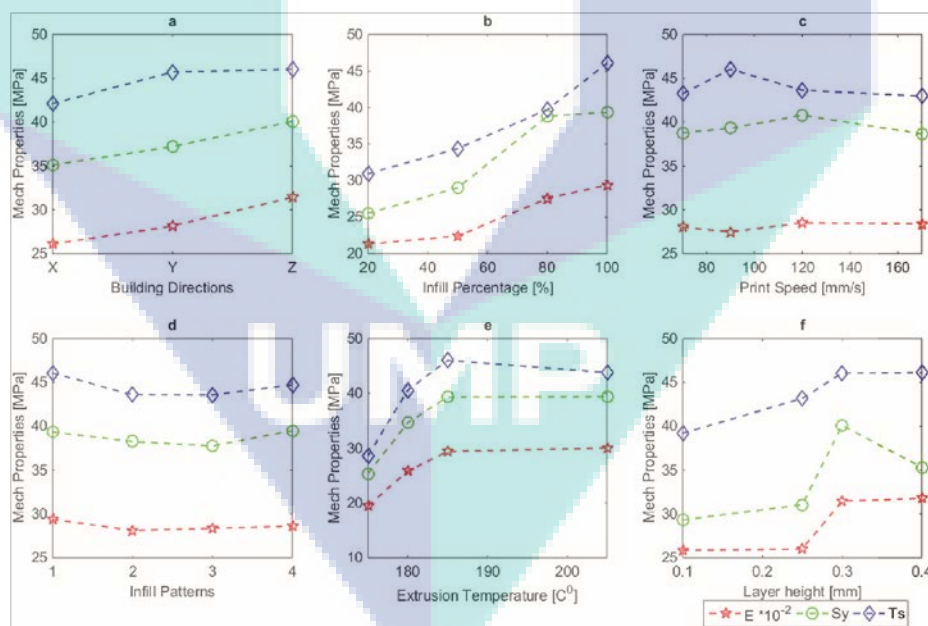


Figure 2.15 Mechanical Properties - Tensile Strength [MPa] caused by (a) building direction, (b) infill percentage, (c) printing speed, (d) infill patterns, (e) extrusion temperature and (f) layer height, where E is young's modulus, Sy is the yield strength and Ts is the tensile strength

Source: Ahn et al. ( 2002).

However, there are certain considerations that needs to be taken in order for Topology Optimisation to be feasible in designing a component made via FDM. The most

important consideration is the anisotropic nature of parts produced by the FDM process. As shown in Figure 2.15, the mechanical properties of FDM fabricated parts are highly dependent on FDM process parameters namely the build direction, infill percentage and pattern, extrusion temperature as well as the layer height (Ahn et al., 2002). This variation of mechanical properties also differs with different manufacturers even for the same plastic material type. Acrylonitrile Butadiene Styrene (ABS) is one of the example of such case.

Table 2.6 Summary on Research Investigating Mechanical Properties of Fused Deposition Modelling Components

No.	Research Title	Author & Year	Machine Model & ABS Type	Mechanical Properties (Average Tensile Stress)
1.	Determination and Comparison of the Anisotropic Strengths of Fused Deposition Modelling P400 ABS	(Upadhyay et al., 2017)	Dimension SST-768 ABS P400	X-Orientation: Untested Y-Orientation: 19 MPa Z-Orientation: 15 MPa
2	Effect of Build Orientation on Mechanical Properties of Rapid Prototyping (Fused Deposition Modelling) Made Acrylonitrile Butadiene Styrene (ABS) Part	(Ashtankar et al., 2013)	Dimension BST-768 ABS P400	X-Orientation: Untested Y-Orientation: 15.2 MPa Z-Orientation: 11.6 MPa
3.	Mechanical Characterization of Parts Fabricated Using Fused Deposition Modelling	(Bellini & Güçeri, 2003)	Stratasys 1650 FDM ABS	X-Orientation: 16.0 MPa Y-Orientation: 11.7 MPa Z-Orientation: 7.6 MPa
4.	Fused Deposition Modelling Tensile Strength Characterisation	(Vidakis et al., 2016)	Dimension Elite ABS	X-Orientation: Untested Y-Orientation: 19.4 MPa Z-Orientation: Untested
5.	Mechanical Properties of Components Fabricated with Open-source 3D Printers Under Realistic Environmental Conditions	(Tymrak et al., 2014)	MOST RepRap Natural ABS	X-Orientation: Untested Y-Orientation: 27.7 MPa Z-Orientation: Untested

Table 2.6 summarises the directional mechanical properties of several types of commercially available ABS fabricated using different FDM Machines. All denoted axis (X, Y, Z) have been standardised across literature according to Figure 2.16. As we can see from the table, there are large variance of mechanical properties values even between plastic of the same type. This this difference is due to different processing methods and



material additives used by different manufacturers in order to produce the FDM filaments. Even materials made by the same manufacturer [as per literature no. 1, 2, 3 & 4] but fabricated with different machine models exhibited a significant difference in mechanical properties. This occurrence is due to different machine parameters (extrusion temperature, platform temperature, ambient temperatures during process) employed in different FDM machine models even for the same manufacturer. Since Structural Optimisation deals with stress and deformation principles, proper material testing need to be performed for specific material and machine used in order for the SO method to yield accurate results. In this thesis, the material are tested according to different type of orientations as shown in Figure 2.16. Material testing is performed based on ASTM's Standard Testing Procedure, ASTM D638 – Testing Procedures for Rigid Plastics with conditioning methods abiding Procedure A of Practice D618 – 13 Standard Practice for Conditioning Plastics.

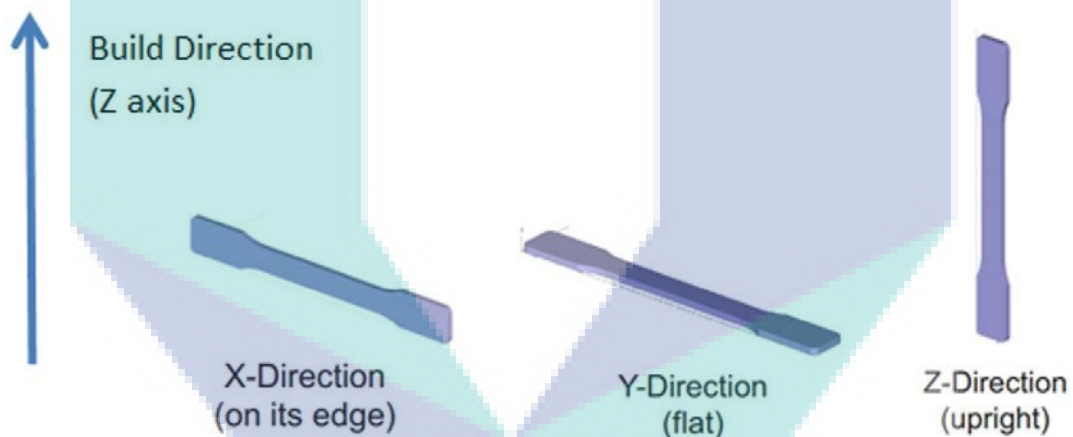


Figure 2.16 Standardised Axes Used to Describe Build Orientation Across Literature

## CHAPTER 3

### METHODOLOGY

#### 3.1 Introduction

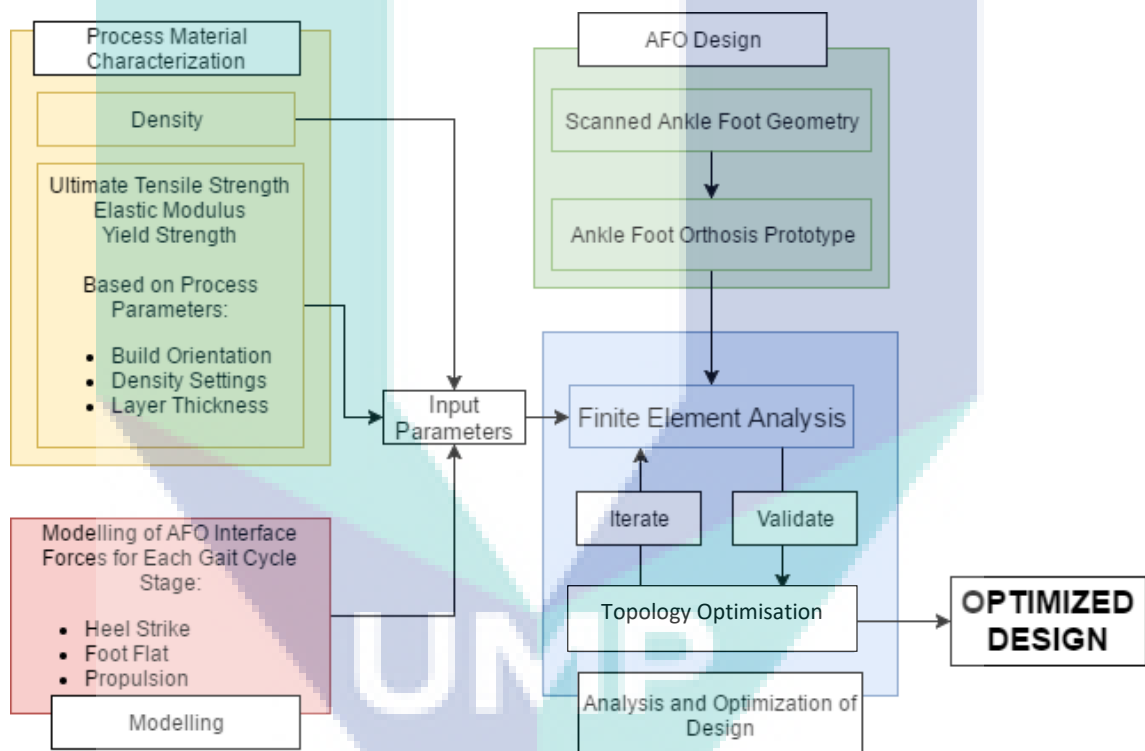


Figure 3.1 Research Flow Chart

The proposed methodological framework is divided into 4 phases namely the material characterisation, modelling, AFO design and analysis and optimization of design as illustrated in Figure 3.1. In terms of sequence, the research starts with the AFO Design, where the 3D scanning process of the limb is performed and based of this scanned geometry, a preliminary AFO prototype is designed. The scanned geometry is obtained by scanning the limb of the wearer using a low-cost 3D Scanner. Before FEA is performed on the initial AFO design, several required input parameters have to be

fulfilled. A set of specimens made by FDM using different process parameters (namely filament thickness and build density) is prepared and the properties of each of these specimens are tested using Tensile Test. The boundary conditions for the FEA is also modelled for 3 main load bearing phases in the gait cycle namely the heel strike, single stance and propulsion. FEA is performed for each aforementioned gait support phases with the material properties that is selected in the previous material characterization phase. The aforementioned gait cycle phase which yields the lowest factor of safety is chosen for the next research stage. Topology optimisation is then performed based on the said gait phase loading conditions. Once the shape optimisation phase is completed, the resulting design will be validated in terms of material usage, structural integrity and overall process cost savings using a proposed cost calculation model.

### 3.2 Ankle-Foot Region Scanning

The purpose of this stage is to obtain the foot geometry in a fast, efficient and costly manner. The lower limb geometry is scanned using Microsoft’s Kinect device which is a relatively inexpensive device. The Skanect software by Occipital, which is a free trial software was used to take advantage of the built-in Kinect IR Depth sensor for 3D scanning.

Table 3.1 Microsoft Kinect 360 Technical Specifications

<b>Microsoft Kinect 360 Specifications</b>	
Viewing Angle	57° Horizontal, 43° Vertical
Vertical Tilt Range	27° Either up or down
Frame Rate (Depth and RGB Colour Scheme)	9Hz ~ 30Hz (Resolution Dependent)
Effective Distance Range	0.7m – 6m

The Kinect Model used in this study is the Microsoft Kinect 360 with specifications as stated in Table 3.1. The RGB Sensor and Depth Sensor module are placed in location marked as in Figure 3.2.

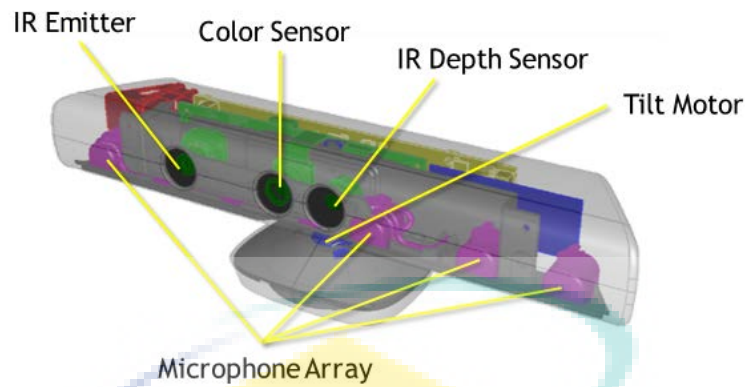


Figure 3.2 Major Components of a Microsoft 360 Kinect Device

The RGB camera stores three channel data at a resolution of 1280 x 960 thus making capturing colour image possible. This coloured image is mainly used as texture data for the 3D model and is mostly an aesthetic feature. The Infrared (IR) Emitter emits an infrared wavelength light beam to an object and the resulting reflected beam is captured by the IR Depth Sensor giving the distance value from the object to the sensor creating point clouds in 3D Space. Using the aforementioned Skanect software, these point clouds are triangulated to generate a mesh and is further processed to generate 3D Models.



Figure 3.3 Kinect 3D Scanning Setup

In the scanning phase, the individual's leg is placed in a slanted position on a transparent platform made from Polymethyl Methacrylate (PMMA) as shown in Figure 3.3. This is done because the IR Depth Sensor is not able to pick up transparent object's detail (due to the IR light rays going pass the object due to transparency) causing the

platform to be excluded from the scanning process. This allows for the scanning of the full individual's foot geometry. The individual was asked not to exert too much pressure on the platform to ensure that the scanner was able to capture the actual resting geometry of the foot, not the flattened one. The individual scanned is a healthy, 27 years old male weighing 84 kg with the height of 174 cm.

The Skanect software converts point clouds to 3D surface geometry in which this surface geometry is later water-tight processed (holes, crevices are sealed, closed) and is further processed to produce a solid geometry as shown in Figure 4.1. This geometry initially is of high resolution containing 183,342 faces and 91,673 vertices which is too large for most 3D Computer Aided Modelling (CAD) software to effectively handle. The 3D Model is simplified using the MeshLab software using the Quadratic Edge Collapse Decimation tool, a tool used to remove redundant faces without losing too much geometry accuracy. The final geometry is reduced to 1,000 faces and 502 vertices enabling it to be imported into Autodesk Inventor CAD software.



Figure 3.4 Post-Processed 3D Geometry of Scanned Limb

To determine the accuracy of the scanned model, actual measurements of the scanned limb is compared with scanned 3D limb geometry measurements. The measurement for the scanned 3D limb geometry were done using MeshLab's virtual

measuring tool while the actual limb was measured using rulers. The anthropometric features that were measured are shown in Figure 3.5.

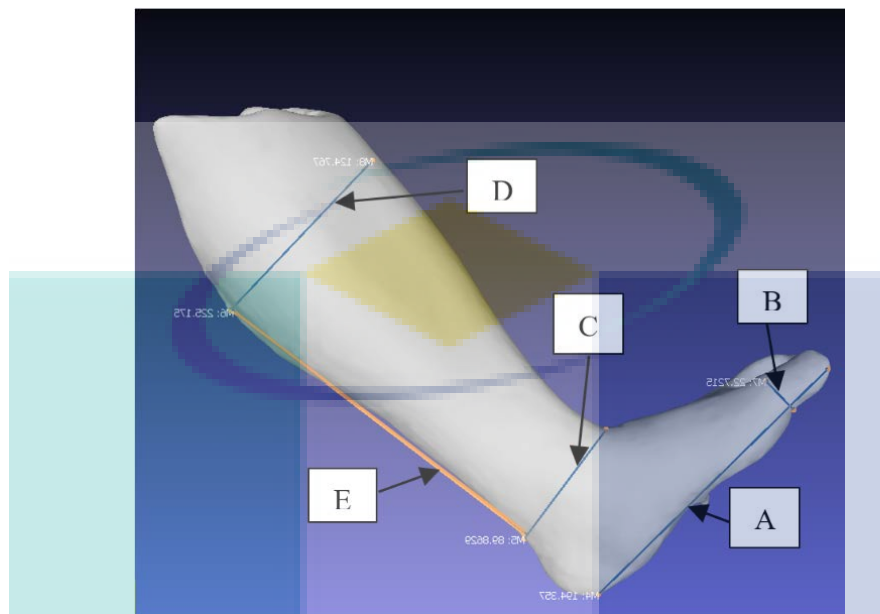


Figure 3.5 Foot Anthropometry Measurements

### 3.3 FDM Material Characterization

The test procedures; from the fabrication and preparation of the tensile specimens to the tensile testing is performed based on ASTM D638 – 02a Standard Test Methods for Tensile Properties of Plastics.

#### 3.3.1 Fabrication and Preparation of Specimens

Both the test specimens and orthosis are fabricated using the Zortrax M200 3D printer with Acrylonitrile butadiene styrene (ABS) filaments. Z-ABS (The trade name for Zortrax's ABS Filaments) is categorised as a semi-rigid plastic, therefore; the Type-I specimen parameters were chosen with reference to the aforementioned ASTM test standards.

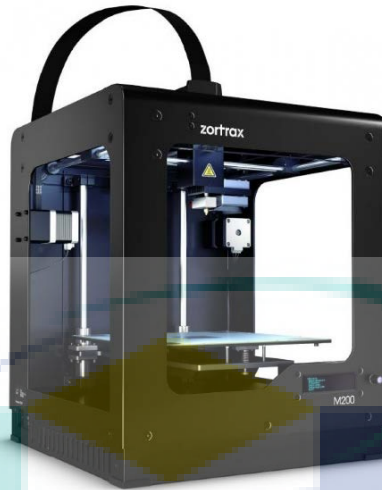


Figure 3.6 Zortrax M200 3D Printer

The dimensions for the test specimens are as shown in Figure 3.4. The thickness of the test specimen is 5 mm, giving a cross-sectional area of  $65 \text{ mm}^2$  around the neck of the test specimen. The 'X' marking in the diagram are the locations of the jaw ends used to clamp the tensile test specimen.

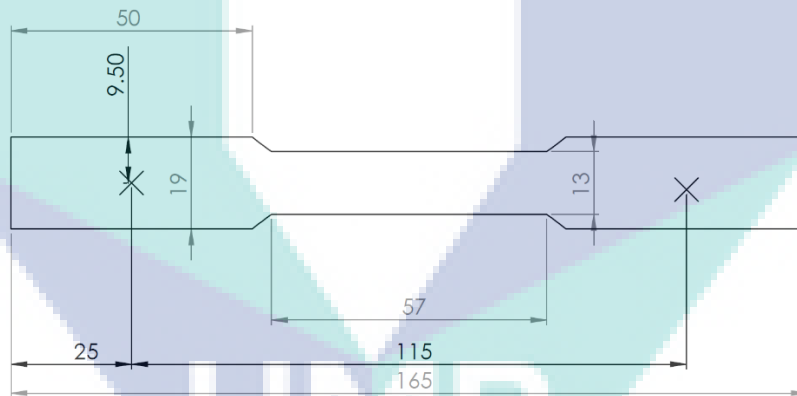


Figure 3.7 Tensile Test Specimen Dimensions for Z-ABS Material

In accordance to the referred ASTM standards, five test specimens for each anisotropy axis were tested. In FDM Process, the material anisotropy is dependent on the build orientation of the components. There are 3 main ways for a component to be oriented during the FDM Process which is either standing, laid flat or laying on the side as shown in Figure 3.5 which will be referred to in this thesis as A (standing-yx plane), B (laid flat-xz plane) and C-Orientations (laying-yz plane) respectively.

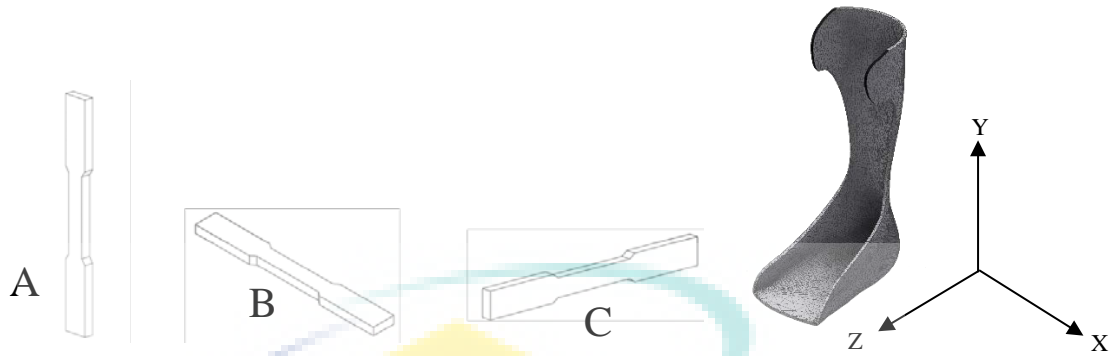


Figure 3.8 Build Orientations with Respect to AFO and Coordinate System

Two parameters can be varied during 3D Printing which are Layer Thickness and Infill Density. Layer thickness can be varied to 4 values (0.09mm, 0.14mm, 0.19mm and 0.29mm) while infill density, as shown in Figure 3.7 can be adjusted to 3 values (Low, Medium and High). Printing location of specimens are as shown in Figure 3.9.

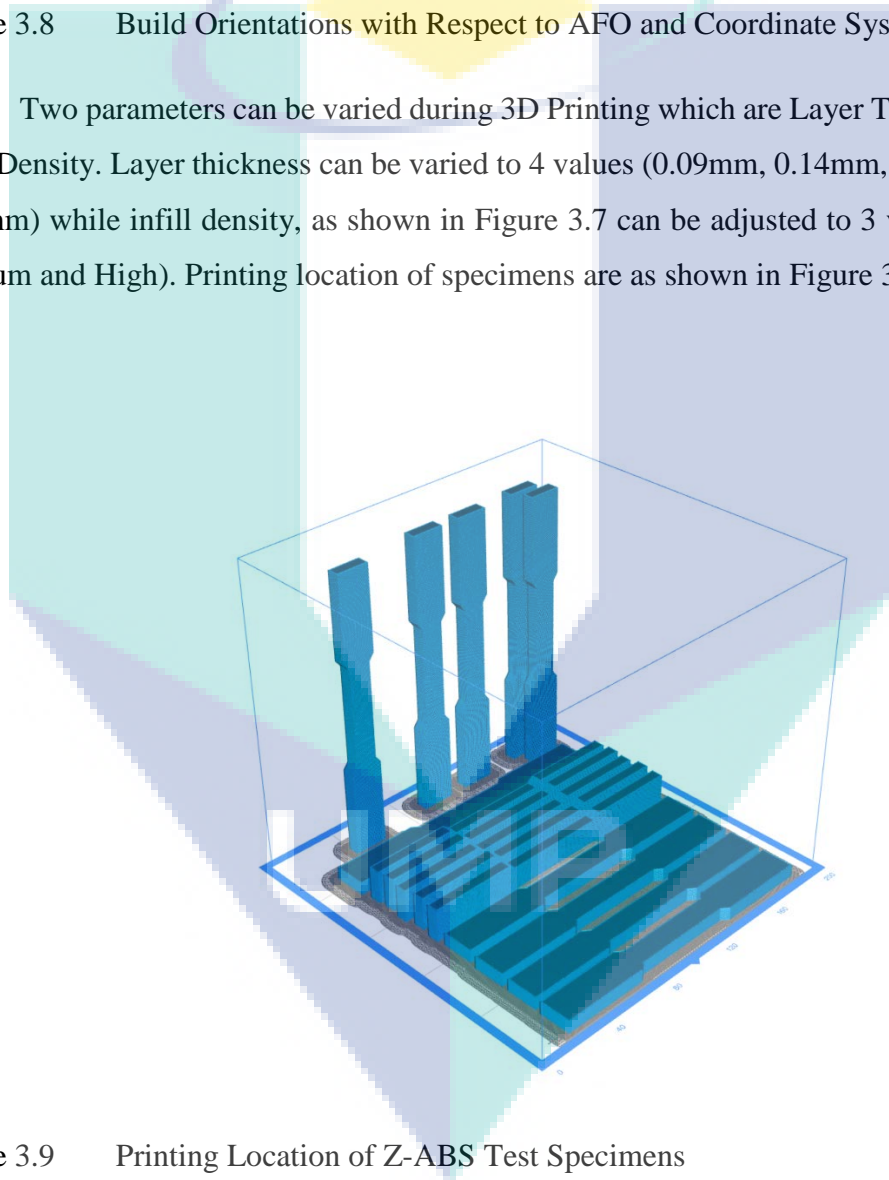


Figure 3.9 Printing Location of Z-ABS Test Specimens

The manufacturer, Zortrax did not include specifically the densities of parts printed using the FDM machine through said infill density settings. Given is only the density of the ABS filaments which is at  $1000 \text{ kg/m}^3$ , referenced from the Zortrax Material Safety Data Sheet (2016). To estimate the density of build settings as accurately



as possible, the images of the printing raster similar to the one in Figure 3.10 is converted into black and white using MATLAB's image to black and white command based on RGB Level. The white region represents the solid area while the black region represents unfilled space. After image is converted into black and white the white to black area ratio is calculated using MATLAB.

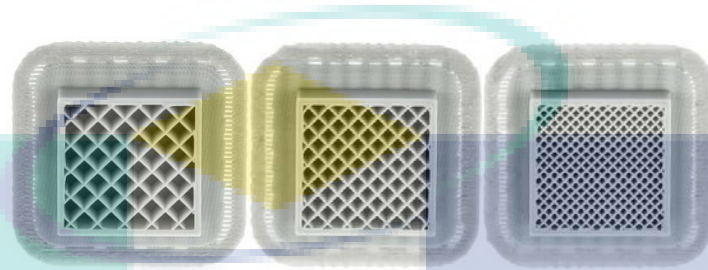
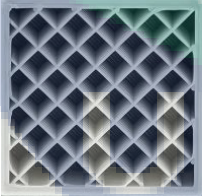
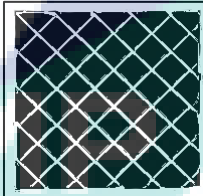
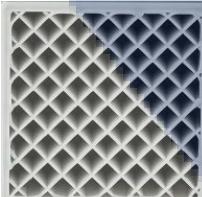
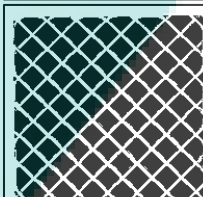
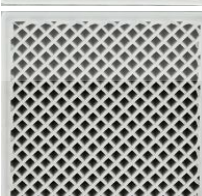
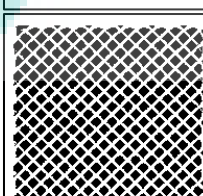


Figure 3.10 Infill Density Settings (From Left; Low, Medium and High Settings Respectively)

This ratio is then factored by the density of solid ABS filaments as mentioned previously to obtain the exact density to all infill density settings. Results are as summarised in Table 3.2.

Table 3.2 Build Settings Density Calculation Using Black and White Image Mapping Method

Build Orientation	Raster Image	Black & White Raster Image	RGB Level	Percentage White & Estimated Density
LOW			191	35.7881 % Density = 357.881 kg/m <sup>3</sup>
MEDIUM			181	42.9186 % Density = 429.186 kg/m <sup>3</sup>
HIGH			191	56.5408 % Density = 565.408 kg/m <sup>3</sup>

For each of these parameters varied, 15 specimens will be tested – 5 for each build orientations (5×3). Infill density is set to low when varying layer thickness parameters whereas when varying infill density, the layer thickness is set to a constant 0.29 mm. This is done to isolate the effects of other build parameters when investigating a particular build parameter. The overall design of experiment is shown in Table 3.3.

Table 3.3 Specimen Build Parameters and Specimen Numbers

FDM Parameters	Test Values	No. of Specimens
Layer Thickness (Infill Density constant at Low)	0.09 mm	15
	0.14 mm	15
	0.19 mm	15
	0.29 mm	15
Infill Density (Layer Thickness constant at 0.29 mm)	Low	15
	Medium	15
	High	15

After the specimens are fabricated according to different test parameters, they are conditioned inside a dry cabinet with the temperature of  $23\pm 2^{\circ}\text{C}$  and  $50\pm 5\%$  humidity for 48 hours in accordance to Procedure A of Practice D618 – 13 Standard Practice for Conditioning Plastics for Testing by ASTM.



Figure 3.11 Test Specimens Conditioned in a Dry Cabinet with Temperature Control

### 3.3.2 Tensile Test Procedures

The machine used for the tensile test is the INSTRON 3300 Series Dual Column Table Top Universal Testing System (UTS). The said UTS machine uses a combination

of motor and gear reduction system the crosshead up and down to apply compressive or tensile forces to the sample. The motor speed controls the speed of the crosshead. Depending on material type and the geometry of the test specimens, load cells with different grips are attached to the crosshead. The lower grip is stationary to the fixed base plate of the frame while the upper grip moves in vertical upward or downward direction.

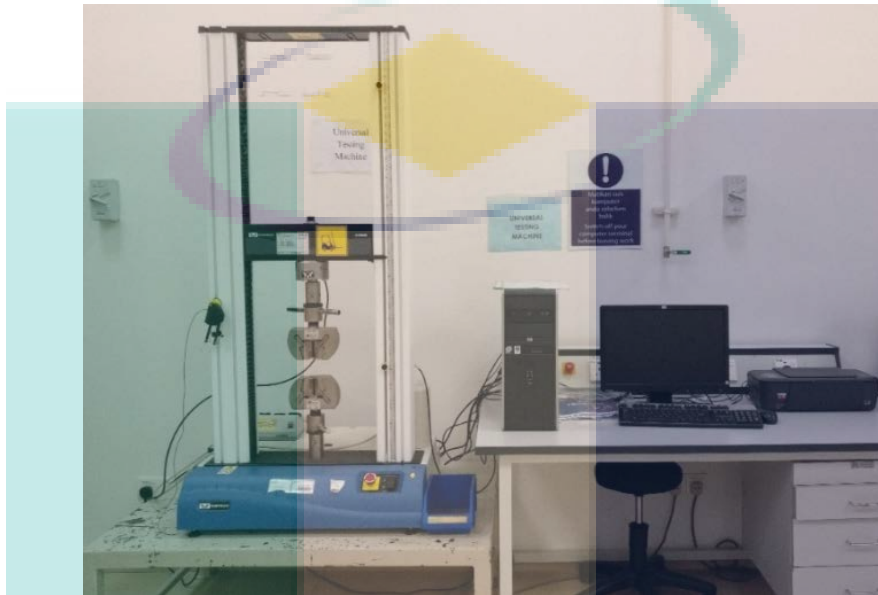


Figure 3.12 INSTRON 3300 UTS Machine and Test Setup

The UTS machine settings are set according to Table 3.4. The speed of testing (5mm/min) is based on the ASTM D638 – Testing Procedures for Rigid Plastics. The end of test criteria is set to when the load abruptly drops to 10N (Fracture). This value is selected due to the semi-rigid nature of ABS plastics. All calculated parameters in Table 3.4 are presented as mean values of 5 samples for each process parameter set.

Table 3.4 INSTRON UTS Machine Testing Parameters

Test Parameters	Values
Speed of Testing (Extension Rate)	5 mm/min
Data Capture Interval	50 milliseconds (ms)
End of Test Criteria	Load Threshold (Drop to 10N)
Parameters Calculated	Maximum Load Tensile Stress at Maximum Load Tensile Strain at Maximum Load Load at Break Tensile Stress at Break Tensile Strain at Break Tensile Stress at Yield

### 3.4 Modelling of the AFO

The AFO study is modelled as a linear elastic anisotropic body. The reason why a linear analysis is chosen is due to the forces as well as material characteristics implemented in this study are of linear behaviour; linear forces as well as linear behaviour of the anisotropic material respectively. The parameters of interest in this study are the resulting stresses, strains as well as the deformation at various regions of the AFO geometry. The FEA simulation is performed using Autodesk's In-CAD NASTRAN FE Version 2018.1 Software.

#### 3.4.1 Geometrical Model

The element shape used in this study is the parabolic-tetrahedron (CTETRA) which is an isoparametric tetrahedron element with four vertex nodes and up to six additional midside nodes (giving a total of 10 nodes) as shown in Figure 3.13. The CTETRA element is widely used in complicated systems, such as geometry with complex extrusions, turbine blades and so forth. It is modelled as a SOLID element with the anisotropic material (MAT9) properties. SOLID elements have only translational degrees of freedom (DOF). No rotational DOF are used to define SOLID elements.

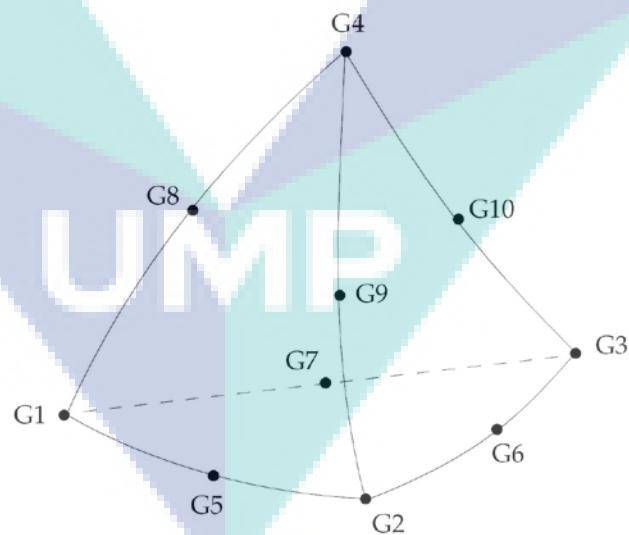


Figure 3.13 Parabolic-Tetrahedron Element Nodes (10 Nodes Total)

The NASTRAN software calculates element stresses ( $\sigma_x$ ,  $\sigma_y$ ,  $\sigma_z$ ,  $\tau_{xy}$ ,  $\tau_{yz}$ , and  $\tau_{zx}$ ) at the elements center and gauss points. These stresses are extrapolated to obtain stresses at the corner grid points.

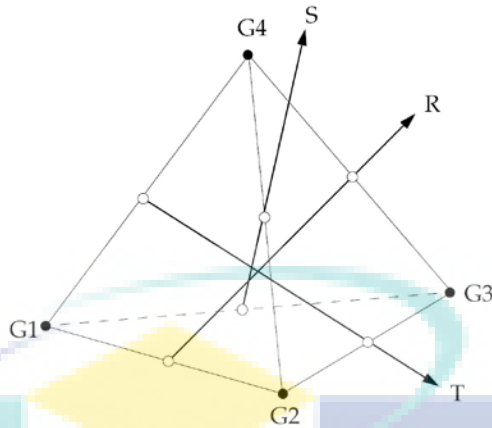


Figure 3.14 Parabolic-Tetrahedron (CTETRA) Element Coordinate System

The CTETRA element coordinate system is derived from 3 vectors namely vectors R, S and T which join the midpoints of opposite edges as shown in Figure 3.14. The origin of the coordinate system is located at node G1. Nodes G1, G2 and G3 define a triangular face.

Before deciding geometry meshing parameters, a convergence study is performed to investigate which meshing parameters yields the highest accuracy. Theoretically as the mesh is refined and the mesh size is reduced, the accuracy of the next iteration will increase. This also leads to higher computational requirements to solve a given model. As mesh elements decrease in size, they will eventually reach a point of diminishing returns on the level of accuracy compared to the computational overhead and time required to compute a result. Thus, a convergence analysis is performed to get the best mesh parameter giving the best accuracy without causing excessive computational overheads. The convergence analysis parameters used are listed as in Table 3.5.

Table 3.5 Convergence Analysis Settings

Parameters	Values
Maximum Number of Iterations	20
Stop Criteria	Error, $\varepsilon < 0.1\%$
Geometry Refinement Threshold	0.75
Results to Converge	Von Mises Stress, Displacement
Geometry Selection	Whole AFO Geometry

In Autodesk In-CAD NASTRAN, the software automatically generates mesh parameters in between iteration. The only inputs to the NASTRAN convergence analysis module are as per Table 3.5. The convergence analysis is done to the whole AFO

Geometry with Von Mises stress and displacement as the main result parameters, as these two are the main point of interest in our static analysis. The geometry refinement threshold indicates the location of where the software would refine the mesh with the value of 0.75 indicating that the software is set to refine mesh in all areas where stresses are within the 25% of the maximum stress value. The number of iterations as well as the stop criteria is set at such a figure to allow us to clearly ensure that the analysis reaches convergence before completion. The plot in Figure 3.15 shows the convergence plot for the AFO case study.

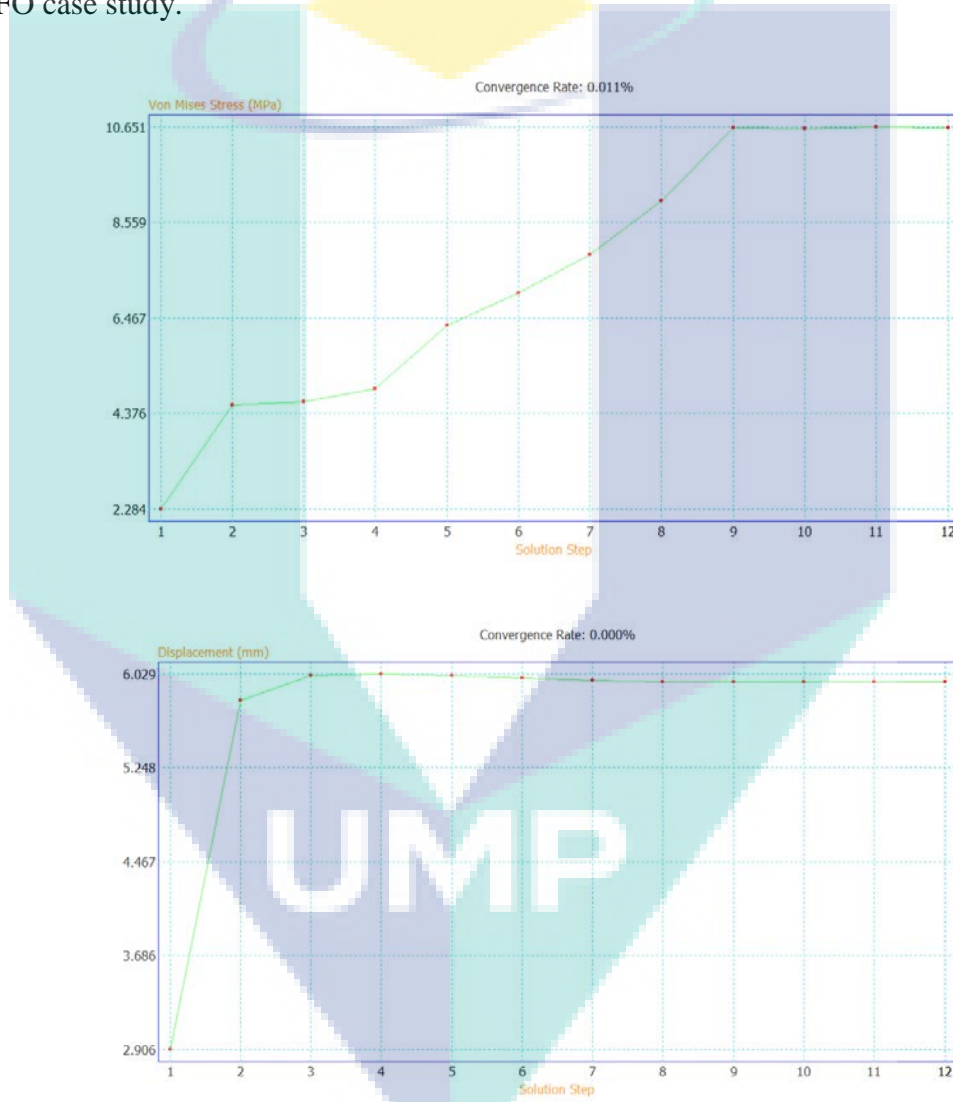


Figure 3.15 Convergence Plot for different Mesh Iterations (Top – Von Mises Stress, Bottom – Displacement)

As shown in the convergence plot, the 9<sup>th</sup> iteration is the point of convergence where mesh refinement beyond that particular point yields no accuracy benefits. The convergence rate for Von Mises Stress (MPa) and displacement (mm) are 0.011 % and

0% respectively. The convergence rate indicates the result difference beyond the selected point which in this case, the convergence rate is excellent.

The 9<sup>th</sup> iteration mesh parameters are as listed in Table 3.6. The element size is 9.1067 mm with a refinement ratio of 0.9. Refinement ratio indicates the level of uniformity of mesh sizes, with higher values meaning more uniform mesh sizes. This mesh parameters are also used in the Topology Optimisation analysis. The elements are idealised as a solid even though in nature the geometry of the actual fabricated AFO are made up of polymer arrangements with porosity. The reasoning behind this decision is that the material characteristics obtained from the tensile tests are sufficient to represent this behaviour. The same approach was also used in Krone & Schuster (2006) research where they modelled bone structures which in nature are not only porous but are also irregular in shape (in contrast with the consistent raster shape of FDM printed components).

Table 3.6 AFO Mesh Parameters

Parameters	Values
Element Type	Solid
Element Shape	Parabolic Tetrahedron
Element Size	9.1067 mm
Element Tolerance	0.0003032135 mm
Element Order	Parabolic
Refinement Ratio	0.9
Minimum Triangle Angle	20
Maximum Triangle Angle	30
Maximum Element Growth Rate	1.2

The resulting meshed geometry is as shown in Figure 3.16. As can be observed, the distribution of meshes are consistent with less congestion of mesh in any of the AFO regions.

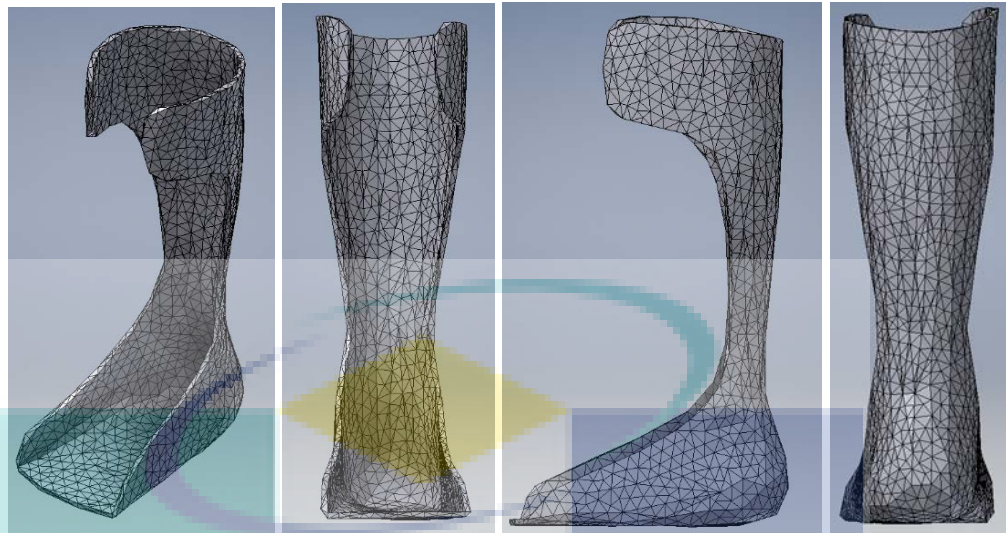


Figure 3.16 Meshed AFO Geometry (From Left; Isometric, Side, Front and Back View Respectively).

### 3.4.2 Material Properties

The material in this FEA study is modelled as an anisotropic material which is defined by the material matrix as described in Equation 3.1. As the FEA study is mainly on structural static analysis, thermal factors such as anisotropic thermal expansion, coefficient as well as conductivities are disregarded.

$$\begin{Bmatrix} \sigma_x \\ \sigma_y \\ \sigma_z \\ \tau_{xy} \\ \tau_{yz} \\ \tau_{zx} \end{Bmatrix} = \begin{bmatrix} G_{11} & G_{12} & G_{13} & G_{14} & G_{15} & G_{16} \\ & G_{22} & G_{23} & G_{24} & G_{25} & G_{26} \\ & & G_{33} & G_{34} & G_{35} & G_{36} \\ & & & G_{44} & G_{45} & G_{46} \\ \text{Symmetric} & & & & G_{55} & G_{56} \\ & & & & & G_{66} \end{bmatrix} \begin{Bmatrix} \epsilon_x \\ \epsilon_y \\ \epsilon_z \\ \gamma_{xy} \\ \gamma_{yz} \\ \gamma_{zx} \end{Bmatrix} = \begin{bmatrix} A_1 \\ A_2 \\ A_3 \\ A_4 \\ A_5 \\ A_6 \end{bmatrix} (T - T_{REF}) \quad 3.1$$

The input to this material matrix are obtained from the tensile test results mentioned beforehand. As there are many possible resulting material properties due to large possible combination of printing parameters, a selection process will be conducted before finalising this value. The detailed process of this selection is as discussed in Chapter 4.2 in this thesis. In terms of how the anisotropy axis is aligned relative to the orthosis, the coordinate system used are as illustrated in Figure 3.8.



### 3.4.3 Boundary Conditions – Loads and Constraints

AFO during walking is subjected to loadings that are highly complex due to interaction between the limb and the AFO itself. These loads vary with respect to position and time in a cyclic manner, so a dynamic analysis is necessary to fully describe the loading conditions borne by the AFO. In this research, the AFO is modelled in isolation and loads are applied to it directly as the main objective of the simulation is to produce an AFO with structural integrity. The loads are exaggerated to ensure that the aforementioned objective is achieved. While modelling the forces borne by the AFO, the following assumptions and simplifications were made:

1. Loading conditions are assumed to vary slowly with respect to time, so that inertia and damping effects are not induced and can be disregarded.
2. Loading types are limited to externally applied forces and pressures, steady-state inertia loads such as gravity.
3. The foot is rigidly attached to the Orthosis with no change of contact conditions
4. The mass of the individual foot regions is calculated using percentage total body weight based on work done by Plagenhoef et. al, (1986).
5. Internal tissue friction of the foot and its effects are omitted from the model.
6. All loadings are assumed to be borne by a single leg (single stance) at all major stages to induce maximum-worst case loading conditions.
7. The foot modelled as a solid, non-deforming object which applies all the force directly to the orthosis.

In this research, a healthy 27 years old individual with 84 kg weight and 1.74 m height is used as a test subject for both the scanning process to obtain the geometry as well as the reference for this AFO FEA. This subject is also appropriate for Plagenhoef et al's (1983) body segment weight data as the values fall within its range of application.

Table 3.7 Body Mean Segment Weight (Based on Percentage Value, Adapted from (Plagenhoef et al., 1983) for Lower Limb Segments)

Segment	Males	Female	Average
Total Leg	16.68	18.43	17.555
Thigh	10.5	11.75	11.125
Leg	4.75	5.35	5.05
Foot	1.43	1.33	1.38
Leg & Foot	6.18	6.68	6.43

When a person walks while wearing an AFO, a number of cyclic events occur. These series of events can be generally divided into three main phases; heel strike, mid stance and the push off stage in sequence, respectively. In this research, 3 different static analysis are performed, one for each gait phase.

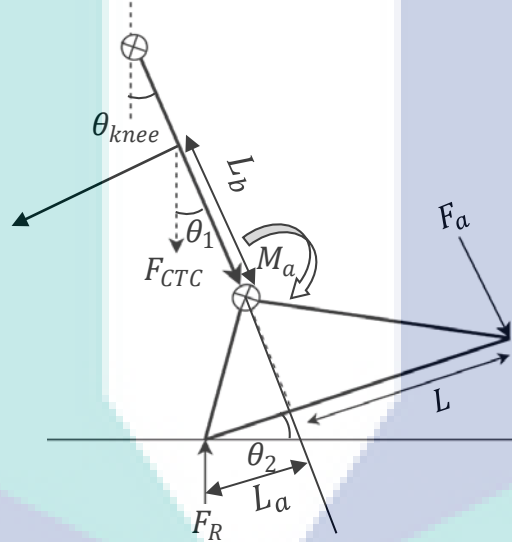


Figure 3.17: Free-Body Diagram for The Heel Strike Gait Phase

In the heel strike phase as illustrated in Figure 3.17, the magnitude of individual forces can be obtained by summing all the moment at point a which is the ankle joint, given by  $M_a$  as described in Equation 3.2. The whole weight of the body,  $F_{BW}$  is transmitted from the body to the ground causing a resultant force,  $F_R$  to act upon the heels given by the rearranged Equation 3.3. The moment arm,  $L$  is the perpendicular length of the orthosis bottom wedge from the ankle joint where  $\theta_2$ , is the dorsiflexion angle obtained from gait data.

$$M_a = mgL \sin \theta_1 - F_a L - F_r L_a = 0 \quad 3.2$$

$$F_a = \frac{mgL \sin \theta_1 - F_r L_a - mgL_b \cos \theta_2}{L} \quad 3.3$$

$$F_{CTC} = m_{leg} \sin \theta_1 ; \text{ where } \theta_1 = \theta_{knee} \quad 3.4$$

The contact force is caused by the shank mass being supported by the orthosis and is represented by Equation 3.4. The contact angle,  $\theta_1$  is equal to the knee angle,  $\theta_{knee}$ .  $\theta_{knee}$  which gives the highest contact force value ( $\theta_{knee} = 89^\circ$ ) is selected from gait data from Park et al. (2009).

In the mid stance phase, the whole-body weight is applied onto the foot and a pressure profile is developed as shown in Figure 3.18. To properly model this gait phase for FEA, foot pressure profiles during one-foot standing is applied to the AFO geometry based on the values obtained from Park et al. (2009) extrapolated to the aforementioned subject's weight. These extrapolated foot pressure values are as described in Table 3.8.

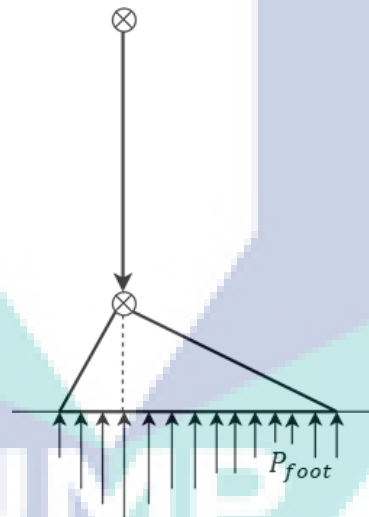


Figure 3.18 Free-Body Diagram for the Mid Stance Gait Phase

A push off force is applied to the hind regions of the foot caused by propulsion moment produced by the ankle joint as described in Figure 3.19. The moment arm is the length from the ankle joint to the end of the heel as per term  $L_{hind}$  in Equation 3.5. The only region of the AFO in contact with the ground is the forefoot region, therefore a resultant force with the same magnitude as the total body weight is applied at that point as per Equation 3.6.

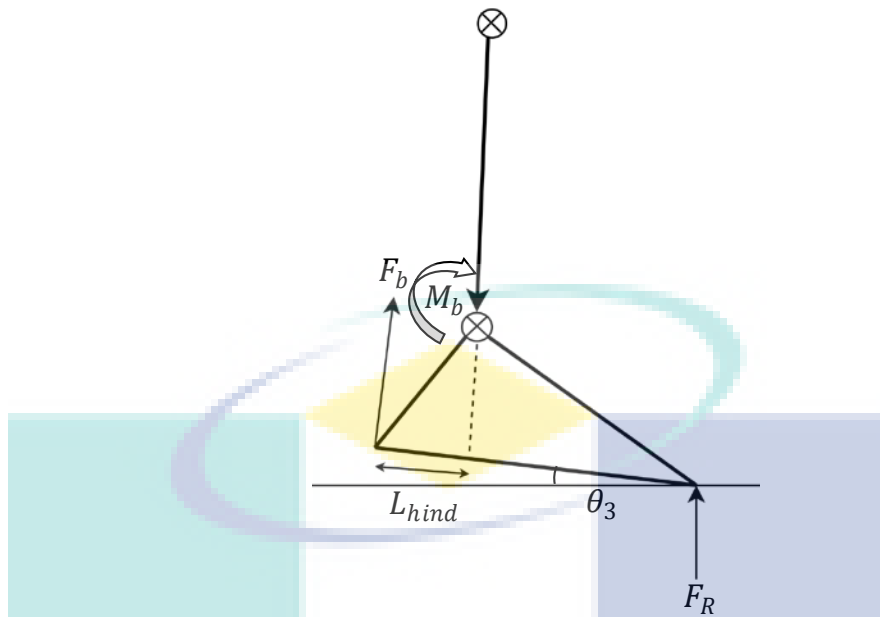


Figure 3.19 Free-Body Diagram for the Push Off Gait Phase

$$F_b = \frac{M_b}{L_{hind}} \quad 3.5$$

$$F_R = F_{BW} \quad 3.6$$

The forces applied on this FE model are based of the previous developed static equations. The region as well as the size in which these forces are applied are obtained based on the foot features from the 3D foot scan. The features are obtained by tracing the feature outline from the 3D scan as shown in Figure 3.20. The coordinates of the features are obtained and is used as reference for applying boundary conditions in the FE model.



Figure 3.20 Obtaining Foot Feature Coordinates from 3D Foot Scan

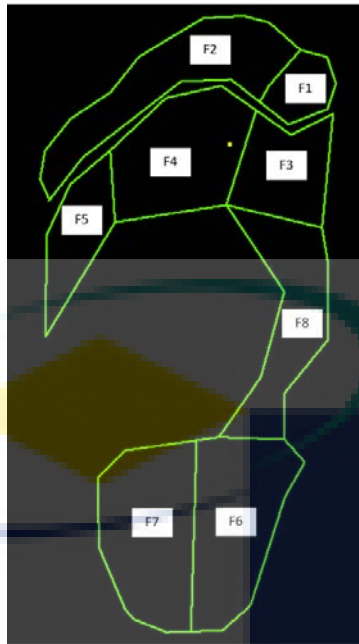


Figure 3.21 Traced Geometry of Scanned Foot. The Yellow Dot Represents the Origin of the Coordinates.

The geometry in Figure 3.21 is used as the regions of force application in the FEA software representing the contact between the AFO and the foot during the gait phase. The regions are separated into 8; each with varying magnitude of forces. The foot pressure data for Figure 3.21 is adapted from Park et al.'s (2009) research due to the similarity in both the anthropometry, age and weight of the test subject used. Park et al.'s (2009) employed the F-scan foot pressure sensing system to obtain the foot pressure profile of 4 normal subjects. The subject chosen is referenced as “test subject 3 – left foot” in Park et al. (2009) study and is a normal, healthy 25 years old individual weighing 84 kg with a height of 174 cm. The foot pressure region and its respective magnitude is as described in Table 3.8.

Table 3.8 Foot Pressure Profile Adapted from. Park et al.'s (2009)

Region	Pressure Magnitude
F1	58.27 kPa
F2	46.65 kPa
F3	105.74 kPa
F4	310.67 kPa
F5	158.50 kPa
F6	174.28 kPa
F7	175.02 kPa
F8	146.48 kPa

The pressure and its respective region are applied to the FE model as per Figure 3.22. Each coloured arrow represents different pressure regions and values ranging from F1 to F8.

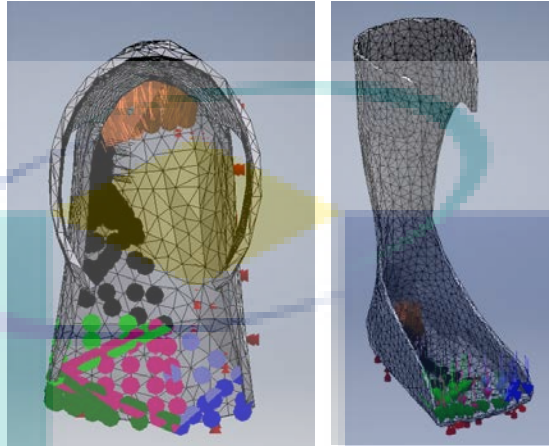


Figure 3.22 Foot Pressure Boundary Condition Applied on Midstance Gait Phase FE Model (Left – Top View, Right- Isometric View)

The fixed constraint is a constraint that freezes both translational and rotation motion in all the axes at the region that they are defined at ( $T_x, T_y, T_z = 0$ ). This constraint is applied at different regions according to the gait phase. In the midstance gait phase, the fixed constraint is assigned at the AFO ground contact surface as shown in marked by the red arrows.

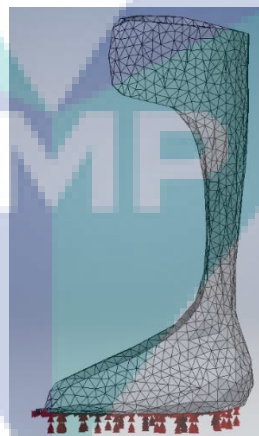


Figure 3.23 Location of Fixed Constraint in the AFO Model for the Midstance Gait Phase.

In the heel strike phase, the region of contact involves the foot as well as the shank. The shank contact area is obtained via similar methods as the one used for the foot profile in Figure 3.21.

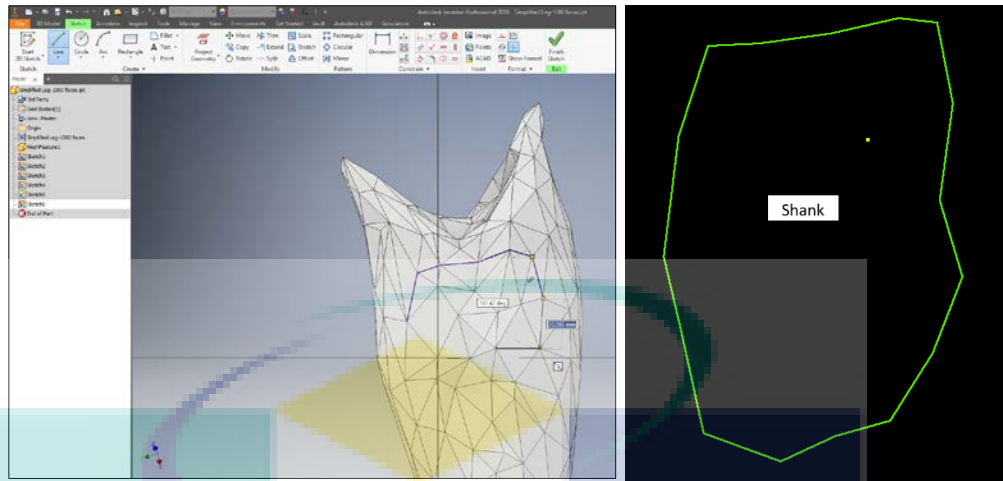


Figure 3.24 Obtained Shank Profile (Left-Feature Tracing, Right-Resultant Geometry)

The foot contact region in the midstance phase is reused in this phase albeit with different values. The forces and their respective regions of application are as Figure 3.23 which is based on the contact regions as exhibited in Figure 3.22.

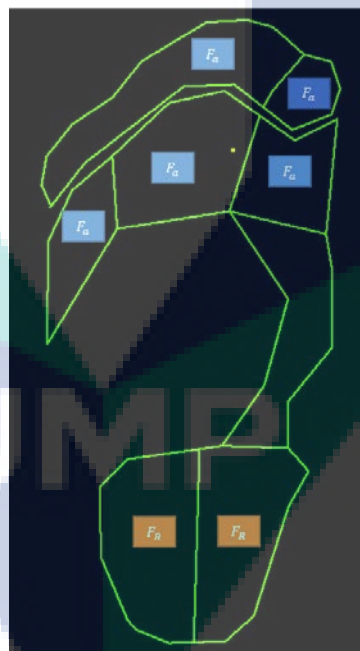


Figure 3.25 Location of Force FE Model Definition during Heel Strike Gait Phase

Table 3.9 describes the maximum values for the aforementioned regions. In the FEA simulation, the Shank Contact Force and the Ankle Propulsion Force are obtained by inputting angle value of shank contact angle (to a maximum of  $61^\circ$ ) and the ankle angle (maximum  $27^\circ$ ) to Equation 3.3 and Equation 3.4. The maximum angle values for both the shank contact and ankle angle are both obtained from Park et al.'s (2009) human

gait analysis data captured using Inertial Measurement Unit (IMU) sensors. The resultant force however is applied as a step function due to its constant value throughout this gait phase.

Table 3.9 Force Boundary Condition for Mid-stance Phase

Region	Maximum Magnitude (N)
Shank Contact Force, $F_{CRC}$	18.98 N
Body Resultant Force, $F_R$	824.04 N
Ankle Propulsion Force, $F_a$	51.59

In the heel strike phase, the heel region is assigned the fixed constraint due to it being the foot pivot region during this gait phase. The loadings are applied as in Figure 3.26 to the FE Model with the red arrows being fixed constraint and the green, blue, yellow arrows being the shank contact force, ankle propulsion force and body resultant force respectively.

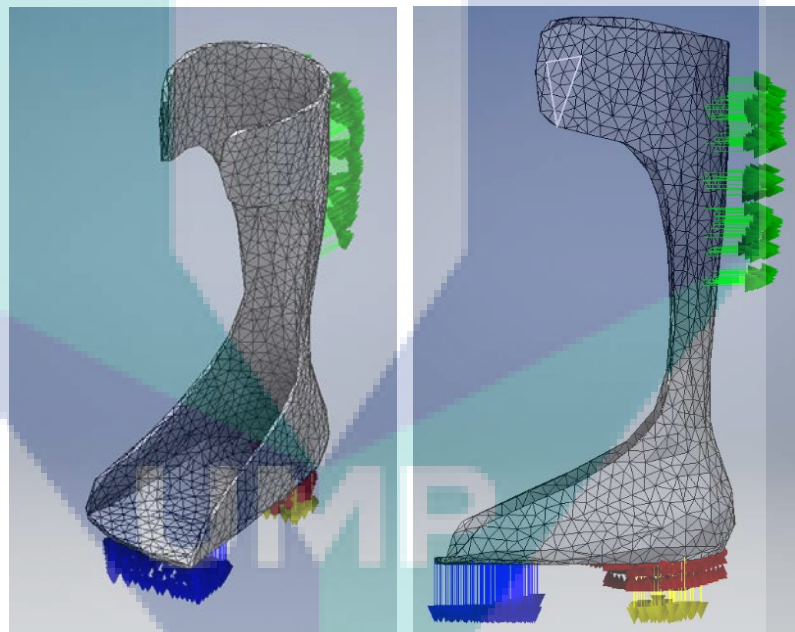


Figure 3.26 Loadings and Constraints Applied to Heel Strike Phase AFO FE Model (Left - Fixed Constraint , Right – Loads).

The Push Off stage involves the propulsion force of the ankle while the foot pivots on the forefoot. Similar to the previous gait phase, the contact region is reused but with different force values and region definition.



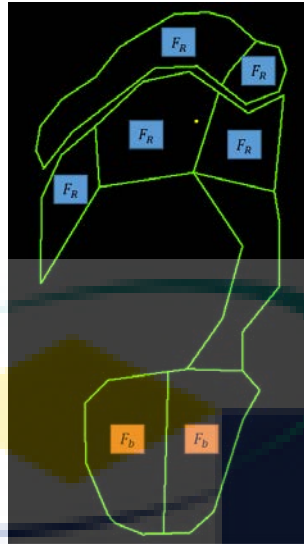


Figure 3.27 Location of Force FE Model Definition during Push Off Gait Phase

Table 3.10 shows the maximum values for the previously defined foot regions. As per previously discussed, the body resultant force is applied as a step function while the Ankle Push Off force is applied as a linear function up to a value of dorsiflexion angle of  $6^\circ$ . The dorsiflexion angle is also obtained from Park et al.'s (2009) gait analysis data.

Table 3.10 Force Boundary Condition for Mid-stance Phase

Region	Maximum Magnitude (N)
Body Resultant Force, $F_R$	824.04 N
Ankle Push Off Force, $F_b$	20.75 N

Based on Table 3.10, the loadings are applied to the FE Model as per Figure 3.28. The red arrows represent the fixed constraint while the orange and green arrows represent the body resultant force as well as the ankle push off force respectively.

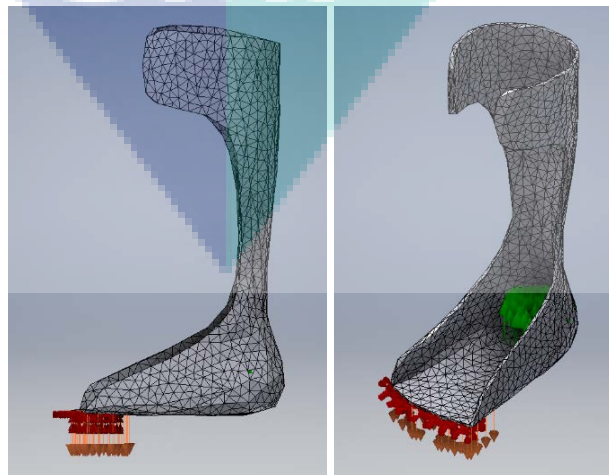


Figure 3.28 Push off Gait Phase FE Model Boundary Conditions

### 3.5 Topology Optimisation

Due to the high loads and relatively low structural integrity of the AFO geometry under heel strike load cases, this phase is selected to be optimised. The main objective of the topology optimisation process is the reduction of mass under the constraint of stress (maximum stress in geometry must not exceed material yield stress). The efficacy of the topology optimisation process is highly mesh dependent therefore a high mesh count is used in this study. Material properties implemented are similar to the FEA model in the previous subchapter. Table 3.11 summarises the optimisation configuration parameters while lists the mesh configuration implemented.

Table 3.11 Topology Optimization Configuration

TO Parameter	Value
Objective Function	Minimize Weight (Target: 30% Reduction)
Constraint	$\sigma_{MAX} < \sigma_{YIELD}$
Load Case	Heel Strike

Table 3.12 Mesh Configuration for Topology Optimisation Process

Mesh Parameter	Value
Shape	Tetrahedral
Element Size	1.75 mm
Element Order	Parabolic
Minimum Triangle Angle	20
Maximum Triangle Angle	60
Max Element Growth Rate	1.5
Material Idealisation	Solid, Orthotropic

The optimisation algorithm in Inventor Nastran analyses load penetration path. Under the specified load constrains and mesh, the algorithm iterates through each element to investigate which elements that are not affected by loads by a certain range and remove them. Due to the nature of the algorithm, regions critical for the function of the AFO are preserved, meaning to exclude certain regions from optimisation process. The configured preserved regions are as shown in Figure 3.29 as green markings. The yellow arrows in Figure 3.29 indicate load applications and their directions which is set as per the heel strike FEA load case.

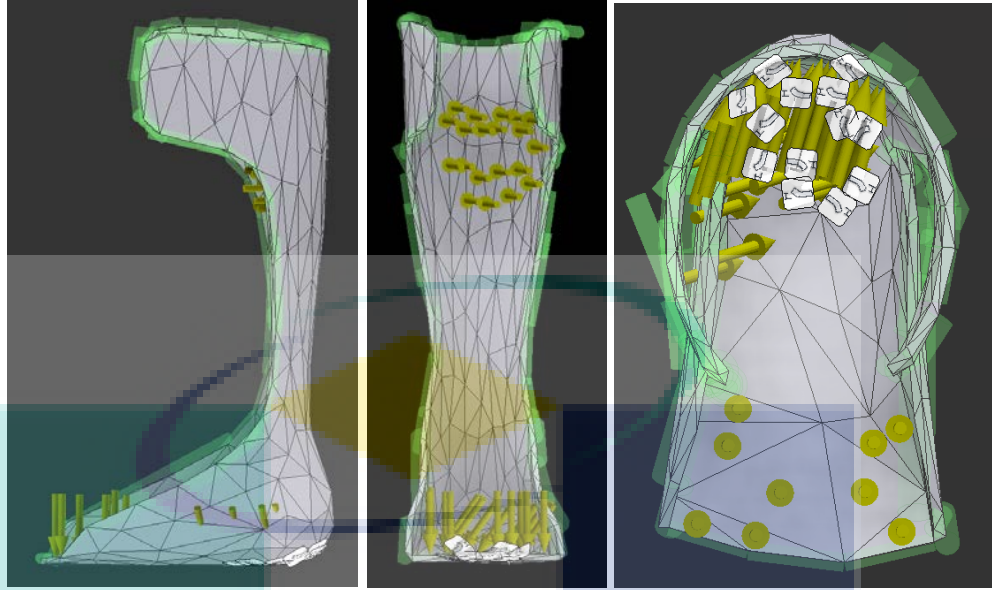


Figure 3.29 Boundary Condition for AFO Topology Optimisation

### 3.6 Cost Model for Fabrication of AFO using the FDM Process

To accurately quantify the cost savings from performing design optimization, a detailed cost analysis must be performed covering every aspect of the process; from the design phase, up to the fabrication phase. Henrique et al. (2010) in their work, have presented the cost calculation specific to their FDM Machine based on Xu, Wong, & Loh (2000)'s cost model for the Rapid Prototyping (RP) process. Henrique et al. (2010)'s work has been adapted to suite the FDM machine and processes as used in this research. The authors in the said work stated that the total prototype cost ( $C_{fp}$ ), is an sum of 4 cost components which is the processing cost ( $C_p$ ), execution cost ( $C_e$ ), material cost ( $C_m$ ) and the post-processing cost ( $C_{pp}$ ) as described in equation 3.7.

$$C_{fp} = C_p + C_e + C_m + C_{pp} \quad 3.7$$

Henrique et al. (2010) cost calculation for the processing cost; i.e. the cost for the prototype design is as shown in equation 3.8.

$$C_p = \left( \frac{0.2 \times C_{pc}}{W_{at}} + \omega_d + PC_e \times P_{kh} + \frac{0.2 \times C_{sl}}{W_{at}} \right) \times T_p \quad 3.8$$

Where:

$C_{pc}$  - Personal Computer (PC) Cost (RM)

$C_{sl}$  - Software license cost (RM)

$\omega_d$  - Designer's cost per hour (RM/h)

$W_{at}$  - PC availability time per year (h)

$PC_e$  - PC energy consumption hour rate (kWh/h)

$P_{kh}$  - Local average energy specific cost (RM/kWh)

$T_p$  - Designer's processing time (h)

Xu, Wong, & Loh (2000) suggested a model as shown in equation 3.9 and a machine cost index  $r_f$  as described in equation 3.10 that covers all machine running costs in the function of time including taxation percentage from machine running and labour costs.

$$C_e = T_e \cdot r_f \quad 3.9$$

$$r_f = (1 + \sigma_{op}) \cdot \omega_o + (1 + \sigma_{mch}) \cdot \frac{P_{mch}}{8760 \cdot T_{mch}} \quad 3.10$$

This model however, did not specify the physical components of machine run cost (energy consumption, running cost, labour cost). Martins (2003) proposed a new model that included the physical components as described in the modified cost index equation 3.11. This equation is similar to our operating conditions and is used instead of 3.10.

$$r_f' = \left( (P_e \times P_{kh}) + \frac{0.2 \times P_{mp}}{W_{at}} + \omega_o + \left( \frac{M_m}{W_{at}} \right) \times 12 \right) \quad 3.11$$

Where:

$r_f'$  - Machine running cost per hour

$\omega_0$  - Operator's cost per hour (RM/h)

$P_e$  - Machine energy consumption rate per hour (kWh/h)

$P_{kh}$  - Local average energy specific cost (RM/kWh)

$M_m$  - Maintenance cost per month (RM)

$P_{mp}$  - Machine price (RM)

$W_{at}$  - Machine availability time per year (h) – (8h/day, 22 days/month, 12 months/year)

Martins (2003) proposed a material cost calculation as shown in equation 3.12, taking into consideration the material, support and construction cost as a function of cost per unit volume.

$$C_m = \frac{(V_m \cdot P_m)}{V_c} + \frac{(V_s \cdot P_s)}{V_c} \quad 3.12$$

Where:

$V_m$  - Model volume utilized (cm<sup>3</sup>)

$P_m$  - Specific cost per model material volume (RM)

$V_s$  - Support volume utilized (cm<sup>3</sup>)

$V_c$  - Model/support material volume per cartridge (cm<sup>3</sup>)

$P_s$  - Specific cost per support material volume (RM)

The Zortrax M200 FDM machine used in this study does not have a separate material used as support. The printed support structure uses the same material as the main printing material albeit with lesser density than model parts for easier removal. This simplifies the model to equation 3.13 for our case. Units are also altered since the supplied material by the manufacturer uses per unit weight for cost calculation.

$$C_m = \frac{(V_{util} \cdot P_{mat})}{V_{total}} \quad 3.13$$

Where:

$V_{util}$  - Total material utilized (g)

$P_{mat}$  - Specific material cost per spool (RM)

$V_{total}$  - Total weight per spool (g)

Henrique et al. (2010) modified Martins (2003)'s machine running cost model by modifying it to suit the ultrasonic stirrer device. The resultant model is as shown in equation 3.14. The model includes the total running cost of the ultrasonic device as well as the soap material's cost. This device is used to remove support material from the 3D Printed components.

$$C_{pp} = \left( (P_{ub} \times P_{kh}) + \frac{0.2 \times P_{bp}}{W_{at}} + \omega_0 \right) \times T_{pm} + (S_c \cdot S_r) \quad 3.14$$

Where:

$P_{ub}$  - Energy consumption rate per hour of the ultrasonic bowl (kWh/h)

$P_{kh}$  - Average local energy specific cost (RM/kWh)

$\omega_0$  - Operator's cost per hour with fringe benefits (RM/h)

$P_{bp}$  - Bowl price (RM)

$W_{at}$  - Bowl availability time per year (h)

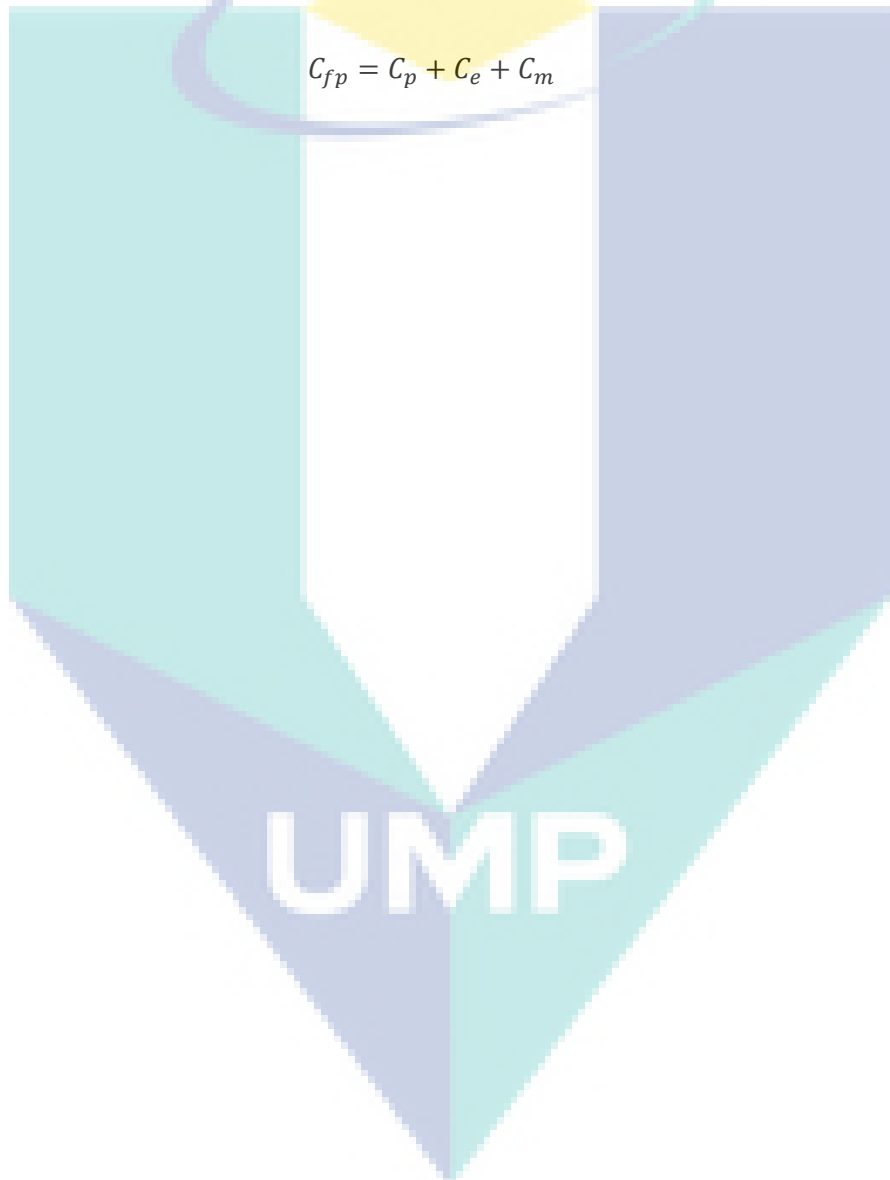
$T_{pm}$  - Model permanence time inside the ultrasonic bowl (h)

$S_c$  - Soap cost per washing time at post-processing (RM)

$S_r$  - Soap rate per package (percent)

In this research, the post-processing stage only involves the removal of support material using manual tools such as scrapers and pliers done by an operator therefore Equation 3.14 is disregarded.

In summary, the prototype cost model used is as described below in equation. The cost component implemented is processing cost, execution cost and material cost as per equation 3.8, 3.9 (with 3.11 machine cost factor), and 3.13 respectively. The values used in the cost calculation are as listed in Table 4.16.

$$C_{fp} = C_p + C_e + C_m \quad 3.15$$


## CHAPTER 4

### RESULTS AND DISCUSSION

#### 4.1 Scanned Limb 3D Geometry and Initial AFO Design

The results of the measurements are as shown in Table 4.1. Previous study such as Matthew, Mary-Ellen, & Keith's (2011) study on Virtual Orthotics 3D non-contact digital scanner device gives a smallest real difference (SRD) value of between 1.56 mm to 5.27 mm. This proves that anthropometric measurements using Kinect are acceptable as the real measurement deviation of the Kinect device ranges from 1.3 mm to 5.1 mm. These measurements are also verified by comparing with measurements performed by a similar low-cost foot 3D scanner which reports a 3-5% difference with actual measurements (Taha et al., 2013). Table 4.1 summarises the measurement accuracy scanned geometry using Microsoft Kinect and the Skanect software.

Table 4.1 Comparison of Measurements Between Scanned and Actual Limb

<b>Anthropometric Features</b>	<b>Actual Limb Measurement (mm)</b>	<b>Scanned Limb Measurement (mm)</b>	<b>Measurement Deviation (mm)</b>	<b>Percentage Measurement Error</b>
Heel-Toe Length (A)	121.5 mm	125.8 mm	+ 4.3 mm	+ 3.54 %
Toe (B)	33.9 mm	35.2 mm	+ 1.3 mm	+ 3.83 %
Ankle (C)	77.2 mm	79.1 mm	+ 1.9 mm	+ 2.46 %
Calf (D)	112.6 mm	117.3 mm	+ 4.7 mm	+ 4.17 %
Proximal (E)	198.1 mm	203.2 mm	+ 5.1 mm	+ 2.57 %

In order to design the customised AFO, a conforming 3D shell element must be designed based on the scanned limb 3D model. This is done by drawing a set of physical trim lines in the sagittal plane that will be used to remove specific regions of the scanned limb 3D model. These trim lines, as described in Figure 4.1 are determined based on M.



A. Arnold's (1999) Ankle Foot Orthosis trim line construction which consisted of the height of the proximal trim line (marked as PROXIMAL in Figure 4.1), the location of the calf band trim line (CALFBAND and OVERLAP respectively), radius of the ankle and calf trim line arcs (RADIUS) and the ankle joint vertical clearance (ANKLE).

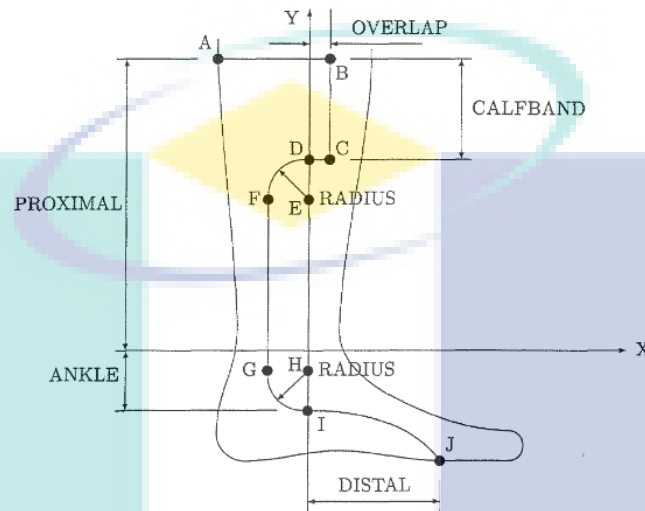


Figure 4.1 Dimensions for Construction of Trim line (M. A Arnold, 1999)

In this study, the length of these physical dimensions is determined manually based on how well they enclose the scanned individual's foot. The dimensions of the trim line used are described in Table 4.2.

Table 4.2 Dimensions for Trimline

Orthosis Measurement	Values (mm)
Proximal	228
Distal	98
Calf band	26
Overlap	73
Radius	18
Ankle	22

In the Inventor CAD Software environment, this trim line is drawn on a drawing plane projected from the sagittal plane. This trim line is then projected (as shown as in Figure 4.2 as the white solid) across the scanned foot geometry.

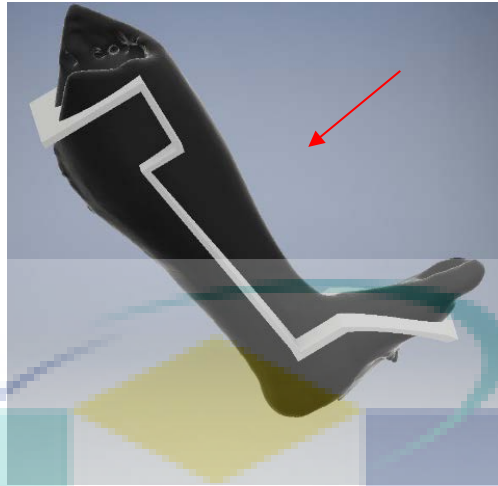


Figure 4.2 AFO Design Process - Splitting of the Geometries

This projected geometry is used as a parting line using the split command in which the geometry marked by the arrow will be removed from the scanned foot geometry. After this process is performed, the remainder geometry is extruded to produce a shell element with a thickness of 6 mm using Inventor's face extrude command. This shell component is further refined by adding fillet and radii to smoothen out the sharp edges. The end result is the initial prototype of the AFO as shown in Figure 4.3. Precise dimension of the orthosis is included at APPENDIX B section of the thesis.



Figure 4.3 Initial Prototype of Ankle Foot Orthosis Designed Based on Scanned Geometry.

## 4.2 Tensile Test Results of FDM Printed Specimens for Different Printing Parameters

This section presents the tensile test results performed on FDM printed specimens for different process parameters; namely the layer thickness and infill densities. For each of these process parameters, their effects towards the mechanical properties of different build orientations (A, B and C respectively) were also investigated. The results in this section are organised into build orientations and is divided into two sections; one for layer thickness settings and the other for infill density settings. All results presented in this section are engineering stress-strain curves.

### 4.2.1 Tensile Test Results for Specimens of Different Layer Thickness

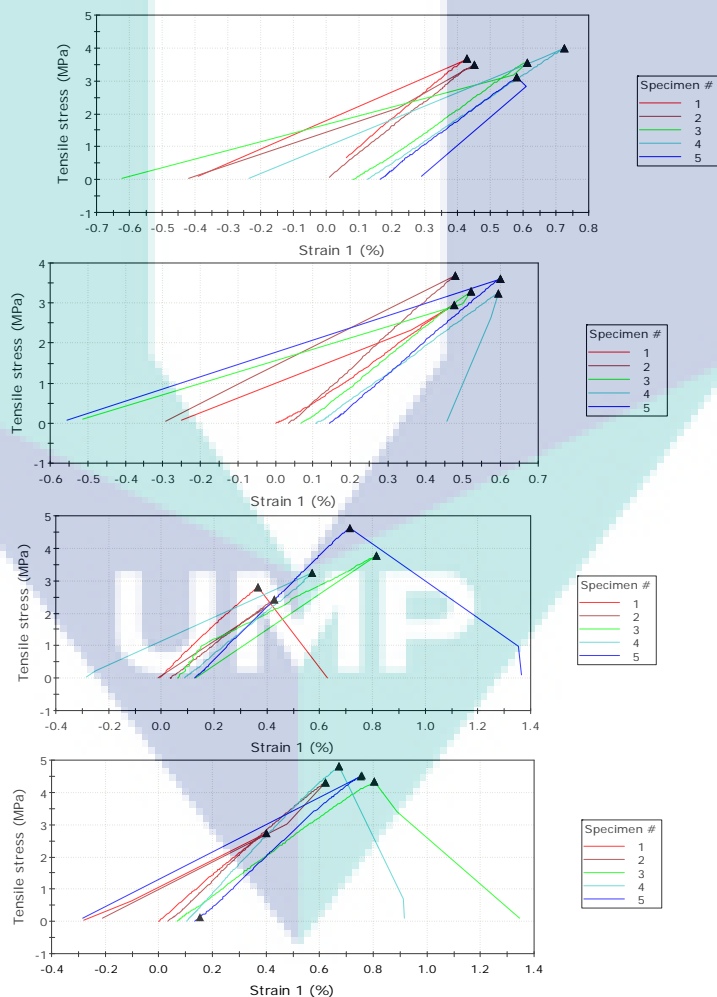


Figure 4.4 A Build Orientation Specimen Stress-Strain Curves for Layer Thickness of 0.09mm, 0.14mm, 0.19mm and 0.29mm (From top to bottom respectively)

Tested specimens within similar build orientation settings exhibits a similar stress strain curve shape. The A-build orientation stress strain curves as shown in Figure 4.4, exhibits a linear strain curve with the specimen fracturing within the linear proportional line similar to that of those of rigid materials. This linear stress strain curve shape also holds true for the other A-build orientation which will be discussed at the following subchapter.

Table 4.3 A-Build Orientation, Low Density Z-ABS Material Properties for Different Layer Thickness (N = 5 Samples for Each Layer Thickness). Values of Properties are of Average Value for 5 Samples.

<b>Layer Thickness</b>	<b>0.09 mm</b>	<b>0.14 mm</b>	<b>0.19 mm</b>	<b>0.29 mm</b>
Maximum Load	325.05 N	305.26 N	306.35 N	376.68 N
Tensile Stress at Maximum Load	3.57 MPa	3.35 MPa	3.37 MPa	4.14 MPa
Tensile Strain at Maximum Load	3.57	3.35	3.37	4.14
Modulus of Elasticity	439.93 MPa	421.84 MPa	727.31 MPa	540.46 MPa
Load at Break	325.05 N	305.26 N	306.35 N	376.38 N
Tensile Stress at Break	3.57 MPa	3.35 MPa	3.37 MPa	4.14 MPa
Tensile Strain at Break	-1.22	1.09	1.32	1.37
Tensile Stress at Yield-Zero Slope	3.57 MPa	3.38 MPa	3.27 MPa	3.39 MPa
Maximum Load Standard Deviation	29.52 N	26.49 N	78.68 N	72.95 N
Tensile Stress Standard Deviation	0.32 MPa	0.29 MPa	0.87 MPa	0.80 MPa

In comparison with the other build orientations, A-Orientation exhibits the smallest average maximum stress across process parameters; 3.57 MPa for filament thickness of 0.09 mm, 3.35 MPa for 0.14 mm, 3.37 MPa for 0.19 mm and 4.14 MPa for 0.29 mm filament thickness respectively. The average maximum strength of components built in this orientation shows no significant increase as filament thickness is increased and this can be attributed to the weak bonding between filaments.

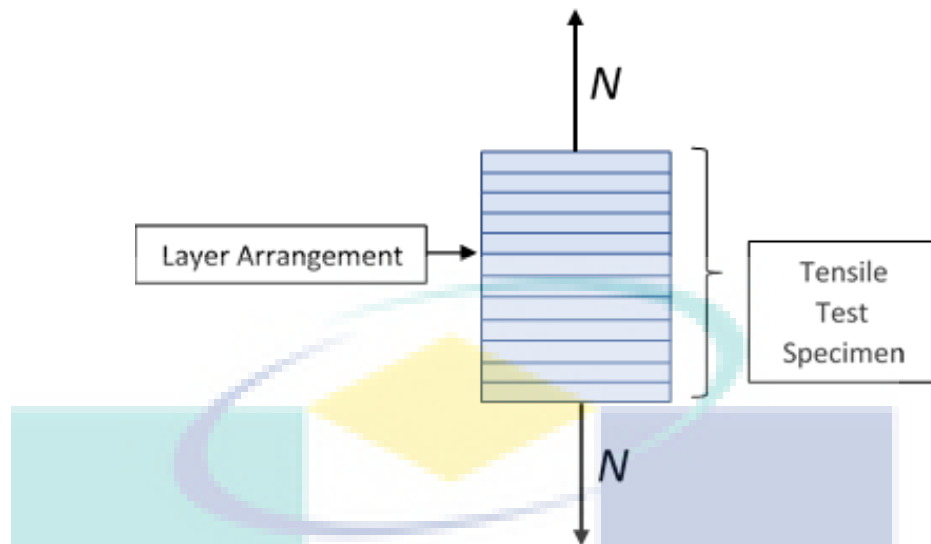


Figure 4.5 Direction of Forces,  $N$  to A-Build Orientation Filament Arrangement

This is due the specimen print layers experiencing a perpendicular force direction resulting from the arrangement of the filament layers as exhibited in Figure 4.5. In this orientation, the load is not supported by the whole filament but by the small area of bonding in between filaments instead. Due to the dependence on the bonding conditions of the filaments, fractures in this orientation occurs suddenly and rapidly without any dip or plateauing of the stress-strain curve slope. This is indicated in Table 4.3 where the average stress at maximum load and break are of the same value, indicating that the specimen fractures at the instant of achieving its maximum load. The stability of the mechanical properties throughout increasing filament thickness parameters also gets more unstable shown by the increasing standard deviation (SD) values. High SD value means a large variance in recorded value between samples which could be potentially unwanted for applications requiring small stress tolerances.

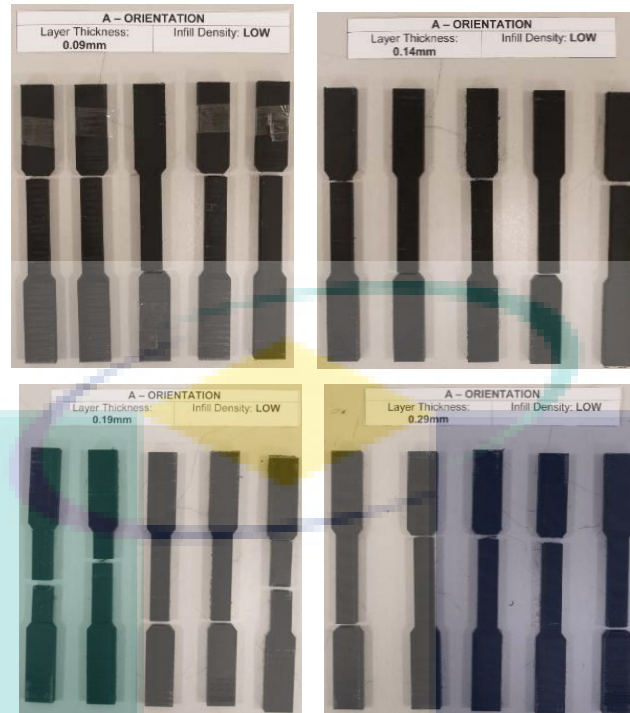


Figure 4.6 Failure Mode of A-Build Orientation for Each Layer Thickness

The locations of the fractures are shown in Figure 4.6. The specimens built in this orientation underwent fractures which are straight and clean at the plane perpendicular to the loading direction. No plastic deformation stretch mark patterns were observed at the region of the fracture.

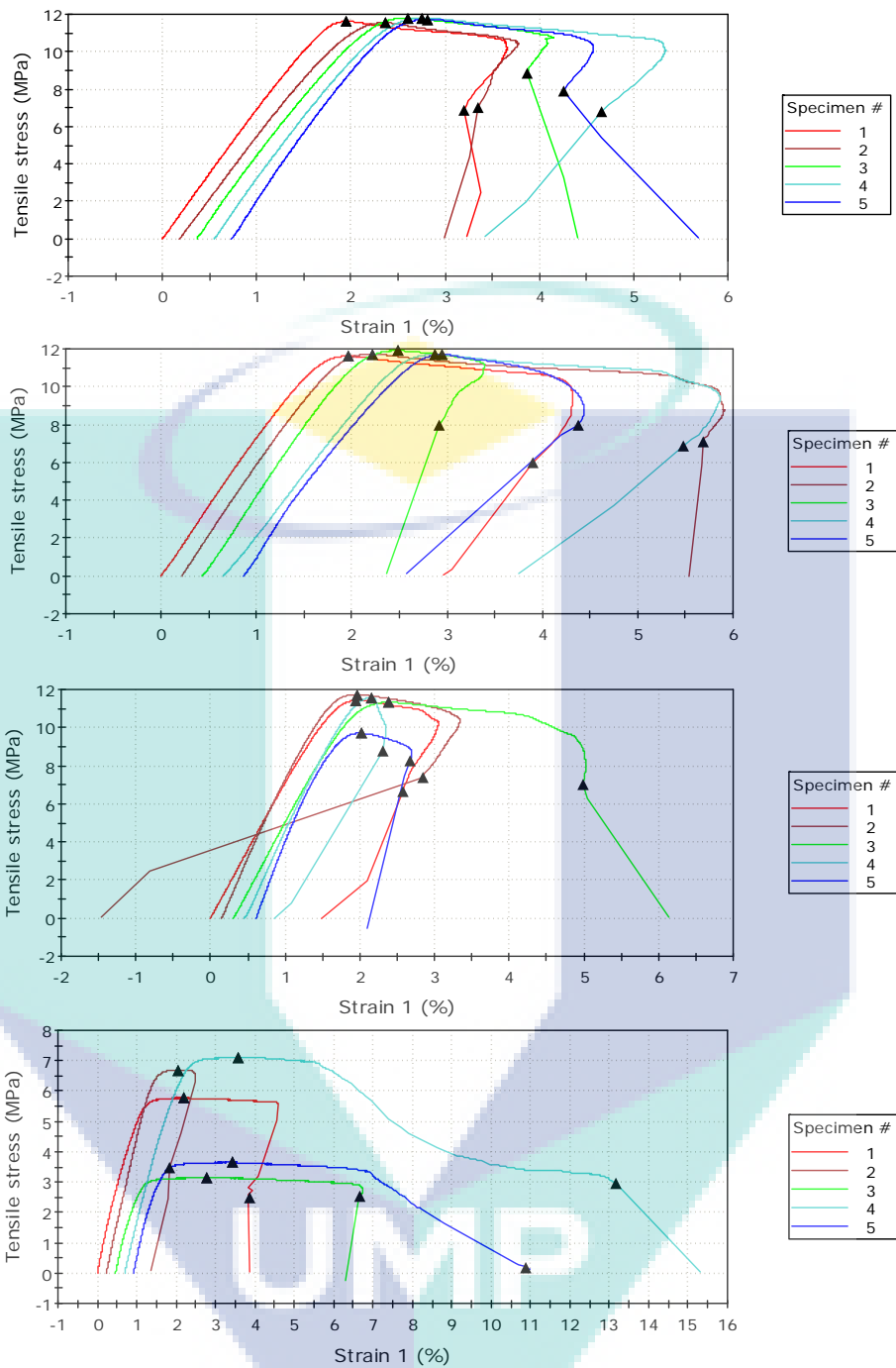


Figure 4.7 B Build Orientation Specimen Stress-Strain Curves for Layer Thickness of 0.09mm, 0.14mm, 0.19mm and 0.29mm (From top to bottom respectively)

B-Orientation specimens exhibits a ductile material stress-strain curve that undergoes a significant amount of deformation before fracturing. However, in actuality the material is not ductile and the plateau of deformation before fracturing is actually due to the breakage of individual filaments until the fracture propagation is complete. The material properties of these specimens are stable at lower layer thickness (0.09 mm and

0.14 mm) in which the tested specimen have very little variation of maximum in between samples but becomes increasingly unstable when higher filament thickness values are used.

Table 4.4 B-Build Orientation, Low Density Z-ABS Material Properties for Different Layer Thickness (N = 5 Samples for Each Layer Thickness). Values of Properties are of Average Value for 5 Samples.

Layer Thickness	0.09 mm	0.14 mm	0.19 mm	0.29 mm
Maximum Load	1065.01 N	1067.79 N	1015.35 N	479.57 N
Tensile Stress at Maximum Load	11.70 MPa	11.73 MPa	11.16 MPa	5.27 MPa
Tensile Strain at Maximum Load	5.09	4.40	3.87	5.68
Modulus of Elasticity	667.29 MPa	689.11 MPa	787.75 MPa	503.07 MPa
Load at Break	680.27 N	652.63 N	693.40 N	211.03 N
Tensile Stress at Break	7.48 MPa	7.17 MPa	7.62 MPa	2.32 MPa
Tensile Strain at Break	8.92	8.52	6.24	10.32
Tensile Stress at Yield-Zero Slope	11.70 MPa	11.73 MPa	11.16 MPa	5.27 MPa
Maximum Load Standard Deviation	10.23 N	9.57 N	75.12 N	162.68 N
Tensile Stress Standard Deviation	0.11 MPa	0.11 MPa	0.83 MPa	1.79 MPa

Lower layer thickness settings also result in stronger specimens in which the average maximum tensile stress at maximum load is 11.70 MPa and 11.73 MPa for 0.09 mm and 0.14 mm layer thickness respectively, as shown in Table 4.4. This value dips slightly to 11.16 MPa at 0.19 mm layer. Strain differences between specimens also tend to be larger at this point. At a layer thickness of 0.29 mm, the specimens tested starts to be unstable, displaying large differences in maximum stress and maximum strain in between specimens. The average tensile stress at maximum load also drops drastically at 0.29 mm dropping to a low 5.27 MPa. In terms of mechanical property stability, the values are stable only in the lower filament thickness range (0.09 mm and 0.14 mm filament thickness setting) which is similar to A-Orientation. When 0.29 mm filament thickness is used, the material property becomes highly unstable exhibiting a large SD value of 162.68 N as shown in Table 4.4.



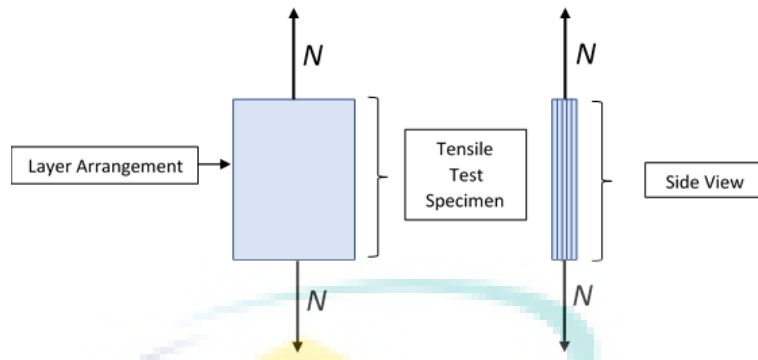


Figure 4.8 Direction of Forces, N to B-Build Orientation Filament Arrangement

In this orientation, the tensile test applies forces parallel to the filament layer arrangement as depicted in Figure 4.8. The forces are borne by the whole filament giving an overall higher part strength compared to specimens fabricated in the A-Orientation.

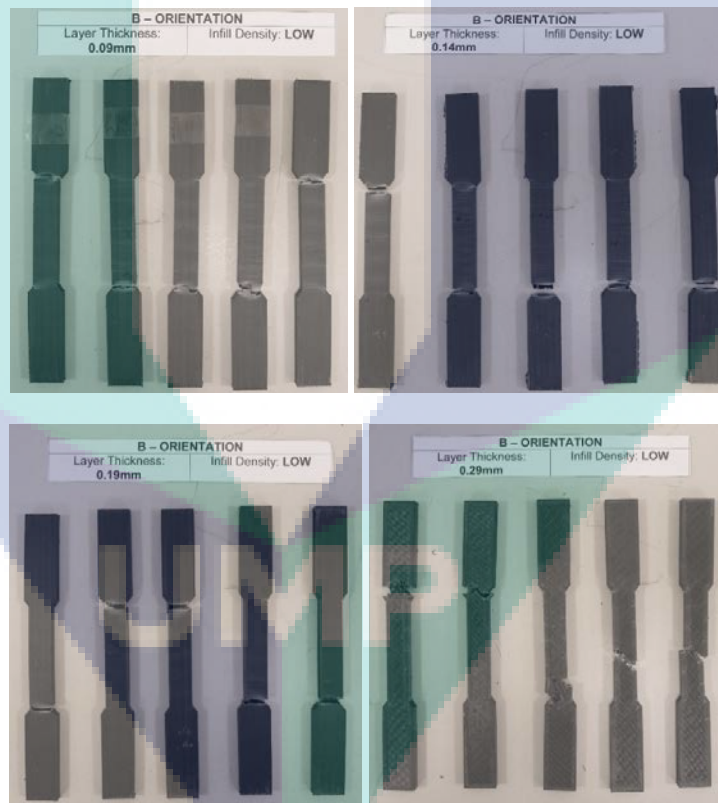


Figure 4.9 Failure Mode of B-Build Orientation for Each Layer Thickness

The fractures that occur in this orientation have a jagged step shape as shown in Figure 4.9. This is due to the layer by layer breakage towards full specimen fracture. This phenomenon also causes the white strips to form due to filament plastic deformation when the specimen is nearing fracture as well the plateauing of the of the stress strain gradient as shown in Figure 4.9.

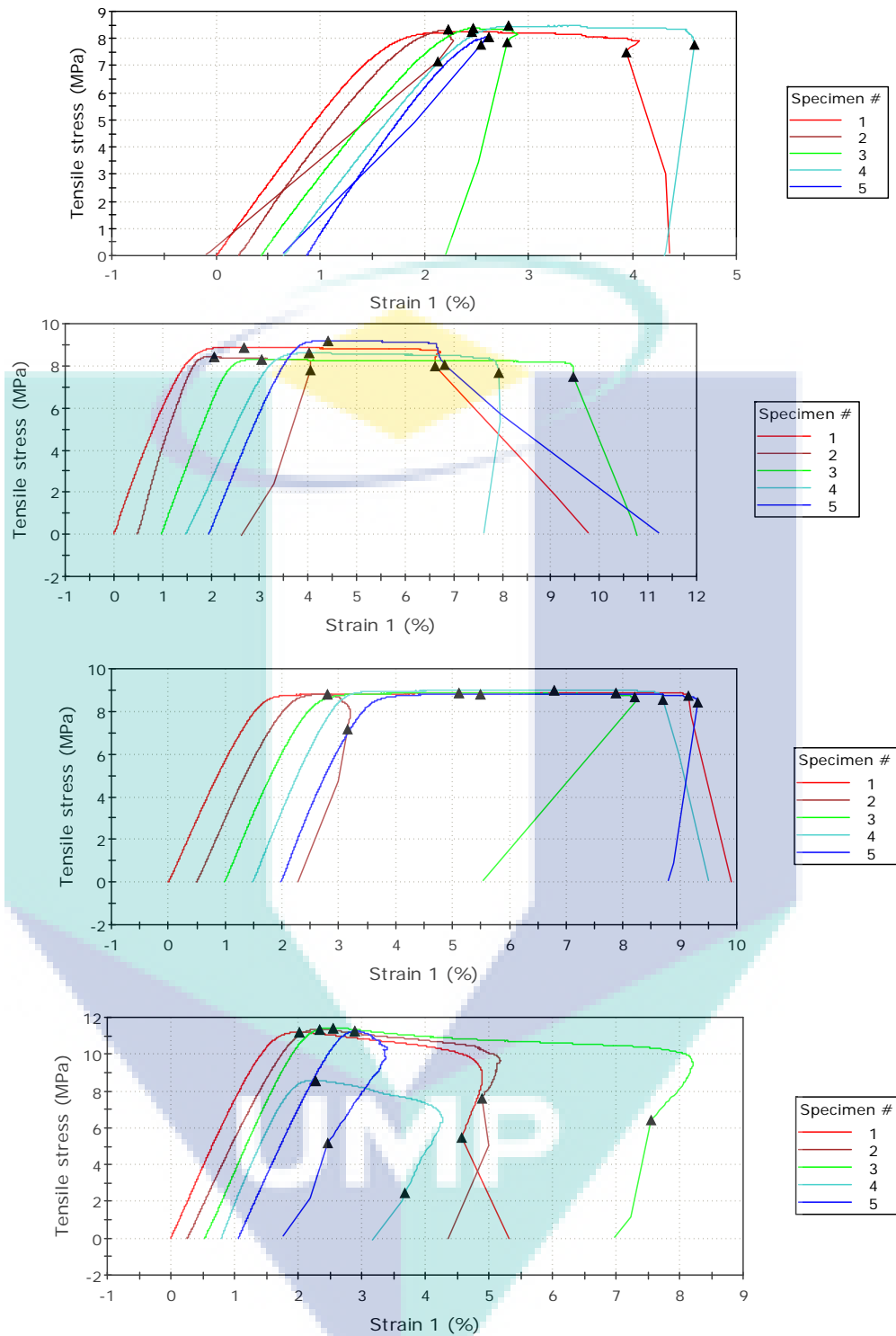


Figure 4.10 C Build Orientation Specimen Stress-Strain Curves for Layer Thickness of 0.09mm, 0.14mm, 0.19mm and 0.29mm (From top to bottom respectively)

Similar to B-Orientation specimens, C-Orientation specimens also exhibits a ductile material like stress-strain curve. The maximum stresses as well as strain are more stable in this orientation in comparison with both A and B Orientation, showing little variation in between samples with the exception of the 0.29 mm layer thickness setting. At 0.29

mm layer thickness, the average maximum stress only varies slightly but the average maximum stress and strain values before break shows a significant amount of variation.

Table 4.5 C-Build Orientation, Low Density Z-ABS Material Properties for Different Layer Thickness (5 Samples for Each Layer Thickness). Values of Properties are of Average Value for 5 Samples.

Layer Thickness	0.09 mm	0.14 mm	0.19 mm	0.29 mm
Maximum Load	755.66 N	791.12 N	807.22 N	979.92 N
Tensile Stress at Maximum Load	8.30 MPa	8.69 MPa	8.87 MPa	10.77 MPa
Tensile Strain at Maximum Load	5.50	1.96	8.82	3.73
Modulus of Elasticity	500.81 MPa	589.44 MPa	586.63 MPa	718.20 MPa
Load at Break	693.56 N	710.64 N	755.65 N	494.83 N
Tensile Stress at Break	7.62 MPa	7.81 MPa	8.30 MPa	5.44 MPa
Tensile Strain at Break	7.18	3.35	11.86	7.97
Tensile Stress at Yield-Zero Slope	8.30 MPa	8.69 MPa	8.87 MPa	11.25 MPa
Maximum Load Standard Deviation	14.03 N	32.58 N	6.82 N	111.64 N
Tensile Stress Standard Deviation	0.15 MPa	0.36 MPa	0.07 MPa	1.23 MPa

As layer thickness increases, tensile stress at maximum load also increases; 8.30 MPa at 0.09 mm, 8.69 MPa at 0.14 mm, 8.87 MPa at 0.19 mm and a sharp increase to 10.77 MPa at 0.29 mm. Average tensile stress and load at break also increases as layer thickness increases except at 0.29 mm filament thickness where the both of these values dip to 5.44 MPa and 494.83 N respectively.

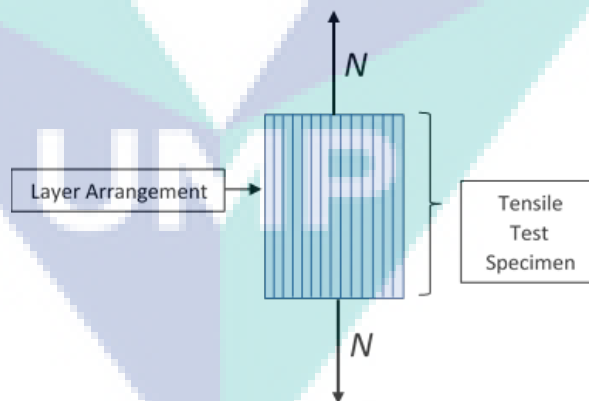


Figure 4.11 Direction of Forces, N to C-Build Orientation Filament Arrangement

Similar to B-Orientation, the tensile forces are parallel to the filament layers as shown in Figure 4.1 with the difference in how the raster layers are aligned. C-build orientation raster arrangement is aligned to the sides whereas in this orientation, the raster is aligned to the front. Force is still applied onto the whole filament for both of these

orientations which explains the near-similar tensile strength values between both B and C build orientations.

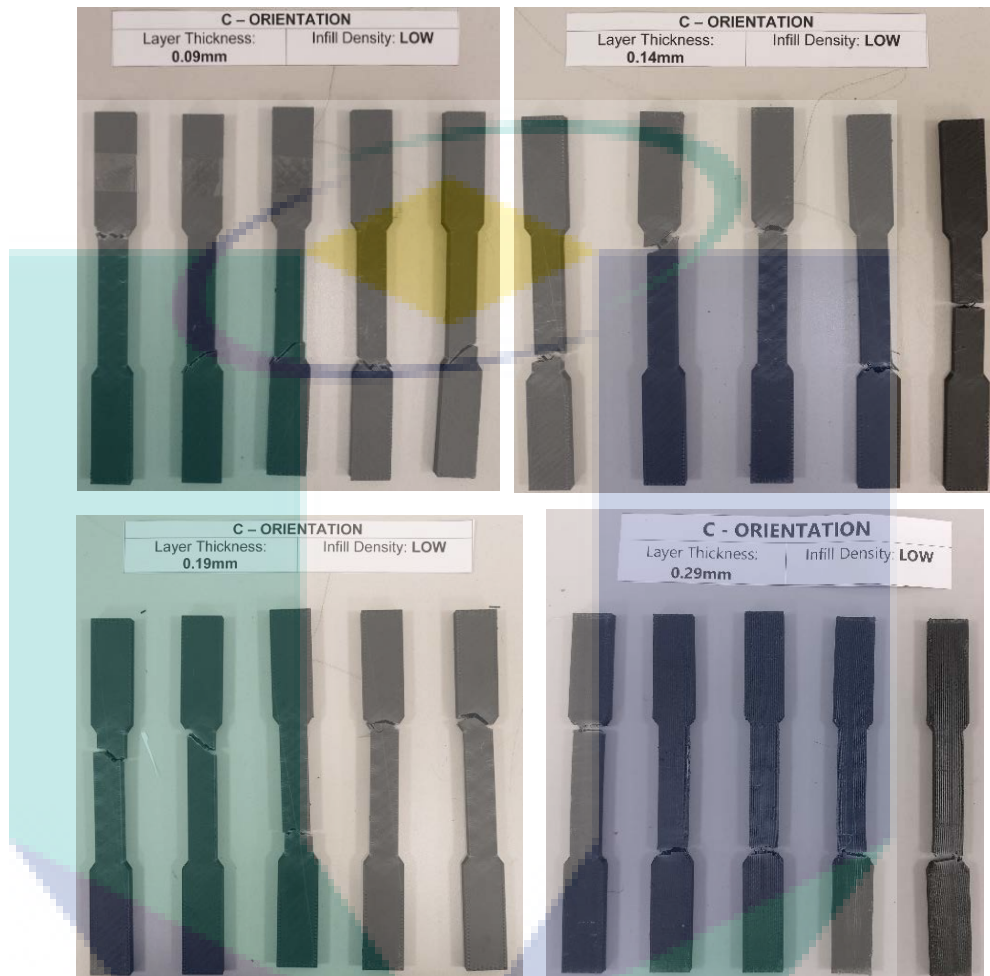


Figure 4.12 Failure Mode of C-Build Orientation for Each Layer Thickness

The fracture shape is again similar to that of B-Orientation. However, the difference in raster alignment causes the specimen to exhibit a criss-cross white plastic deformation pattern (in contrast with B-Orientation's straight white stripe shaped plastic deformation patterns) when the test specimens are approaching the fracture limit as shown in Figure 4.12.

#### 4.2.2 Tensile Test Results for Specimens of Different Infill Densities

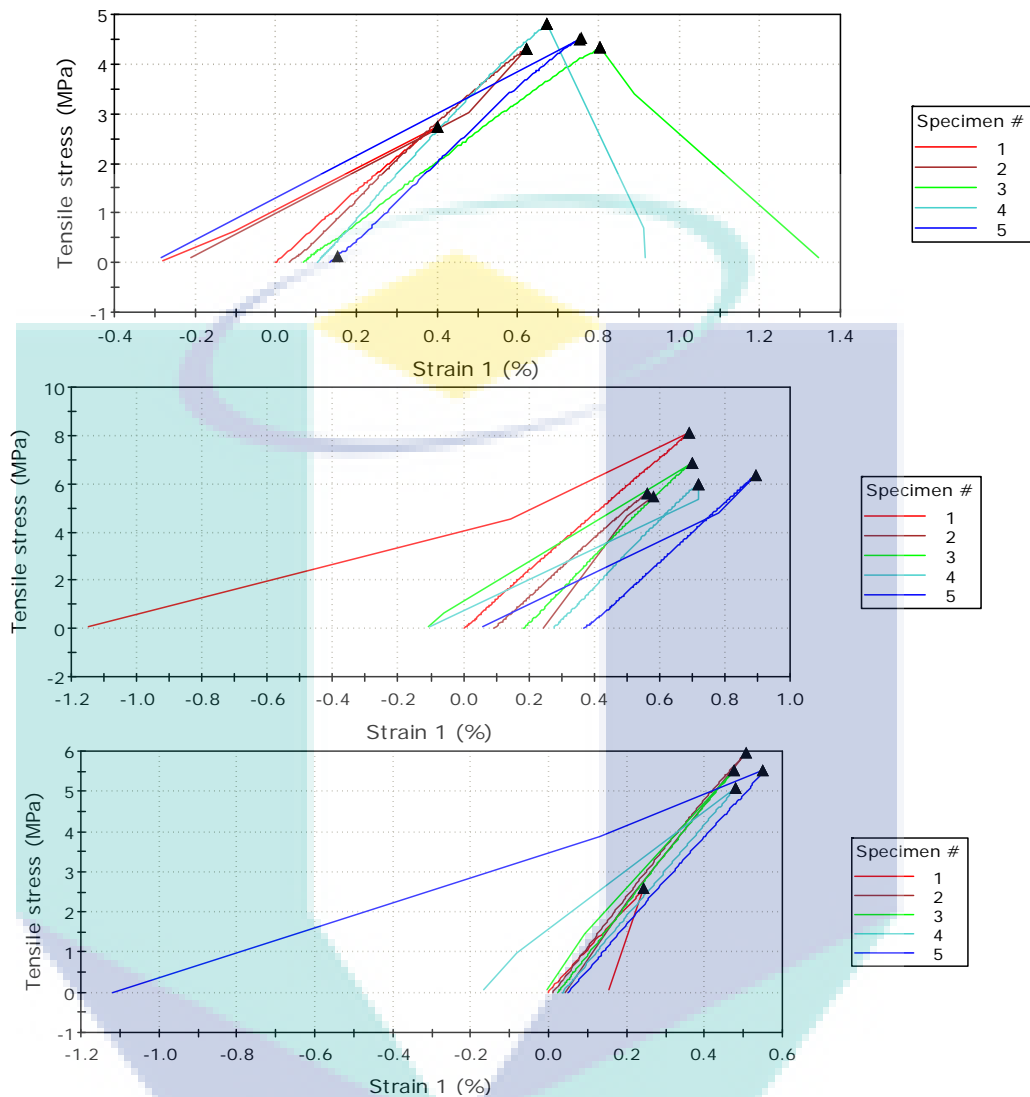


Figure 4.13 A Orientation Specimen Stress Strain Curves for Low, Medium and High Infill Densities (From top to bottom respectively.)

As previously mentioned, the stress-strain curve patterns are similar within same build orientation in which this statement also applies when changing process parameters. Even altering process parameters, the behaviour of the material still follows similar stress strain pattern. In terms of mechanical property stability however, the specimens in the A-build orientation are highly unstable, having large differences in maximum tensile stress in between specimens, with the most unstable having an SD value of 1.34 MPa (SD value of 30% of the sample mean for that process parameter). As the infill density is increased, the SD value also increases indicating increasing differences of measured strength values between tested samples as shown in Table 4.6.

Table 4.6 A-Build Orientation, Constant Layer Thickness of 0.29 mm Material Properties for Different Infill Densities (5 Samples for Each Infill Density Setting).

<b>Part Infill Density</b>	<b>Low</b>	<b>Medium</b>	<b>High</b>
Maximum Load	376.68 N	600.28 N	449.13 N
Tensile Stress at Maximum Load	4.14 MPa	6.60 MPa	4.94 MPa
Tensile Strain at Maximum Load	4.14	1.40	1.11
Modulus of Elasticity	540.46 MPa	748.08 MPa	878.35 MPa
Load at Break	376.38 N	598.32 N	449.13 N
Tensile Stress at Break	4.14 MPa	6.57 MPa	4.94 MPa
Tensile Strain at Break	1.37	1.40	1.11
Tensile Stress at Yield-Zero Slope	3.39 MPa	6.16 MPa	5.38 MPa
Maximum Load Standard Deviation	72.95 N	88.61 N	122.12 N
Tensile Stress Standard Deviation	0.80 MPa	0.97 MPa	1.34 MPa

As exhibited in Table 4.6, the average maximum load and stress from low to medium density settings; 4.14 MPa to 6.60 MPa respectively. However, when highest fill density setting is used, tensile strength exhibited a dip to 4.94 MPa in. Strain at break also follows a similar pattern increasing slightly from 1.37% for low density settings to 1.40% to medium density settings then dipping to 1.11% for high density settings. In terms of part rigidity, rigidity of printed components increases as more higher infill density settings are used.



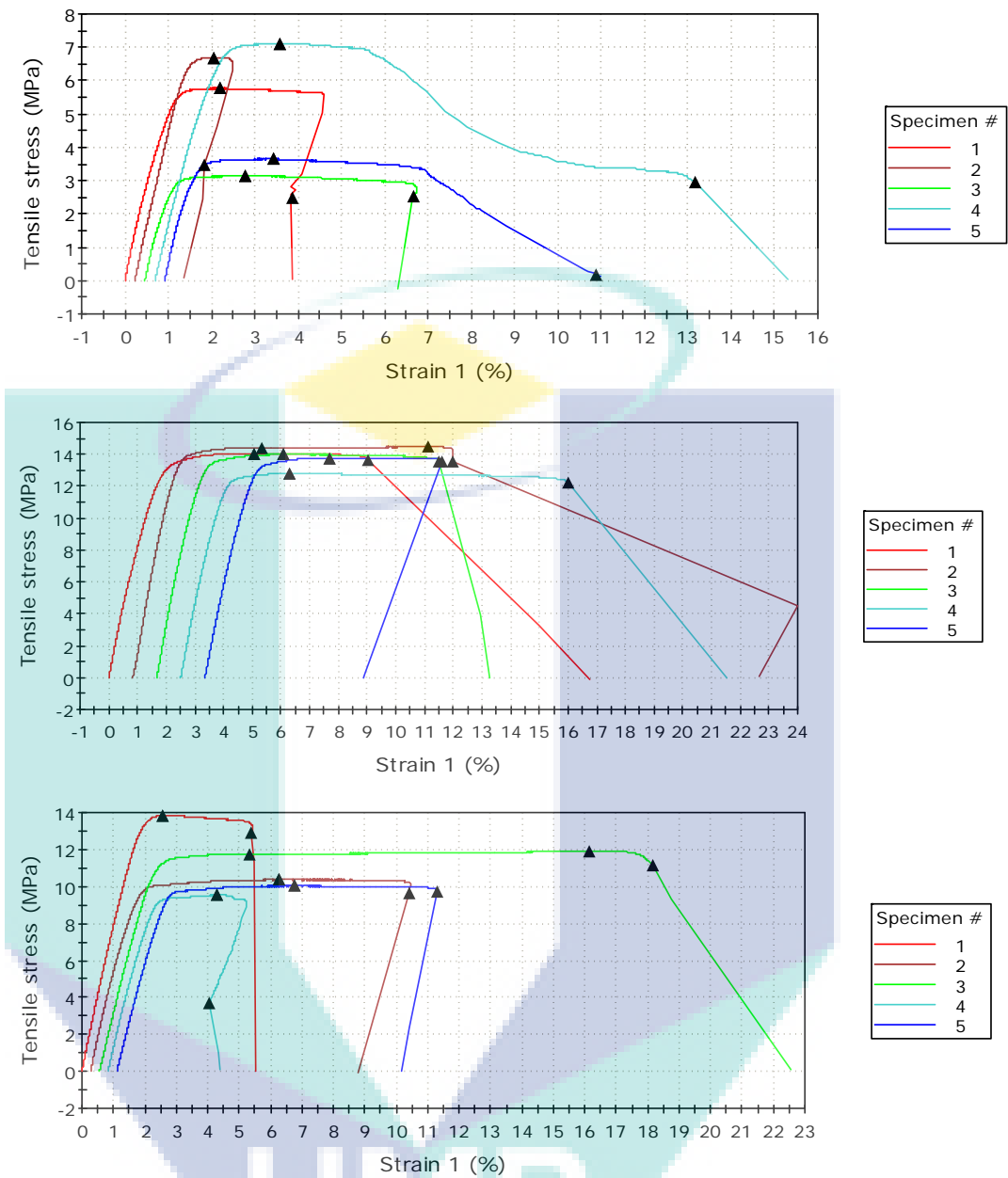


Figure 4.14 B Orientation Specimen Stress Strain Curves for Low, Medium and High Infill Densities (From top to bottom respectively.)

For B-Build Orientation, the lowest density settings yield the lowest tensile strength. The lowest infill density settings yield an average of 5.27 MPa tensile strength which is less than 40% of the highest strength possible attainable tensile strength using the medium infill density settings. Similar to A-Build Orientation, tensile strength peaks at medium infill density settings but dip slightly when the highest density setting is used. In terms of the specimen material properties' stability, it is relatively unstable at the lowest infill density settings having high SD value at 1.79 MPa. Stability is best at

medium infill density settings ( $SD = 0.62$  MPa) but sharply dips at high infill density settings to an  $SD$  value of  $1.75$  MPa.

Table 4.7 B-Build Orientation, Constant Layer Thickness of  $0.29$  mm Material Properties for Different Infill densities (5 Samples for Each Infill Density Setting).

Part Infill Density	Low	Medium	High
Maximum Load	479.57 N	1257.67 N	1013.12 N
Tensile Stress at Maximum Load	5.27 MPa	13.82 MPa	11.13 MPa
Tensile Strain at Maximum Load	5.68	8.83	10.19
Modulus of Elasticity	503.07 MPa	803.29 MPa	646.50 MPa
Load at Break	211.03 N	1210.09 N	857.73 N
Tensile Stress at Break	2.32 MPa	13.30 MPa	9.43 MPa
Tensile Strain at Break	10.32	14.32	14.39
Tensile Stress at Yield-Zero Slope	5.27 MPa	13.81 MPa	11.11 MPa
Maximum Load Standard Deviation	111.64 N	224.26 N	78.64 N
Tensile Stress Standard Deviation	1.79 MPa	0.62 MPa	1.75 MPa

In reference to Table 4.7, the pattern of average tensile stress at maximum load also follows the stability pattern with strength increases from  $5.27$  MPa at low build settings to  $13.82$  MPa at medium then back down again to  $11.13$  MPa. Part rigidity also follows a similar pattern as tensile strength; increasing from low to medium density settings ( $503.07$  MPa to  $803.29$  MPa) then dips at high setting ( $646.50$  MPa).



UMP



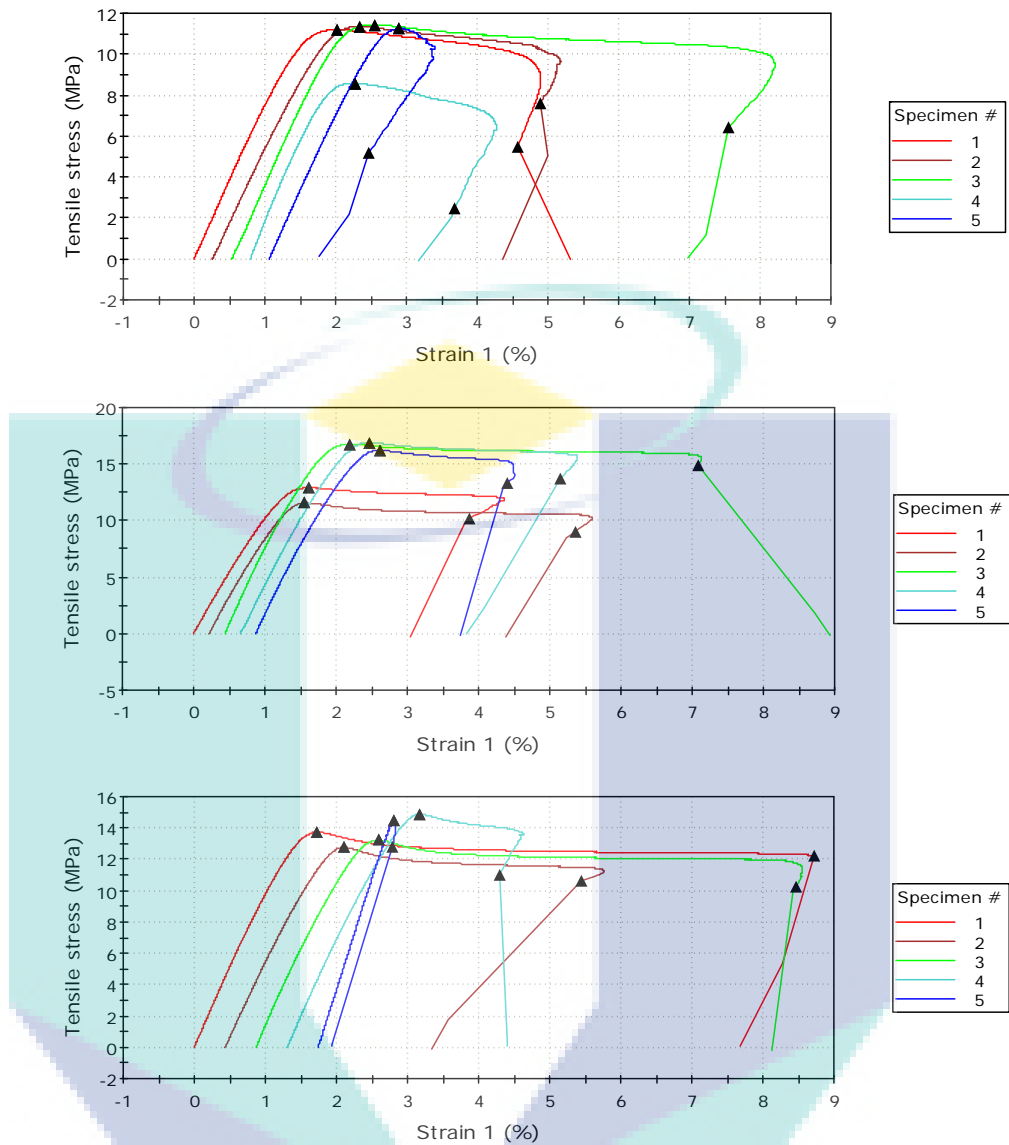


Figure 4.15 C-Orientation Specimen Stress Strain Curves for Low, Medium and High Densities (From top to bottom respectively.)

Generally, all low infill densities settings exhibit low tensile strength properties for the previous orientations. This also applies to C-Orientation. The tensile strength of the specimen is lowest at low density settings (10.77 MPa average), highest at medium infill density settings (14.87 MPa average) and dips slightly at the highest infill density setting (13.81 MPa average). In terms of stress-strain curve shape, the curves throughout infill density settings maintain a similar ductile material shaped stress-strain curve as shown in Figure 4.15. The only difference across build settings are the peak (maximum tensile strength), the strain region of the plastic deformation, as well as the fracturing point.

Table 4.8 C-Build Orientation, Constant Layer Thickness of 0.29 mm Material Properties for Different Infill Densities. (5 Samples for Each Layer Thickness). Values are average for 5 Samples.

<b>Part Infill Density</b>	<b>Low</b>	<b>Medium</b>	<b>High</b>
Maximum Load	979.92 N	1353.40 N	1257.14 N
Tensile Stress at Maximum Load	10.77 MPa	14.87 MPa	13.81 MPa
Tensile Strain at Maximum Load	3.73	3.72	5.45
Modulus of Elasticity	718.20 MPa	1103.33 MPa	995.96 MPa
Load at Break	494.83 N	1112.92 N	1035.88 N
Tensile Stress at Break	5.44 MPa	12.23 MPa	11.38 MPa
Tensile Strain at Break	7.97	8.54	10.52
Tensile Stress at Yield-Zero Slope	11.25 MPa	14.87 MPa	13.81 MPa
Maximum Load Standard Deviation	111.64 N	224.26 N	78.64 N
Tensile Stress Standard Deviation	1.23 MPa	2.46 MPa	0.86 MPa

Although tensile strength peaks at medium density settings, material properties stability shows a different trend. Material stability decreases from low (SD of 1.23 MPa) to medium settings (SD of 2.46 MPa) but sharply increase at high density settings (SD of 0.86 MPa). Part rigidity also follows a similar trend as tensile strength with increasing rigidity from low (718.20 MPa) to medium density settings (1103.33 MPa) then dropping slightly at high infill density settings (995.96 MPa) as shown in Table 4.8. This trend is similar to B-Orientation's infill density trends as well.



### 4.2.3 Summary of Tensile Test Findings and Selection of Process Parameters for Fabrication of AFO

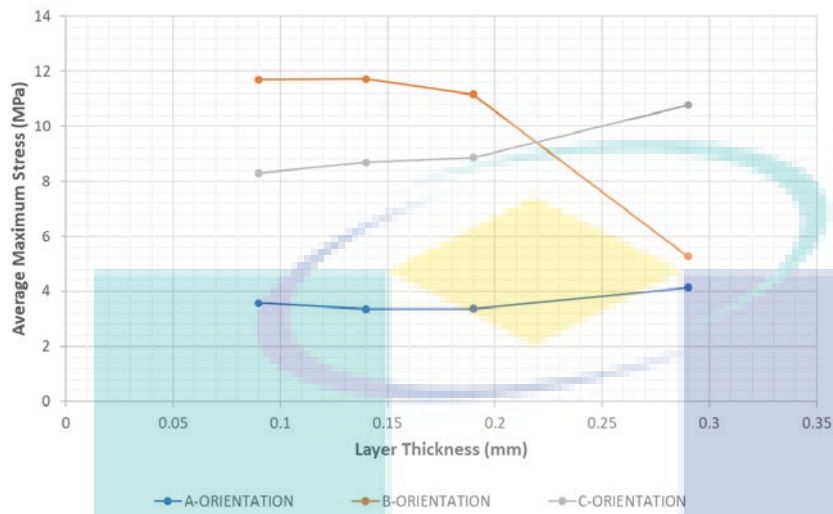


Figure 4.16 Average Maximum Stress (MPa) Across Varying Layer Thickness (mm)

A-Orientation and C-Orientation samples show a similar pattern with increasing average maximum stress values as layer thickness is increased with the 0.29 mm layer thickness setting being the best for highest structural strength. However, for the case of B-Orientation test samples, the average maximum stress values show a steady decline as layer thickness is increased with the largest value dip at 0.29 mm filament thickness setting. These findings on part orientation strength is in line with Cai et al. (2016) and Ranganathan & N.'s (2018) findings.

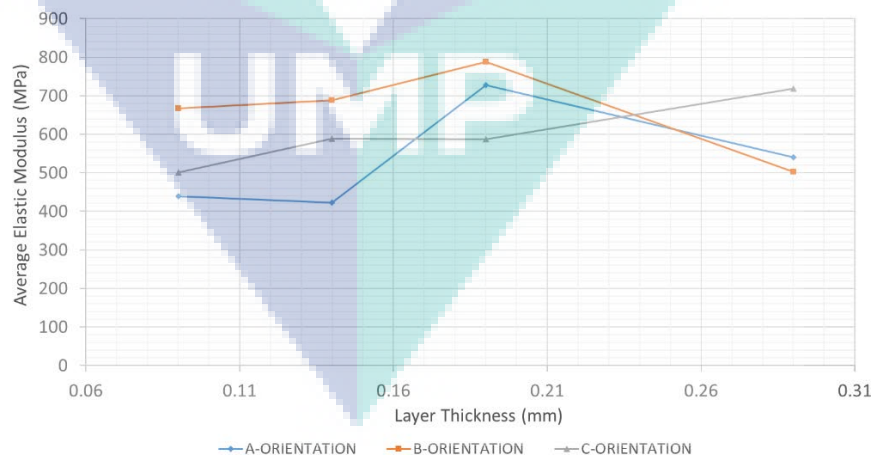


Figure 4.17 Average Elastic Modulus (MPa) Across Varying Layer Thickness Size (mm)

In terms of part rigidity, the patterns are unique for each build orientations. For both A and B build orientations, elastic modulus increases from 0.09 mm to 0.19 mm

layer thickness setting but after that point, part rigidity drops drastically for both orientations. For C-Orientation, rigidity increases as layer thickness increases.

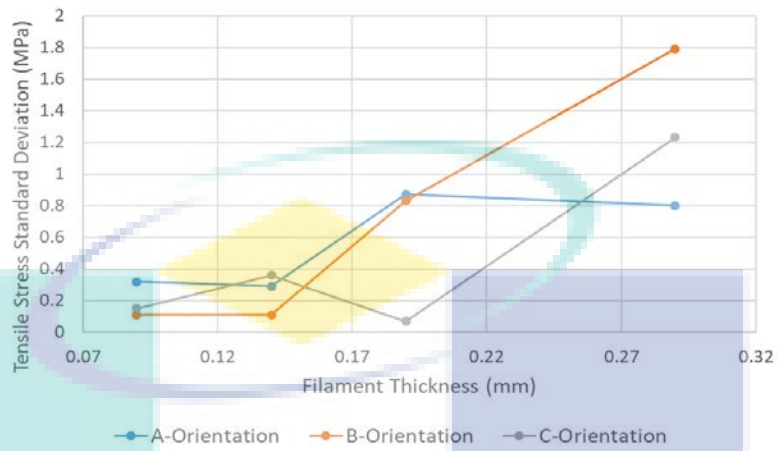


Figure 4.18 Tensile Stress Standard Deviation (MPa) Across Varying Filament Thickness (mm)

For material property stability, the trend is unique for each build orientation. For A orientation, increasing layer thickness from 0.09 mm to 0.19 mm shows increment in stability but falls slightly when filament thickness is further increased after that point. In B orientation, part stability increases as filament thickness with the highest increment from 0.19 mm to 0.29 mm. C-Orientation shows an up and down trend with values increasing from 0.09 mm to 0.14 mm, down from 0.14 mm to 0.19 then sharply raising from 0.19 mm to 0.29 mm.

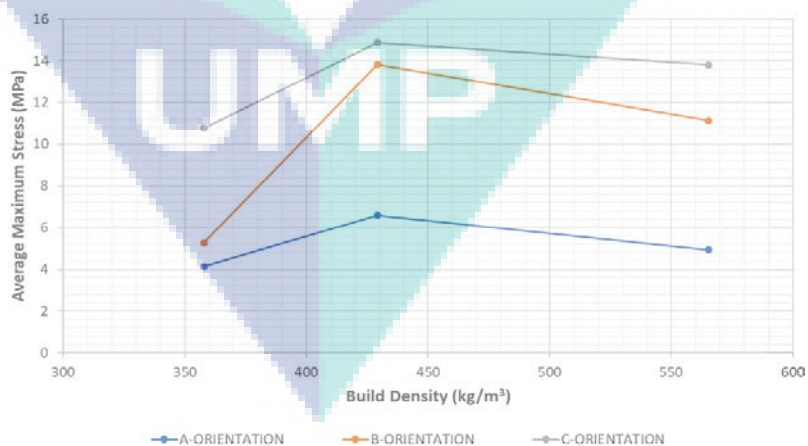


Figure 4.19 Average Maximum Stress (MPa) Across Varying Infill Density Settings (kg/m<sup>3</sup>)

For infill density settings, all 3-build orientation exhibits a similar pattern where part strengths increase from low to medium density settings and then slightly decrease

from medium to high density settings. C-Orientation's medium density settings score the highest part strength among other orientation and infill density settings. B-orientation samples shows the highest increment in average maximum stress values when medium infill density settings are used, closing in to C-Orientation's highest part strength value.

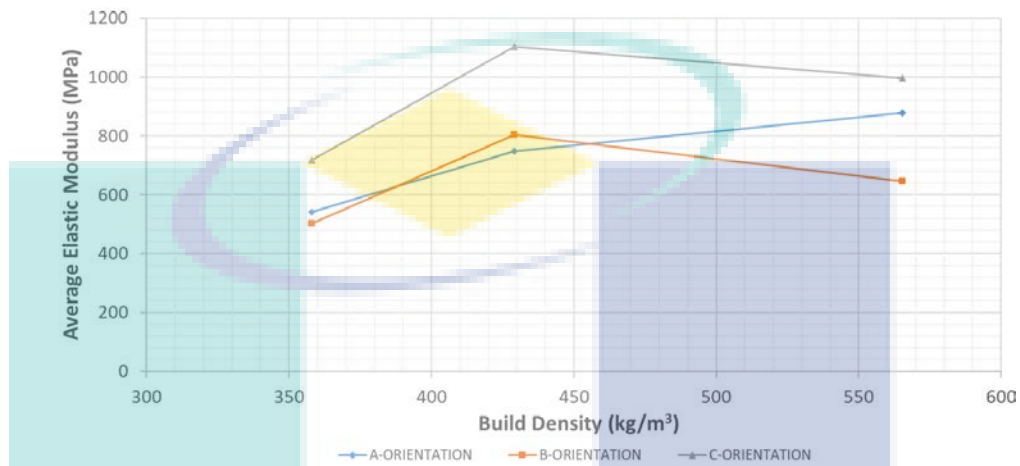


Figure 4.20 Average Elastic Modulus (MPa) Across Varying Infill density Settings (kg/m<sup>3</sup>)

Part rigidity increases as infill density is increased for A build orientation test samples as shown in Figure 4.20. However, the case is different for both B and C build orientations, as the peak in rigidity being the parts fabricated using the medium density settings. Both orientations' rigidity plummets when high infill density settings were used.

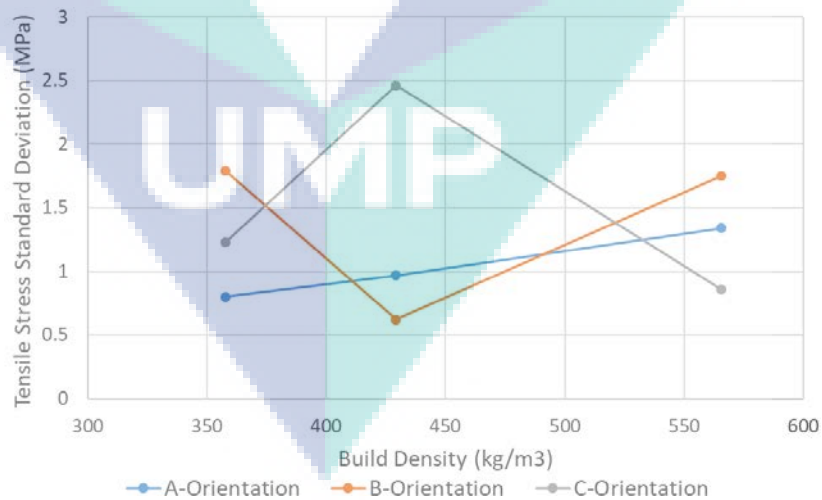


Figure 4.21 Tensile Stress Standard Deviation (MPa) Across Varying Infill density Settings (kg/m<sup>3</sup>)

The trend for stability of material property is different for all respective build orientations. A-orientation shows a linear increase in material property stability as higher

infill densities are used. B-build orientation most stable material property is at the lowest infill density settings. Stability drops after at medium setting followed by an increase at high settings. For C-build orientation, stability peaks at medium settings.

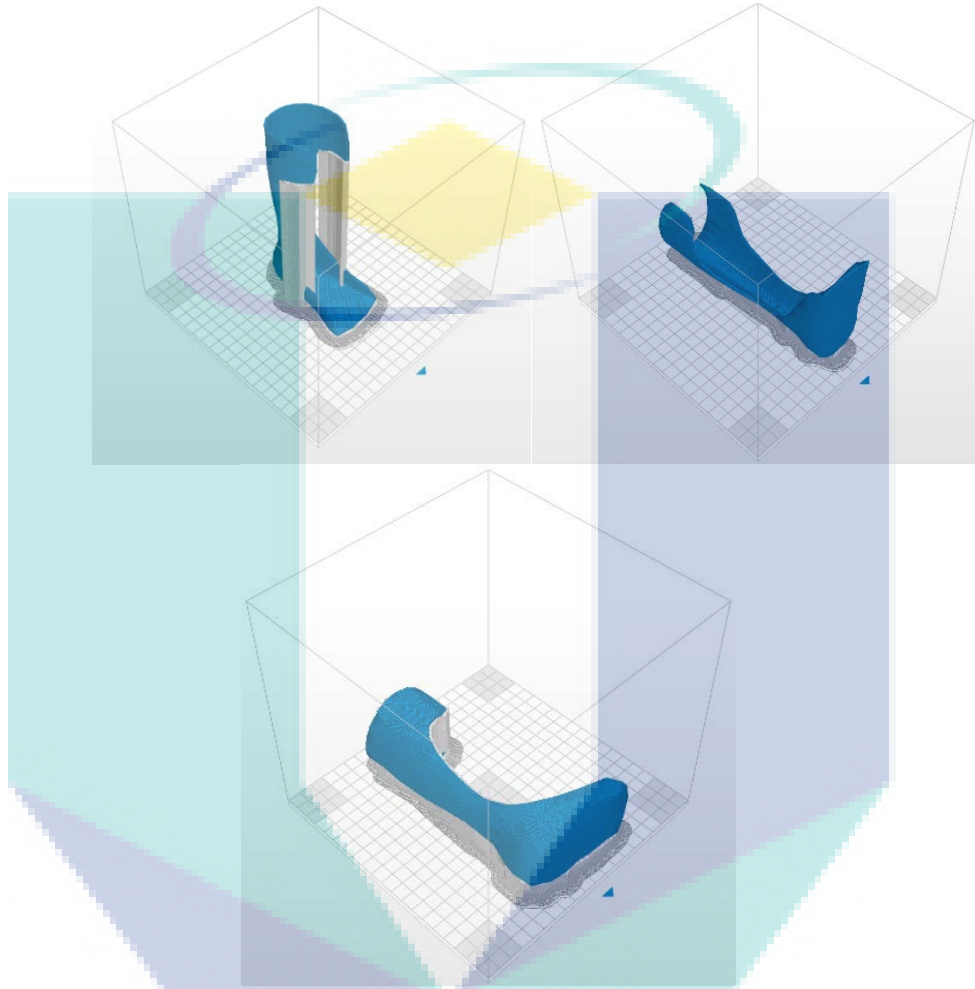


Figure 4.22 Final Printing Geometry with Support Structure Generated by 3D Printer Software (A, B and C Build Orientation Respectively.)

When selecting the most optimum parameters for AFO fabrication it is important to take into consideration the effect of the geometry towards support material usage. Therefore, the consumption of support material is also investigated by loading the un-optimised AFO design to the 3D Printer's Software to obtain a rough estimate of material that will be used for that particular process parameter. Material usage is calculated as mass of printing material used as per Table 4.9.

Table 4.9 Mass of Fabricated AFO (Inclusive of Support Material) Calculated by Z-Suite Software for Different Process Parameters

<b>Build Orientation</b>	<b>0.09 mm LOW</b>	<b>0.14 mm LOW</b>	<b>0.19 mm LOW</b>	<b>0.29 mm LOW</b>	<b>0.29 mm MED</b>	<b>0.29 mm HIGH</b>
A-Build Orientation	165 g	144 g	143 g	147 g	147 g	146 g
B-Build Orientation	147 g	126 g	125 g	159 g	152 g	152 g
C-Build Orientation	275 g	224 g	227 g	284 g	284 g	283 g

The goal is to select a parameter with the highest tensile strength, most rigid and most stable material properties using the least amount of print material. A-build orientation is removed due to the relatively low strength and low material stability in comparison with the other build orientation. C-build orientation while yielding very decent strength, rigidity and material stability falls short due to the high material use. B-build orientation is the best candidate in terms of the aforementioned requirements. The process parameter chosen is B-build orientation with 0.14 mm filament thickness with the infill density of medium. The material properties of the selected process parameter are as in Table 4.10.

Table 4.10 Selected Process Parameter (B-build Orientation, Filament Thickness = 0.14 mm, Medium Infill Density) and Material Properties.

<b>Material Properties</b>	<b>Values</b>
<b>Yield Stress</b>	
XZ-Plane (A-Orientation)	5.32 MPa
XY-Plane (B-Orientation)	11.97 MPa
YZ-Plane (C-Orientation)	11.49 MPa
<b>Modulus of Elasticity</b>	
XZ-Plane (A-Orientation)	583.89 MPa
XY-Plane (B-Orientation)	941.20 MPa
YZ-Plane (C-Orientation)	905.52 MPa
<b>Ultimate Tensile Strength</b>	
XZ-Plane (A-Orientation)	5.34 MPa
XY-Plane (B-Orientation)	11.98 MPa
YZ-Plane (C-Orientation)	12.01 MPa
Density	429.186 kg/m <sup>3</sup>
Total Material Use	126 g

The selected process parameter material properties are used as material definition for the Finite Element Analysis process as well as for fabrication for both the benchmark AFO (Un-optimised) as well as the optimised AFO.

### 4.3 AFO Finite Element Analysis

#### 4.3.1 Heel Strike Gait Phase AFO FEA Results

Extremely high stresses (in the range of 73.28 MPa to a maximum of 93.22 MPa) are concentrated at the lower strut of the AFO with values exceeding the material yield stress (11.97 MPa) by a significant magnitude. This stress concentration occurs due to the direction of the forces of both the forefoot and calf band during heel strike causing a large bending moment to occur in the stress region as shown by the red region in Figure 4.23.

Table 4.11 Minimum and Peak Principal Stress Values for Heel Strike Phase

Subcase	Minimum Principal Stress (MPa)	Element	Maximum Principal Stress (MPa)	Element	Maximum Von Mises Stress (MPa)	Element
Heel Strike	73.28E-07	1175	93.22	6411	89.18	6308

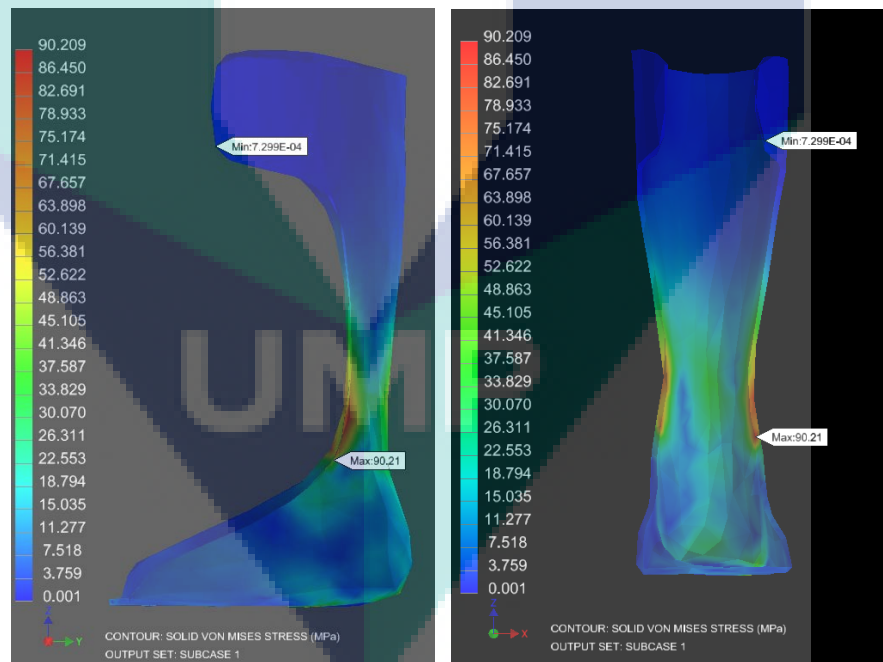


Figure 4.23 Von Misses Stress of AFO During Heel Strike Gait Phase

Large part displacements are also observed in this gait phase especially in the calf region. Table 4.12 describes the element that undergoes the highest displacement in this FEA simulation and its displacement's coordinate components (X, Y, Z). A maximum



total displacement of 57.201 mm is recorded for this element residing in the calf section as denoted in Figure 4.24. This displacement is calculated from the original un-deformed AFO geometry as shown by the red dashed lines in Figure 4.24, right image. Figure 4.24, right visualizes the actual maximum deformed shape once loads are applied. From the strut to the calf section, the displacements observed were in the range of 19.07 mm to 57.201 mm which is considerably high.

Table 4.12 Peak Displacement for AFO FEA of Heel Strike Gait Phase

Subcase	Displacement Components (mm)			Rotation Components (mm)		
	XT	YT	ZT	XR	YR	ZR
Heel Strike	18.51	53.36	21.56	0.0	0.0	0.0

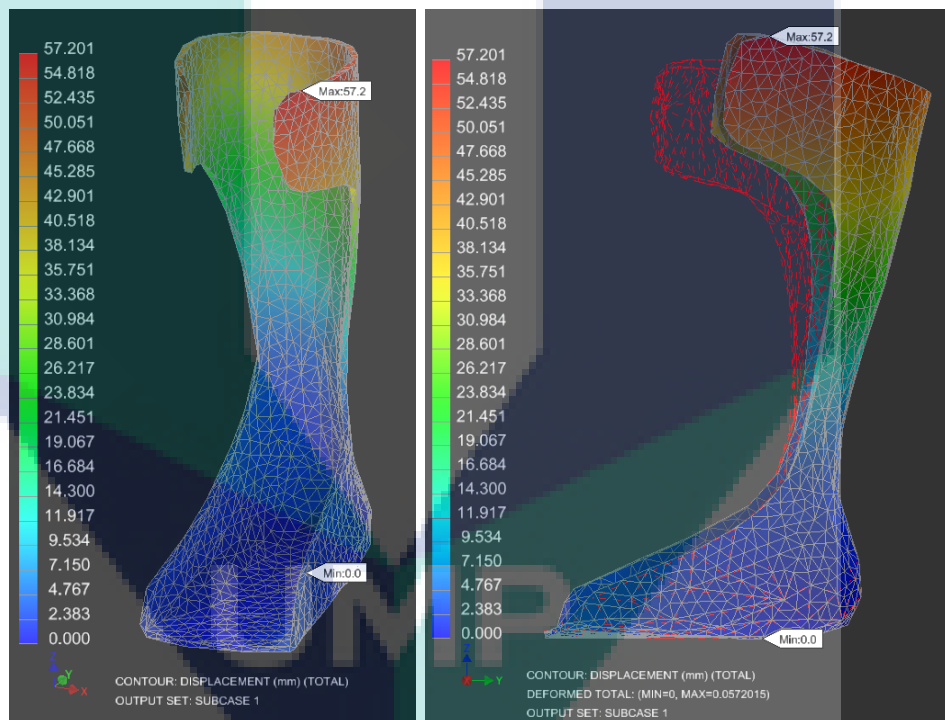


Figure 4.24 Displacement of AFO During Heel Strike Gait Phase

Due to the high concentrated stresses, a low factor of safety (FOS); ranging from 0.201 minimum to 0.63 (which is less than half of the material's yield strength) is observed at the strut of the AFO marked by the red contour in Figure 4.25. This region is likely to be the point of part failure due to the extremely low FOS value. The ankle cup region of the AFO also exhibits small low FOS regions ranging from 0.83 to 1.34 which puts it in areas with high probability of structural failure.

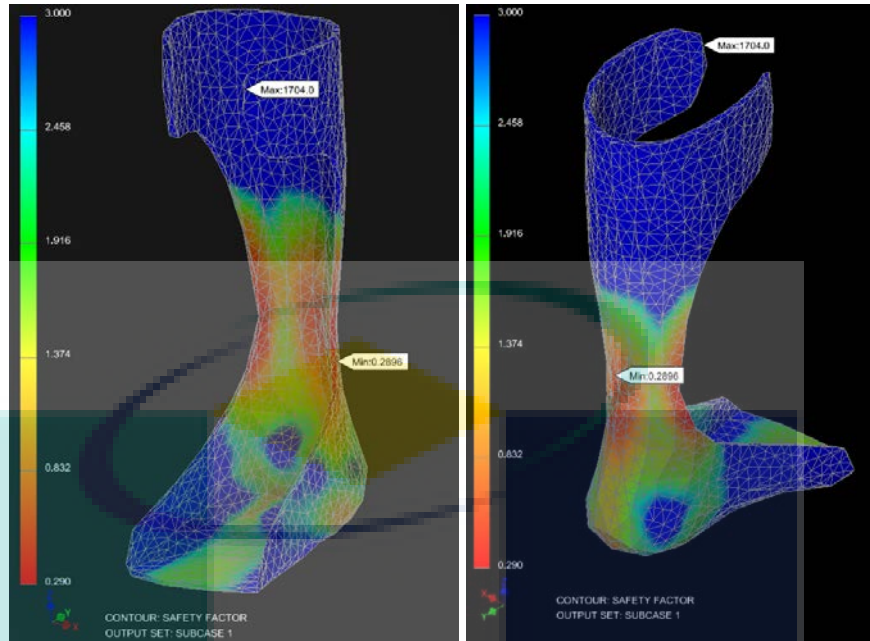


Figure 4.25 Factor of Safety Plot of AFO During Heel Strike Gait Phase

Overall, the heel strike region exhibits the highest deformation and stress magnitude among the other gait phases. Even though the boundary conditions were highly exaggerated (especially the shank force) in this study, the risk of an AFO failing under normal conditions is still significantly high. To alleviate this condition, the stress concentration can be mitigated by altering the AFO geometry to re-distribute the stresses which will be demonstrated in the next section under Topology Optimization.

Although using subjects of different height, weight and nationality, Jamshidi et al.'s (2009) FEA results exhibits a similar von mises stress and displacement distribution; in terms of distribution of magnitudes.

#### 4.3.2 Midstance Gait Phase AFO FEA Results

In contrast to the heel strike phase, the midstance FEA results yield far less maximum stress values. The highest maximum stress is recorded at the heel area with a magnitude of 0.4998 MPa due to how body weight is positioned during standing. Stress is concentrated along the foot region that supports body weight as shown in Figure 4.26.

Table 4.13 Minimum and Peak Principal Stress Values for Midstance Phase

Subcase	Minimum Principal Stress (MPa)	Element	Maximum Principal Stress (MPa)	Element	Maximum Von Mises Stress (MPa)	Element
Subcase 2	0.4998	107	0.3418	Part 1	0.4972	Part 1

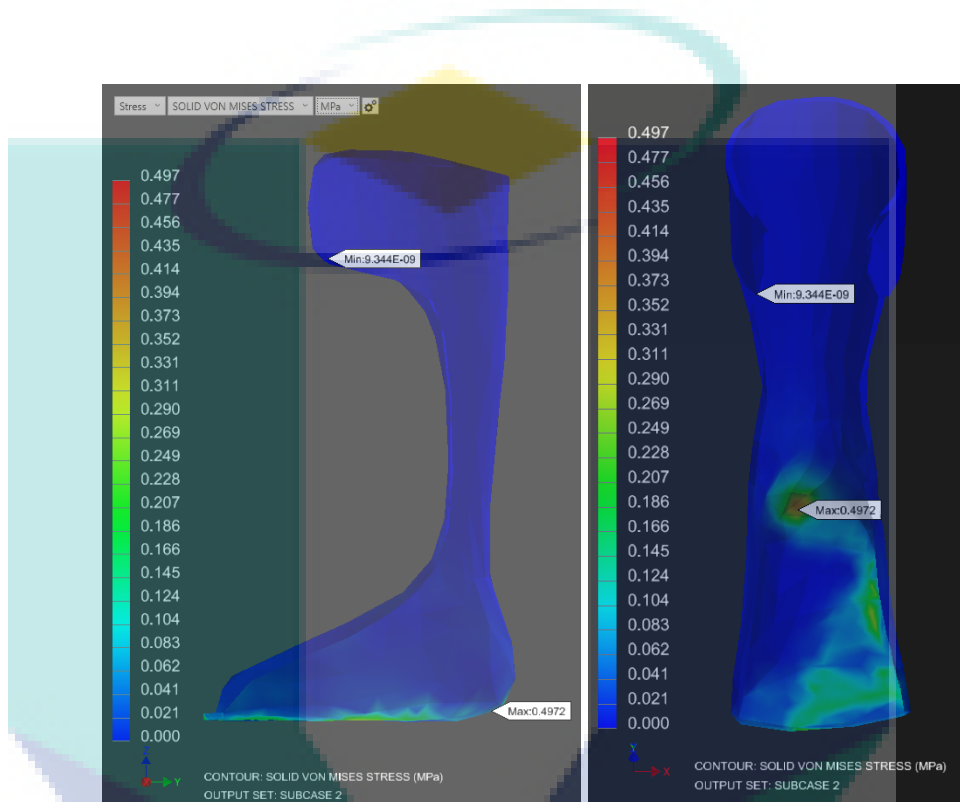


Figure 4.26 Von Misses Stress of AFO During Midstance Gait Phase

In terms of displacement, the peak element displacement recorded in the FEA simulation is only 0.00342 mm which is very small in comparison with the previous gait phase. This is due to the smaller magnitude of stresses involved. As exhibited in Figure 4.27, the displacement region occurs highest at the calf region due to accumulation of displacement value of other elements below it.

Table 4.14 Peak Displacement for AFO FEA of Midstance Gait Phase

Subcase	Displacement Components (mm)			Rotation Components (mm)		
	XT	YT	ZT	XR	YR	ZR
Midstance	3.078E-03	2.017E-03	1.705E-03	0.0	0.0	0.0

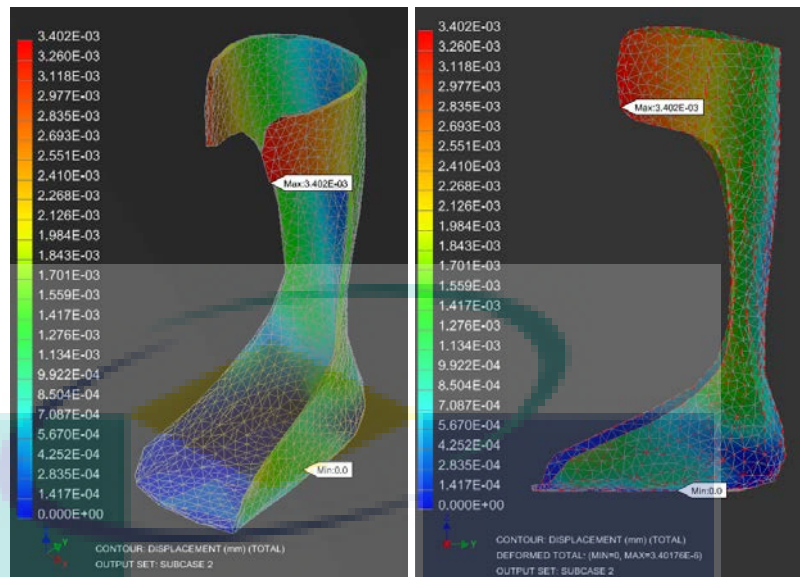


Figure 4.27 Displacement of AFO During Midstance Gait Phase

Load carrying capacity of the whole geometry is largely higher than the actual loads with a high minimum factor of safety of 50.62. This FOS is recorded at the heel contact area due to the concentration of stress there. Other part of the AFO geometry exhibited FOS as high as 50,000 due to minimal loads as shown in Figure 4.28.

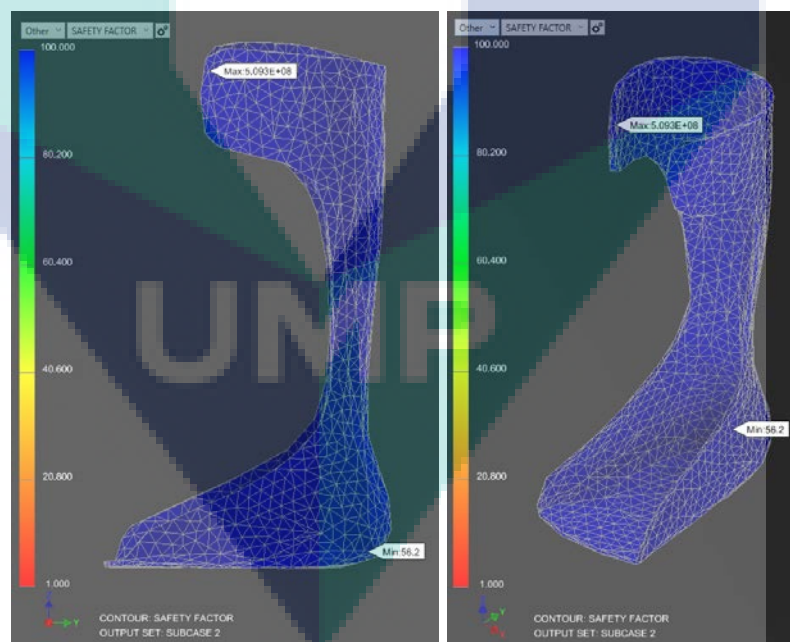


Figure 4.28 Factor of Safety Plot of AFO During Midstance Gait Phase

### 4.3.3 Push Off Gait Phase AFO FEA Results

The push off gait phase is modelled with the forefoot being the pivot for the motion. Hence, stresses due to bending is concentrated at the forefoot of the AFO due to two forces namely the body weight reaction force at the forefoot end (downwards) and the ankle force (upwards) acting at the heel region due to forward propulsion moment by the ankle joint. As shown in Figure 4.29, the peak stress region is concentrated at the forefoot flaps of the AFO.

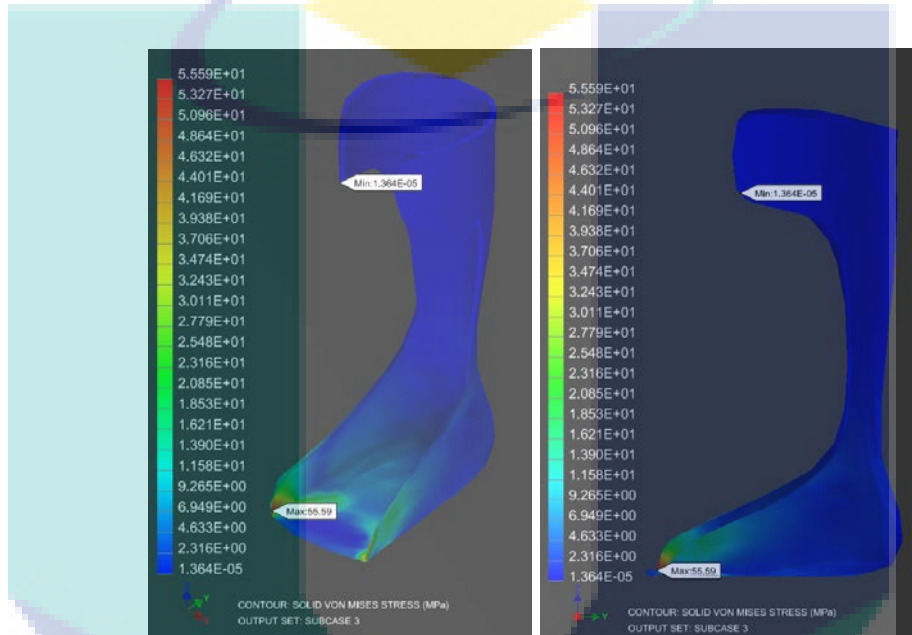


Figure 4.29 Von Misses Stress of AFO During Push Off Gait Phase

The deformation of the AFO during Push Off gait phase is noticeable but is not as excessive as those in the heel strike phase. The highest element displacement is recorded at the calf region as described in Table 4.15 with a magnitude of 16.71 mm. The 16.71 mm value is a cumulative magnitude caused also by the displacement of other elements of the AFO as shown by the shift from the red dashed lines to the deformed geometry in Figure 4.30.

Table 4.15 Peak Displacement for AFO FEA of Midstance Gait Phase

Subcase	Displacement Components (mm)			Rotation Components (mm)		
	XT	YT	ZT	XR	YR	ZR
Midstance	3.078E-03	2.017E-03	1.705E-03	0.0	0.0	0.0

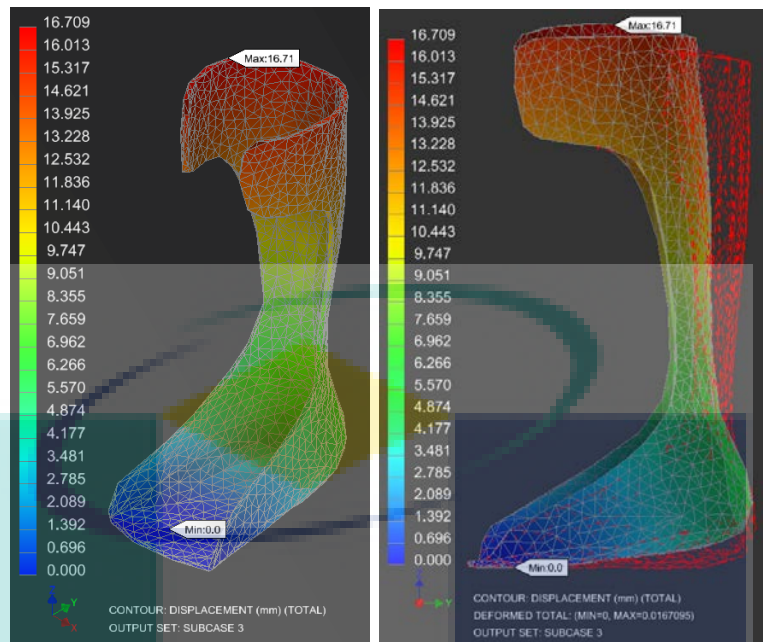


Figure 4.30 Displacement of AFO During Push Off Gait Phase

Overall, the factor of safety for AFO due to loadings under the push off gait phase exhibits high values in a majority of the geometry except the gait pivot region. The FOS value at this region is the lowest in the whole AFO geometry ranging from 1.052 to 1.431, displayed as the red region in Figure 4.31. The FOS value in the region is low, but is acceptable in terms of structural integrity albeit with marginal load headroom.

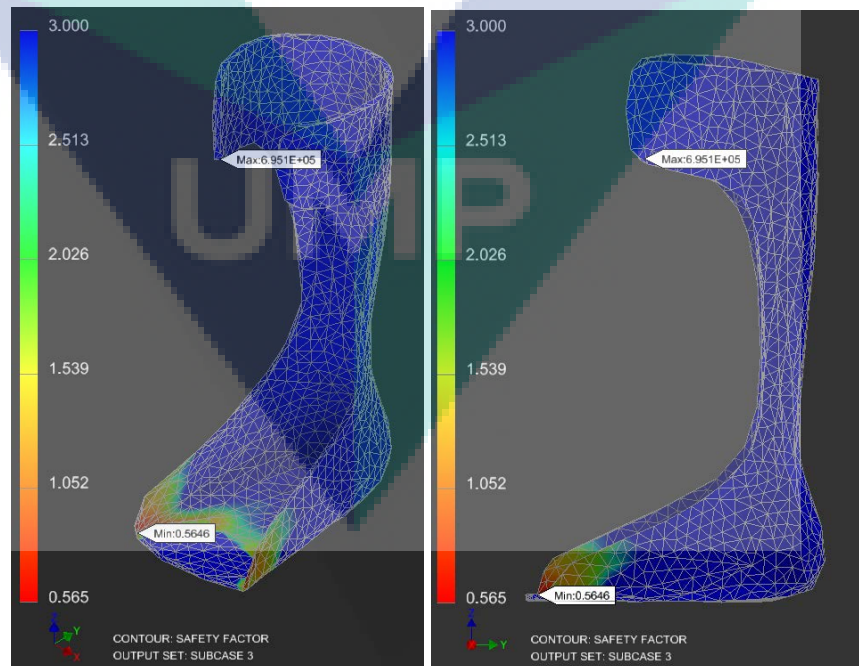


Figure 4.31 Factor of Safety Plot of AFO During Heel Strike Gait Phase

#### 4.4 AFO Topology Optimization Results

Figure 4.32 and Figure 4.33 shows the optimisation design iteration process from start till convergence. The optimisation algorithm removed non-force bearing element in the calf and the foot region as shown in both of the figures. Initially, before the implementation frozen regions, the optimisation would have removed the foot flaps and calf regions completely, leaving only an L-shaped orthosis.

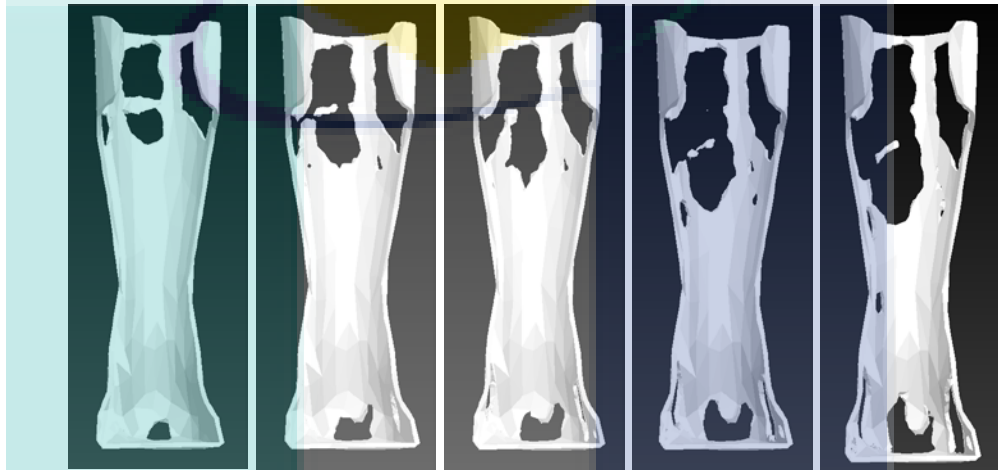


Figure 4.32 Front View Element Removal Process of the AFO Geometry Across Simulation Time (From Left) till Convergence (Right)



Figure 4.33 Side View Element Removal Process of the AFO Geometry Across Simulation Time (From Left) till Convergence (Right)

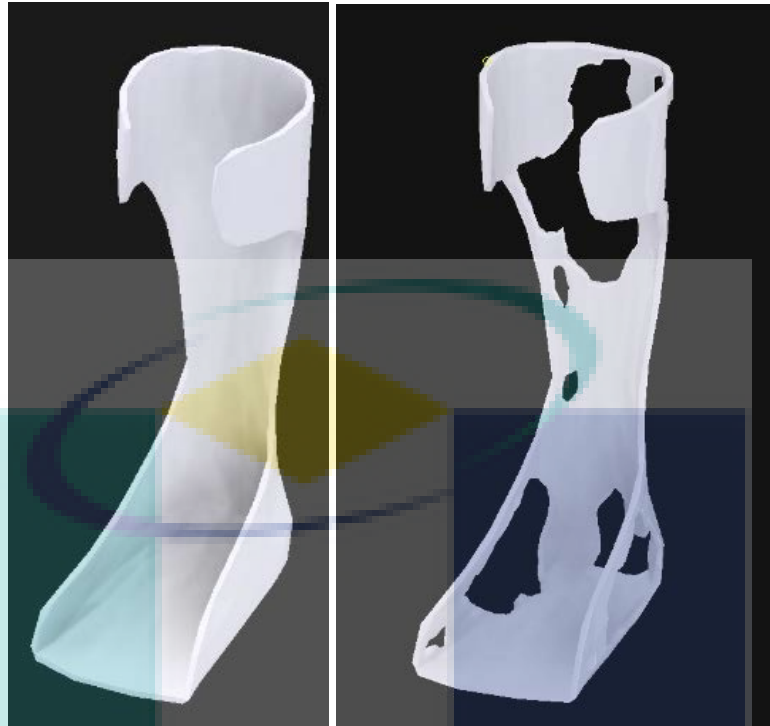


Figure 4.34 Original AFO Geometry (Left) and Optimised Geometry (Right).

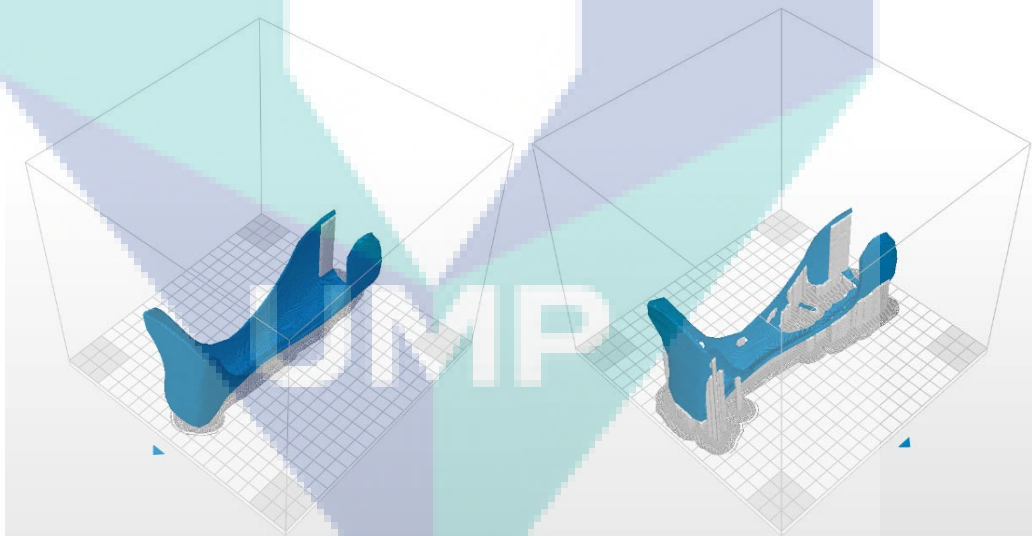


Figure 4.35 Support Material for Original Geometry (Left) and Optimised Geometry (Right)

In the optimisation configuration, the objective weight function is set as mass reduction of 30%. However, in actuality, the optimisation process converges at 29.87% which is reasonably near the target value. As shown in Figure 4.34, the original AFO geometry initially weighing 114 g (126g adding support) is reduced to 80.4 g (97 g adding



support) after the optimisation process. Total time taken for printing the said AFO prototype is 10 hours 41 minutes before optimisation and 9 hours 56 minutes after optimisation. The reason for only slight reduction in printing time after optimisation is due to the added complexity from the optimisation process causing more support structure to be used during the printing process as can be seen when comparing the left (original geometry) and right (optimised geometry) AFO printing geometry in Figure 4.35.

In order to validate the structural integrity of the resultant of the resulting optimised geometry, a finite element analysis is conducted on the said geometry. The boundary conditions used in subchapter 4.3.1, inclusive of the loads and contact areas were re-implemented in this FEA. The only difference is the force application in which foot contact area of the removed geometry is disregarded.

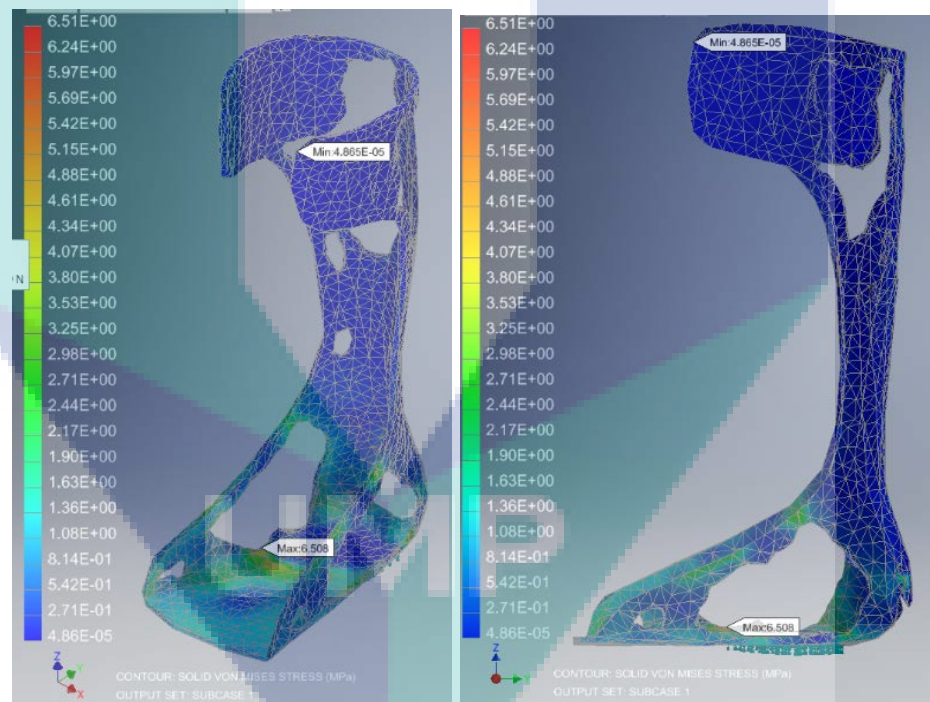


Figure 4.36 Optimised AFO Von Mises Stress

As can be observed from Figure 4.36, the overall force concentration at the neck of the AFO exhibited in the previous chapter had been dispersed to other regions of the AFO geometry. The maximum recorded stress in the optimised geometry is 6.508 MPa in the foot flap region of the AFO. This value is less than the yield stress of the FDM material used (11.97 MPa) and is far less than the un-optimised maximum stress recorded which is 89.18 MPa. Minimum factor of safety also showed similar improvements

increasing from 0.289 (un-optimised) to 4.679 (optimised). In terms of displacement, maximum displacement had decreased slightly from 57.201 mm (un-optimised) to 15.793 mm (optimised).

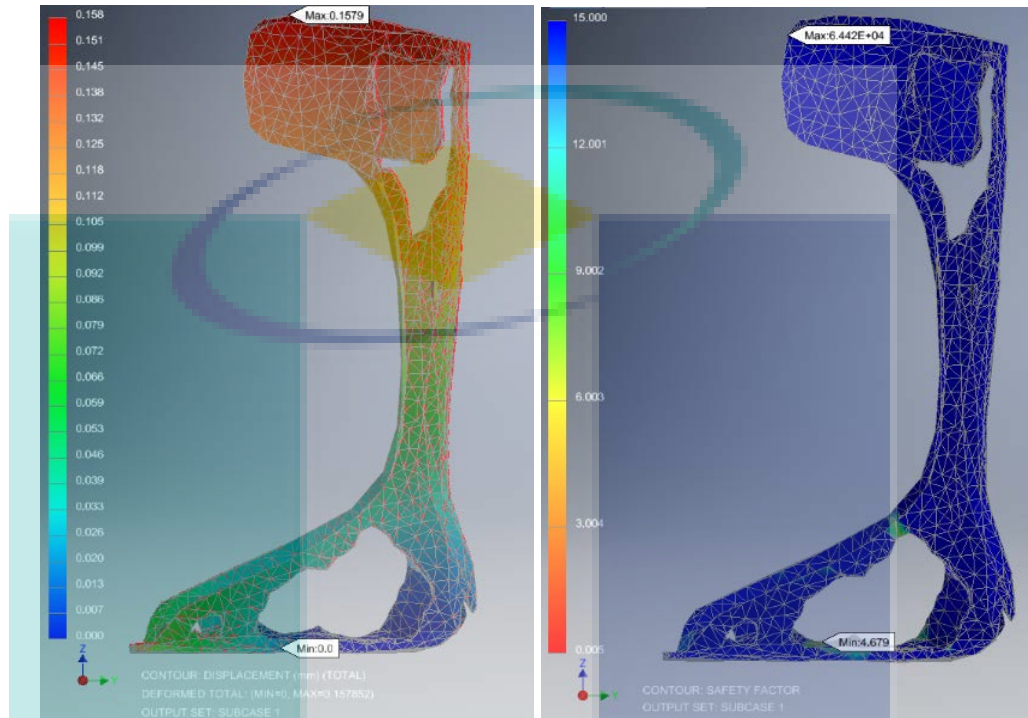


Figure 4.37 Optimised AFO Displacement (Left) and FOS (Right) Plot

#### 4.5 AFO Cost Estimation

The values used in the cost calculation are as listed in Table 4.16. The operators and the designer are set according to the research assistant pay rate since both roles are fulfilled by postgraduate students. The cost for software licensing is inclusive for both the design and analysis software due to the analysis components (Finite Element Analysis and Topology Optimisation) being bundled together with the design software (Autodesk Inventor). Availability, both machine and operator are based on an 8-hour shift, for 22 days a month and 12 months a year. Both power consumption for the personal computer and FDM machine are based on maximum power consumption. Tariffs for the electricity calculations are based on Tenaga Nasional Berhad's Tariff B – Low Voltage Commercial rates obtained from Tenaga Nasional Berhad (2014).

Table 4.16 Parameter Values for AFO Prototype Cost Calculation

Parameters	Un-Optimised Geometry	Optimised Geometry
Processing Cost	RM 26.14	RM 34.85
Personal Computer Cost	RM 3,000.00	RM 3,000.00
Software License Cost	RM 1,577.28	RM 1,577.28
Designer's Cost Per Hour	RM 8	RM 8
PC Availability Time Per Year	2112 hours	2112 hours
PC Energy Consumption Hour Rate	550 W/h	550 W/h
Local Average Energy Specific Cost	RM 0.51/hour	RM 0.51/hour
Designer's Processing Time	3 hours	4 hours
Execution Cost	RM 98.98	RM 92.03
Execution Time	10.683 hours	9.933 hours
Machine Energy Consumption Per Hour	330 W/h	330 W/h
Local Average Energy Specific Cost	RM 0.51/hour	RM 0.51/hour
Maintenance Cost Per Month	RM 10	RM 10
Machine Price	RM 11,448	RM 11,448
Machine Availability	2112 hours	2112 hours
Operator's Cost Per Hour	RM 8/hour	RM 8/hour
Material Cost	RM 35.28	RM 27.16
Total Material Utilised	126 g	126 g
Specific Cost Per Spool	RM 280/spool	RM 280/spool
Total Weight Per Spool	1000 g/spool	1000 g/spool
Total Prototype Cost	RM 160.71	RM 154.33

Based on Table 4.16, the cost savings of performing optimisation is marginal; RM 6.38 reduced cost for an approximate 3% percentage cost reduction. This modest value is due to the additional time required by the designer to produce an optimised AFO design thus incurring a higher processing cost (RM 26.14 for un-optimised geometry vs RM 34.85 for optimised geometry). More time is required to configure as well as perform the topology optimisation process. In addition to that, the additional support structures due to the holes generated by the optimisation process adds material and additional process time further closing in the cost reduction gap between optimised and un-optimised AFOs.

## CHAPTER 5

### CONCLUSION

#### 5.1 Conclusion

Overall, a methodological framework has been developed encompassing the design process till the manufacture of a customised orthosis. The measurement stage employed 3D scanning which greatly reduced the time taken to obtain foot geometry as well as removing the requirements that only trained personnel are able measure anthropometry features. This scanning method proved to be feasible as when benchmarking the scanned foot geometry with current available measurement methods yielded acceptable accuracy results (within 3-5% measurement error).

Designing the AFO prototype virtually via the Inventor CAD demonstrated the simplification of the design process from a manual approach of hand manufacturing multiple casts. Directly from the scanned 3D foot geometry, the AFO design prototype is generated by just a few steps as demonstrated in the previous chapters. In terms of fabrication, FDM is employed allowing for complex shaped AFO to be manufactured without the need of trained AFO specialists. The FDM machine used is a Zortrax M200 which is in itself a low-cost 3D printer. In ensuring the feasibility FDM printed AFOs to be used as a finished product instead of a prototype, a tensile stress test is performed on the printing materials of the FDM process using different printing parameters. The effect of changing printing parameters towards the properties of the printed products namely the strength, rigidity and weight was investigated. Subsequently with the insight from the said study, the printing parameters (B-Orientation, Medium Density) that yields the best strength to printing volume ratio is configured and is used as input for the FEA as well as the fabrication of the final product.

A topology optimisation is performed on the AFO geometry based on the material properties obtained from the tests as well as loads borne by the AFO during its operation. The resultant optimised geometry not only reduced material use it also re-distributed concentrated stresses in the geometry giving an overall increase in FOS from 0.289 to 4.671. The cost reductions are quantified based on a cost calculation model that is a function of time while the structural benefits are weighed via the FEA validation of the final optimised AFO geometry. In terms of cost, the reduction is marginal due to additional process steps during design are needed in order to perform topology optimisation. In terms of structural integrity, the optimisation process succeeded in shifting stress concentration thus fulfilling the final objective of this research.

## **5.2 Limitation of Research Work**

This research work is limited to the investigation of the feasibility of using low-cost scanning method as well as commercially-available 3D printer to fabricate functional patient-specific AFO. Structurally, the AFOs do confirm to the functional requirement which is to support human limbs. However other factors such as ergonomics, long-term efficacy, the effect of using relatively rougher AFO surfaces towards skins and so forth are not within the scope of study of this research.

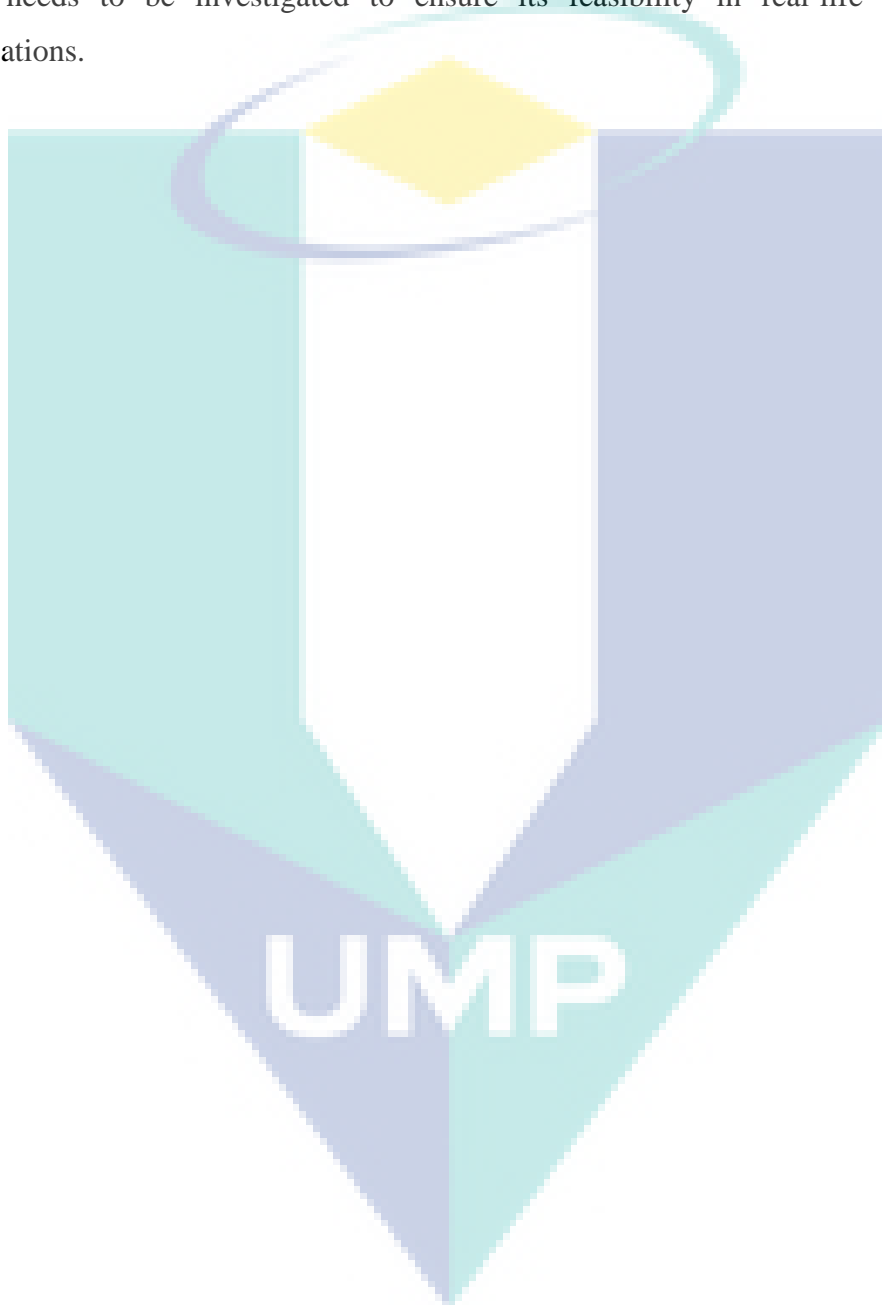
## **5.3 Recommendations for Future Works**

In terms of structural integrity as discussed in Chapter 4.1, different build orientations or layer arrangements translates to different material properties. Higher structural strength could be obtained if each section of the AFO is divided and printed separately according to which parameters imparts upon the highest strength. Further work on printing these regions separately then joining them to a single AFO needs to be done to produce an AFO with optimal structural strength.

Due to the topology optimisation requiring additional time to configure and perform, a software that automates the whole process is necessary to cut down the time and cost that this step incur. This could work could be extended for a PhD study,

employing an algorithm that automatically calculate the AFO boundary conditions based on minimal anthropometry measurements, Finite Element Analysis (FEA) process and AFO Topology Optimisation into one software package.

As mentioned earlier, the medical benefits of the 3D printed, optimised geometry AFO needs to be investigated to ensure its feasibility in real-life rehabilitation applications.



## REFERENCES

- Ahn, S., Montero, M., Odell, D., Roundy, S., & Wright, P. K. (2002). Anisotropic material properties of fused deposition modeling ABS. *Rapid Prototyping Journal*, 8(4), 248–257. <https://doi.org/10.1108/13552540210441166>
- Ashtankar, K. M., Kuthe, A. M., & Rathour, B. S. (2013). Effect of Build Orientation on Mechanical Properties of Rapid Prototyping (Fused Deposition Modelling) Made Acrylonitrile Butadiene Styrene (ABS) Parts. In *Volume 11: Emerging Technologies* (Vol. 11, p. V011T06A017), 1-7. <https://doi.org/10.1115/IMECE2013-63146>
- Becker Orthopedic Appliance. (2003). *Thermoforming Guide*. Troy, Michigan: Becker Orthopedic
- Belegundu, A., & Chandrupatla, T. (2011). *Optimization Concepts and Applications in Engineering*. Upper Saddle River, NJ: Prentice Hall.
- Bellini, A., & Güçeri, S. (2003). Mechanical characterization of parts fabricated using fused deposition modeling. *Rapid Prototyping Journal*, 9(4), 252–264. <https://doi.org/10.1108/13552540310489631>
- Bendsoe, M. P., & Bendsoe, M. P. (1995). *Optimization of Structural Topology, Shape and Material*. Retrieved 12 March, 2017, from <http://www.ltu.se/omltu/ledigajobb/d21826/d21828/1.48687>
- Castiblanco, O., & Shareef, I. (2017). Optimization of StepLock® Orthotic Knee Joint Design. *Procedia Manufacturing*, 10, 622-633. doi:10.1016/j.promfg.2017.07.065
- Cai, L., Byrd, P., Zhang, H., Schlarman, K., Zhang, Y., Golub, M., & Zhang, J. (2016). Effect of Printing Orientation on Strength of 3D Printed ABS Plastics. *TMS 2016: 145th Annual Meeting & Exhibition: Supplemental Proceedings*, 199-204. doi:10.1002/9781119274896.ch25
- Center for Economics and Business Research Ltd. (2011). *The Economic Impact of Improved Orthotic Services Provision*. London: British Healthcare Trades Association.
- Das, S. C., Ranganathan, R., & N., M. (2018). Effect of build orientation on the strength and cost of PolyJet 3D printed parts. *Rapid Prototyping Journal*. doi:10.1108/rpj-08-2016-0137

- European Powder Metallurgy Association. (2015). *Introduction To Additive Manufacturing Technology* (1st ed.). Retrieved 21 December, 2016 from <https://www.epma.com/640-introduction-to-additive-manufacturing-technology-brochure>
- Faustini, M. C., Neptune, R. R., Crawford, R. H., & Stanhope, S. J. (2008). Manufacture of Passive Dynamic Ankle–Foot Orthoses Using Selective Laser Sintering. *IEEE Transactions on Biomedical Engineering*, 55(2), 784-790. <https://doi.org/10.1109/tbme.2007.912638>
- Gibson, I., & Bártolo, P. J. (2011). *History of Stereolithographic Process*. Boston, MA: Springer. <https://doi.org/10.1007/978-0-387-92904-0>
- Gibson, K. S., Woodburn, J., Porter, D., & Telfer, S. (2014). Functionally optimized orthoses for early rheumatoid arthritis foot disease: A study of mechanisms and patient experience. *Arthritis Care and Research*, 66(10), 1456–1464. <https://doi.org/10.1002/acr.22060>
- Hawke, F., Burns, J., Radford, J., & du Toit, V. (2008). Custom foot orthoses for the treatment of foot pain: a systematic review. *Journal of Foot and Ankle Research*, 11(1), 43-46. <https://doi.org/10.1186/1757-1146-1-S1-O46>
- Mello, Martins, Parra, B., Pamplona, Salgado, E., & Seguso, R. (2010). Systematic proposal to calculate price of prototypes manufactured through rapid prototyping an FDM 3D printer in a university lab. *Rapid Prototyping Journal*, 16(6), 411–416. <https://doi.org/10.1108/13552541011083326>
- Hopkinson, N., & Dickens, P. (2003). Analysis of rapid manufacturing - Using layer manufacturing processes for production. *Proceedings of the Institution of Mechanical Engineers, Part C: Journal of Mechanical Engineering Science*, 217(1), 31–39. <https://doi.org/10.1243/095440603762554596>
- Hull, C. (1986). United States Patent No. 4,575,330.
- ICRC. (2010). *Manufacturing Guidelines Ankle-Foot Orthosis*. International Committee of the Red Cross, ICRC. Retrieved 3 July, 2016 from <https://www.icrc.org/eng/assets/files/other/eng-afo-2010.pdf>
- Jang, G. W., Kim, K. J., & Kim, Y. Y. (2008). Integrated topology and shape optimization software for compliant MEMS mechanism design. *Advances in Engineering Software*, 39(1), 1–14. <https://doi.org/10.1016/j.advengsoft.2006.12.003>



- Jin, Y. A., Plott, J., Chen, R., Wensman, J., & Shih, A. (2015). Additive manufacturing of custom orthoses and prostheses - A review. *Procedia CIRP*, 36, 199–204. <https://doi.org/10.1016/j.procir.2015.02.125>
- Jumani, M. S., Shaikh, S., & Khaliqdina, J. H. (2013). Stereolithography Technique for Fabrication of Custom Foot Orthoses: A Cost Benefit Analysis. *Sindh University Research Journal - SURJ (Science Series)*, 45(4), 749–754.
- Kalyani, V. L., & Bansal, D. (2016). Future Communication Technology : A Comparison Between Claytronics And 3-D Printing, 564(2015), 8–28. Retrieved from <http://oaji.net/articles/2016/2725-1472722726.pdf>
- Kilian, S., Zander, U., & Talke, F. E. (2003). Suspension modeling and optimization using finite element analysis. *Tribology International*, 36(4–6), 317–324. [https://doi.org/10.1016/S0301-679X\(02\)00204-9](https://doi.org/10.1016/S0301-679X(02)00204-9)
- Krone, R., & Schuster, P. (2006). An Investigation on the Importance of Material Anisotropy in Finite-Element Modeling of the Human Femur. *SAE Technical Paper Series*, 3(1), 18-24. <https://doi.org/10.4271/2006-01-0064>
- Lin, Y., Lin, K., & Chen, C. (2017). Evaluation of the walking performance between 3D-printed and traditional fabricated ankle-foot orthoses— A prospective study. *Gait & Posture*, 3(1), 1–2. <https://doi.org/10.1016/j.gaitpost.2017.06.471>
- Marro, A., Bandukwala, T., & Mak, W. (2016). Three-Dimensional Printing and Medical Imaging: A Review of the Methods and Applications. *Current Problems in Diagnostic Radiology*, 45(1). <https://doi.org/10.1067/j.cpradiol.2015.07.009>
- Martins, E. (2003). *Contabilidade de Custos*. São Paulo (SP): Atlas.
- Matthew, C., Mary-Ellen, A., & Keith, R. (2011). Reliability of capturing foot parameters using digital scanning and the neutral suspension casting technique. *Journal of Foot and Ankle Research*, 4(1), 9. <https://doi.org/10.1186/1757-1146-4-9>
- Mavroidis, C., Ranky, R. G., Sivak, M. L., Patrilli, B. L., DiPisa, J., Caddle, A., Bonato, P. (2011). Patient specific ankle-foot orthoses using rapid prototyping. *Journal of Neuro Engineering and Rehabilitation*, 8(1), 1. <https://doi.org/10.1186/1743-0003-8-1>
- Olason, A., & Tidman, D. (2010). *Methodology for Topology and Shape Optimization in the Design Process*, 74 - 106. Göteborg: Chalmers University of Technology.

- Organisation Internationale de Normalisation (ISO). (1989). *Prosthetics and orthotics : vocabulary. Part 1, General terms for external limb prostheses and external orthoses = Prothèses et orthèses : vocabulaire. Partie 1, Termes généraux pour prothèses de membre et orthèses externes. TT - (1st ed.). International standard ISO= Norme internationale ISO; 8549-1; Normes ISO (Organisation internationale de normalisation); 8549-1. TA -*. Genève, Switzerland : International Organization for Standardization,.
- Palermo, E. (2013). Fused Deposition Modeling: Most Common 3D Printing Method, 2016(11th March). Retrieved March 11, 2017, from <http://www.livescience.com/39810-fused-deposition-modeling.html>
- Pallari, J. H. P., Dalgarno, K. W., & Woodburn, J. (2010). Mass customization of foot orthoses for rheumatoid arthritis using selective laser sintering. *IEEE Transactions on Biomedical Engineering*, 57(7), 1750–1756. <https://doi.org/10.1109/TBME.2010.2044178>
- Park, J. H., Noh, S. C., Jang, H. S., Yu, W. J., Park, M. K., & Choi, H. H. (2009). The Study of Correlation between Foot-pressure Distribution and Scoliosis. *IFMBE Proceedings 13th International Conference on Biomedical Engineering*, 974-978. [https://doi.org/10.1007/978-3-540-92841-6\\_241](https://doi.org/10.1007/978-3-540-92841-6_241)
- Peter W. Christensen, A. K. (2009). *An Introduction to Structural Optimization*. Berlin: Springer Netherland.
- Plagenhoef, S., Evans, F. G., & Abdelnour, T. (1983). Anatomical Data for Analyzing Human Motion. *Research Quarterly for Exercise and Sport*, 54(2), 169–178. <https://doi.org/10.1080/02701367.1983.10605290>
- Pucci, J. U., Christophe, B. R., Sisti, J. A., & Connolly, E. S. (2017). Three-dimensional printing: technologies, applications, and limitations in neurosurgery. *Biotechnology Advances*, 35(5), 521–529. <https://doi.org/10.1016/j.biotechadv.2017.05.007>
- Rao, N., Wening, J., Hasso, D., Gnanapragasam, G., Perera, P., Srigiriraju, P., & Aruin, A. S. (2014). The Effects of Two Different Ankle-Foot Orthoses on Gait of Patients with Acute Hemiparetic Cerebrovascular Accident. *Rehabilitation Research and Practice*, 2014, 1–7. <https://doi.org/10.1155/2014/301469>
- Saleh, J. M. (2013). *Cost Modelling of Rapid Manufacturing Based Mass Customisation System For Fabrication of Custom Foot Orthoses* (Doctoral Dissertation). Retrieved 7 February, 2016, from <https://theses.ncl.ac.uk/dspace/handle/10443/2193>

- Schmid, M., Kleijnen, R., Vetterli, M., & Wegener, K. (2017). Influence of the Origin of Polyamide 12 Powder on the Laser Sintering Process and Laser Sintered Parts. *Journal of Applied Sciences*, 7(5), 462. <https://doi.org/10.3390/app7050462>
- Schrank, E. S., & Stanhope, S. J. (2011). Dimensional accuracy of ankle-foot orthoses constructed by rapid customization and manufacturing framework. *Journal of Rehabilitation Research and Development*, 48(1), 31–42. <https://doi.org/10.1682/JRRD.2009.12.0195>
- Singh, S., Sachdeva, A., & Sharma, V. S. V. (2012). Investigation of Dimensional Accuracy / Mechanical Properties of Part Produced by Selective Laser Sintering. *International Journal of Applied Science and Engineering*, 1, 59–68. <https://doi.org/10.1081/j.asce.39941>
- Singiresu S. Rao. (2009). *Engineering Optimization: Theory and Practice*. New Jersey: John Wiley & Sons
- Sutradhar, A., Paulino, G. H., Miller, M. J., & Nguyen, T. H. (2010). Topological optimization for designing patient-specific large craniofacial segmental bone replacements. *Proceedings of the National Academy of Sciences*, 107(30), 13222–13227. <https://doi.org/10.1073/pnas.1001208107>
- Taha, Z., Aris, M. A., Ahmad, Z., Hassan, M. H. A., & Sahim, N. N. (2013). A Low Cost 3D Foot Scanner for Custom-Made Sports Shoes. *Applied Mechanics and Materials*, 440, 369–372. <https://doi.org/10.4028/www.scientific.net/AMM.440.369>
- Telfer, S., Abbott, M., Steultjens, M., Rafferty, D., & Woodburn, J. (2013). Dose-response effects of customised foot orthoses on lower limb muscle activity and plantar pressures in pronated foot type. *Gait and Posture*, 38(3), 443–449. <https://doi.org/10.1016/j.gaitpost.2013.01.012>
- Telfer, S., Pallari, J., Munguia, J., Dalgarno, K., McGeough, M., & Woodburn, J. (2012). Embracing additive manufacture: implications for foot and ankle orthosis design. *BMC Musculoskeletal Disorders*, 13(1), 84-91. <https://doi.org/10.1186/1471-2474-13-84>
- Telfer, S., & Woodburn, J. (2010). The use of 3D surface scanning for the measurement and assessment of the human foot. *Journal of Foot and Ankle Research*, 3(1), 19. <https://doi.org/10.1186/1757-1146-3-19>
- Tenaga Nasional Berhad. (2014). TNB Electricity Tariff Rates. Retrieved March 3, 2017, from

- Trotter, L. C., & Pierrynowski, M. R. (2008). The short-term effectiveness of full-contact custom-made foot orthoses and prefabricated shoe inserts on lower-extremity musculoskeletal pain: a randomized clinical trial. *Journal of the American Podiatric Medical Association*, 98(5), 357–363. <https://doi.org/98/5/357> [pii]
- Tymrak, B. M., Kreiger, M., & Pearce, J. M. (2014). Mechanical properties of components fabricated with open-source 3-D printers under realistic environmental conditions. *Materials and Design*, 58, 242–246. <https://doi.org/10.1016/j.matdes.2014.02.038>
- Upadhyay, K., Dwivedi, R., & Singh, A. K. (2017). Determination and Comparison of the Anisotropic Strengths of Fused Deposition Modelling P400 ABS. *Advances in 3D Printing & Additive Manufacturing Technologies*, 9-28. <https://doi.org/10.1007/978-981-10-0812-2>
- Vidakis, N., Vairis, A., Petousis, M., Savvakis, K., & Kechagias, J. (2016). Fused Deposition Modelling Parts Tensile Strength Characterisation. *Academic Journal of Manufacturing Engineering*, 14(2), 87–94.
- Walbran, M., Turner, K., & McDaid, A. J. (2016). Customized 3D printed ankle-foot orthosis with adaptable carbon fibre composite spring joint. *Cogent Engineering*, 3(1), 1–11. <https://doi.org/10.1080/23311916.2016.1227022>
- Wong, M., Wong, D., & Wong, A. (2010). A Review of Ankle Foot Orthotic Interventions for Patients with Stroke. *The Internet Journal of Rehabilitation*, 1(1), 2-4. <https://doi.org/10.5580/26b3>
- Wong, K. V., & Hernandez, A. (2012). A Review of Additive Manufacturing. *ISRN Mechanical Engineering*, 2012, 1–10. <https://doi.org/10.5402/2012/208760>
- Xu, F., Wong, Y. S., & Loh, H. T. (2000). Toward generic models for comparative evaluation and process selection in rapid prototyping and manufacturing. (2002). *Journal of Manufacturing Systems*, 21(6), 471. [https://doi.org/10.1016/s0278-6125\(02\)80076-0](https://doi.org/10.1016/s0278-6125(02)80076-0).
- Yasuhiro Mine, Takamichi Takashima, H. F. (2006). *Study of the Design Method of an Ankle-Foot-Orthosis. Mechatronics for Safety, Security and Dependability in a New Era*. Elsevier Ltd. <https://doi.org/10.1016/B978-008044963-0/50007-2>

## APPENDIX A BLACK TO WHITE RATIO MATLAB CODE

% Replace <> with relevant parameters. Avoid special characters

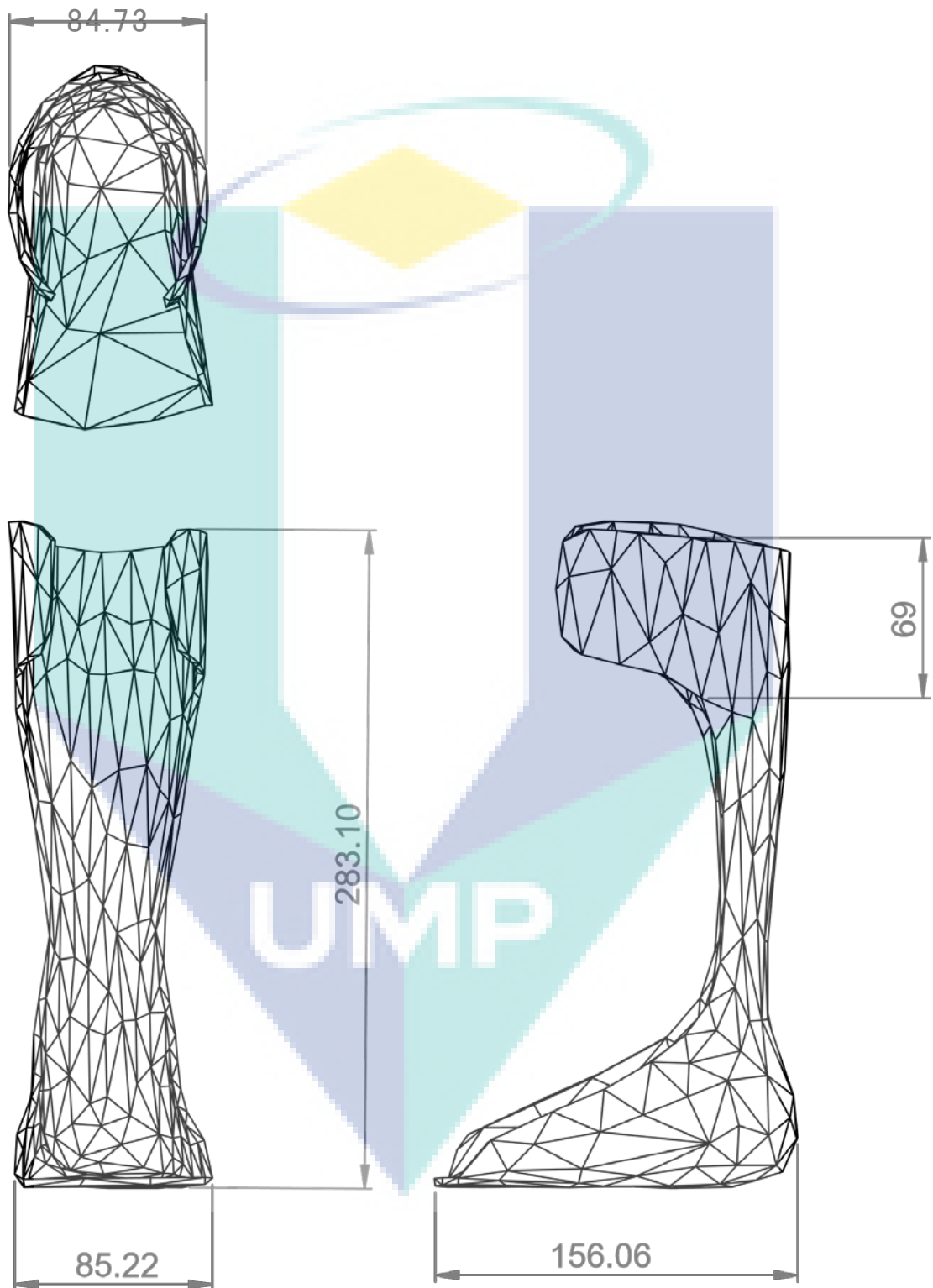
% <imagenamename.format> where img = image name, format = type of image; jpg

```
IMG = imread('<img. format>');  
figure; imshow(IMG)  
IMG = im2bw(RGB,<RGB Level Value>);  
figure, imshow(IMG)  
percentageBlack=(1-nnz(IMG)/numel(IMG))*100
```

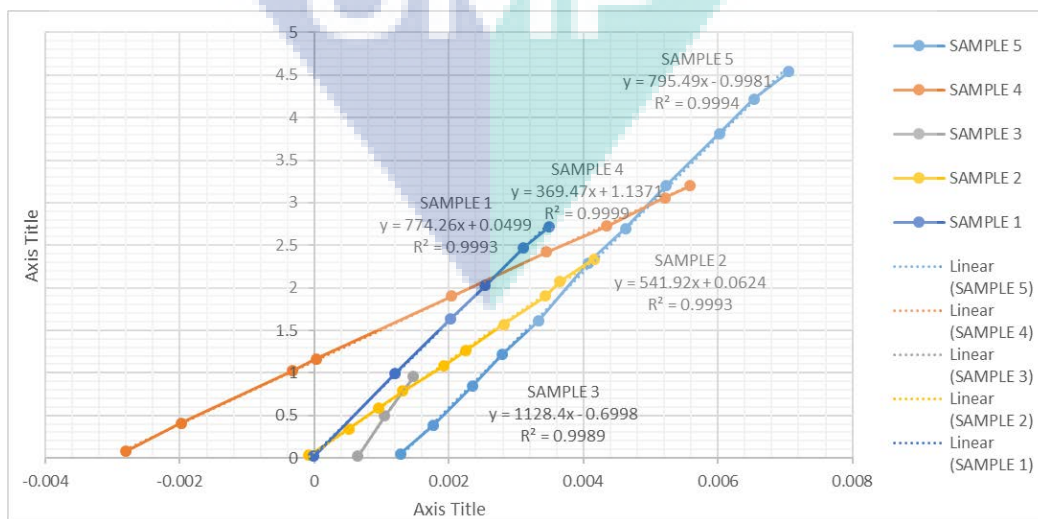
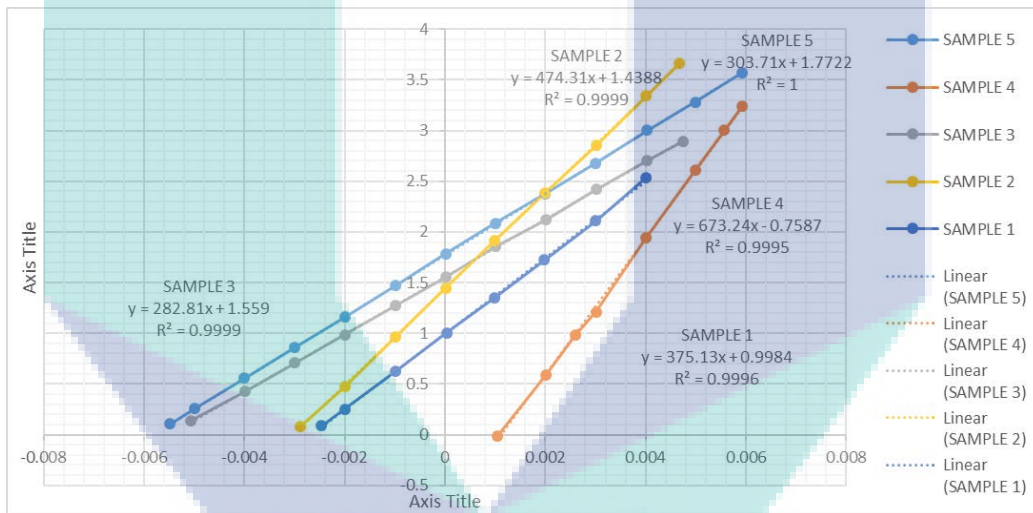
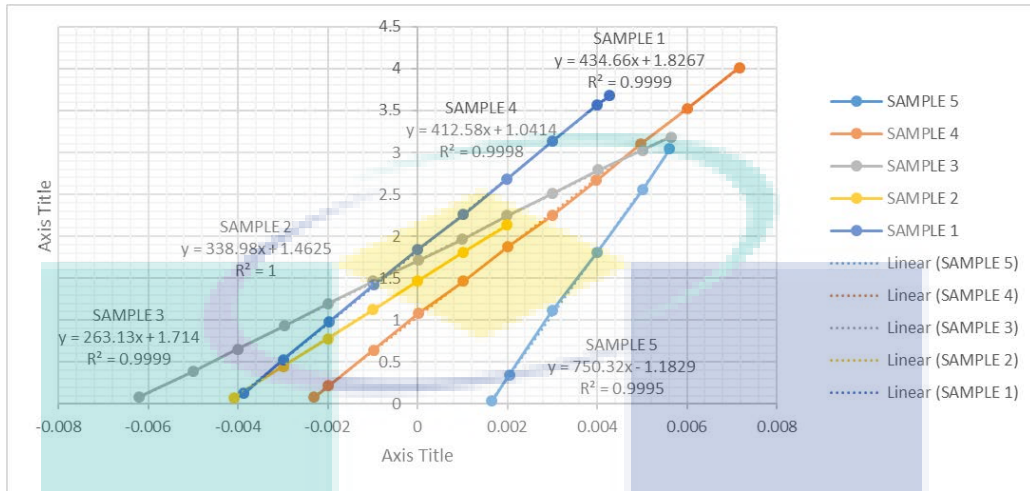
The logo for UIMP (University of Management and Information Technology) is a shield-shaped emblem. It features a yellow diamond at the top, a white vertical stripe in the center, and a teal and blue color scheme on the sides and bottom. The letters 'UIMP' are prominently displayed in white at the base of the shield.

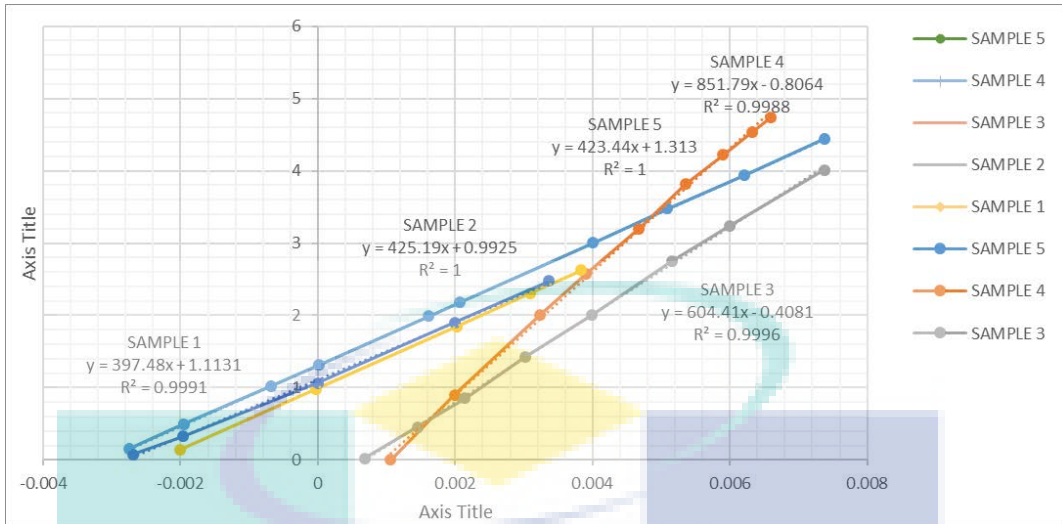
UIMP

**APPENDIX B**  
**ANKLE FOOT ORTHOSIS PROTOTYPE DIMENSIONS**



## APPENDIX C MODULUS OF ELASTICITY – FILAMENT THICKNESS A



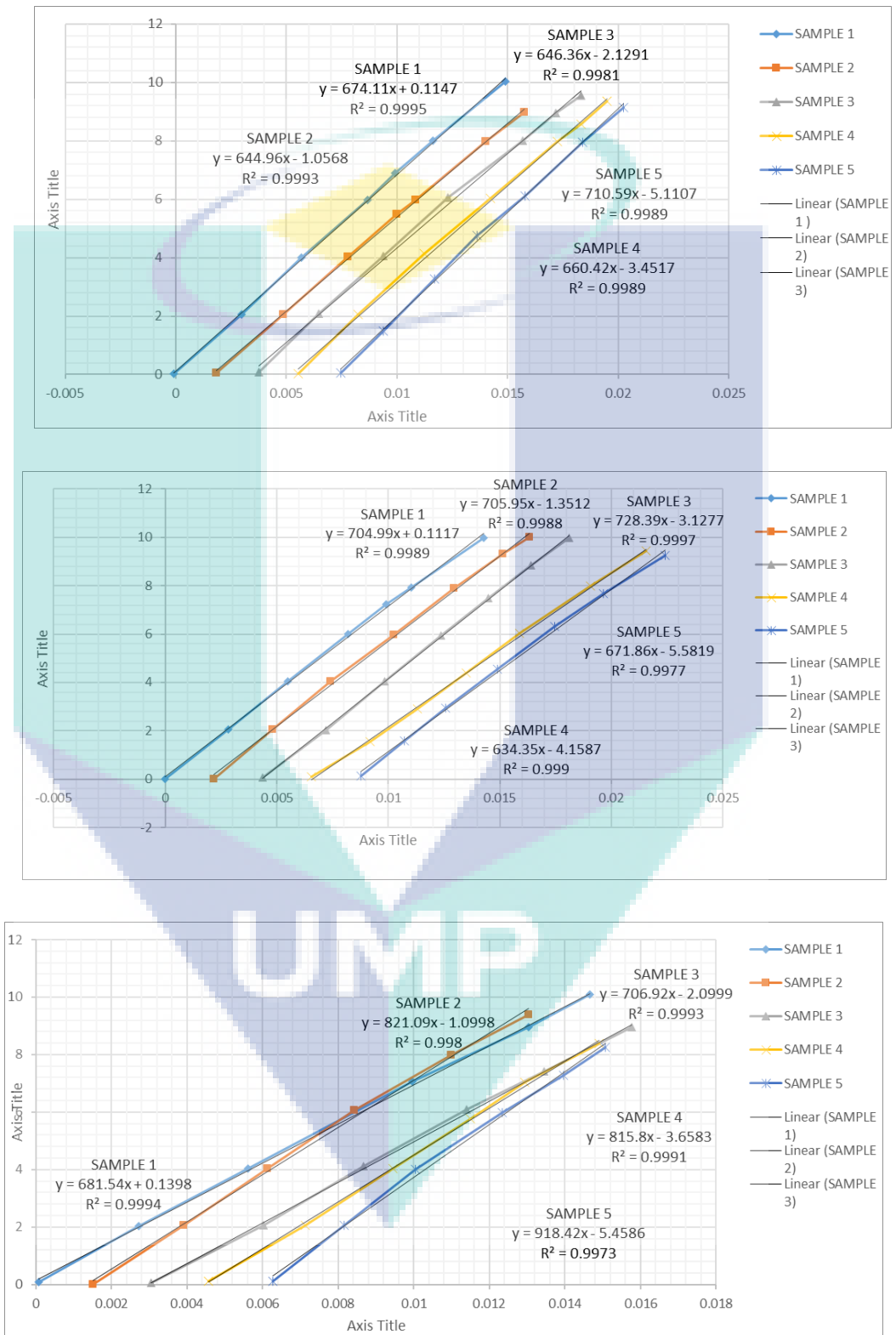


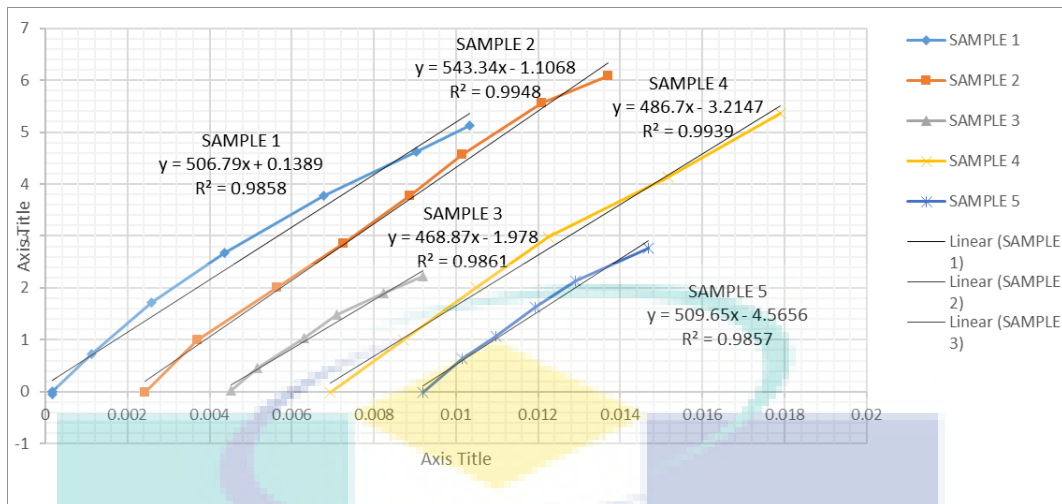
UMP



## APPENDIX C

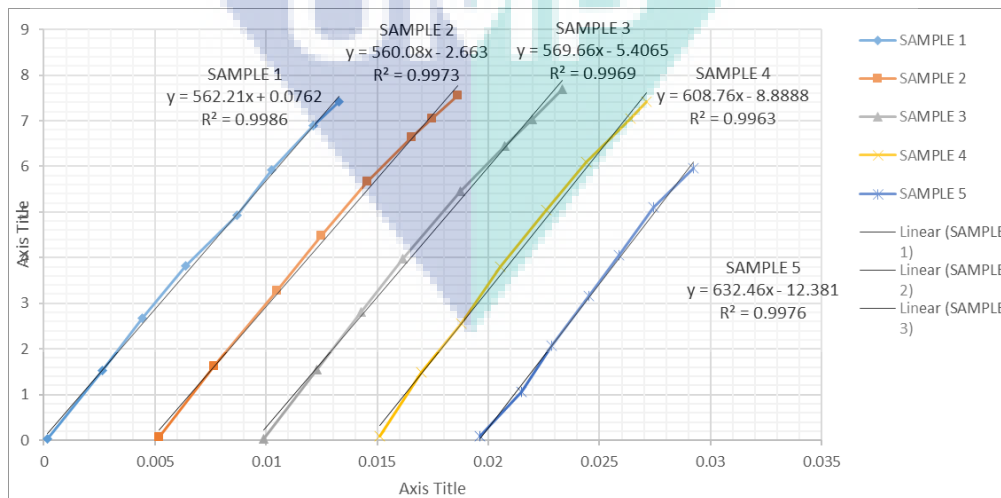
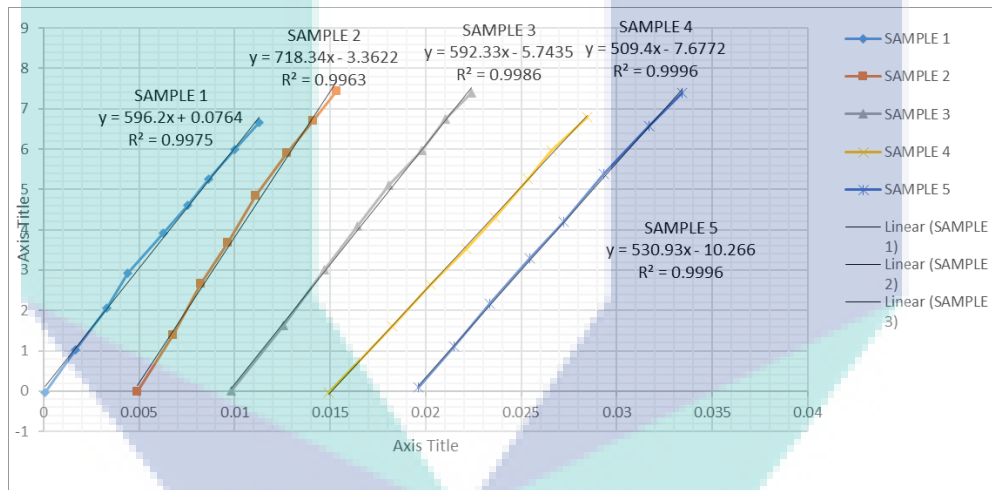
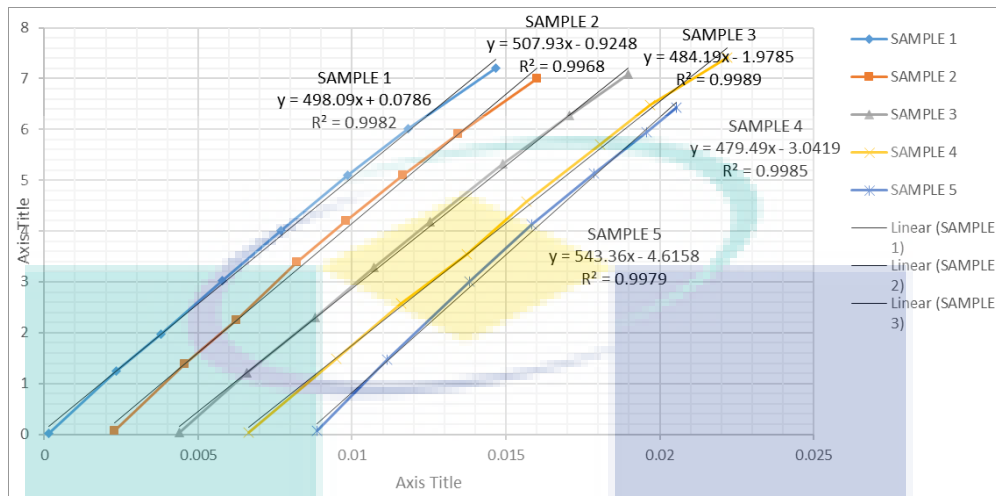
### MODULUS OF ELASTICITY – FILAMENT THICKNESS B

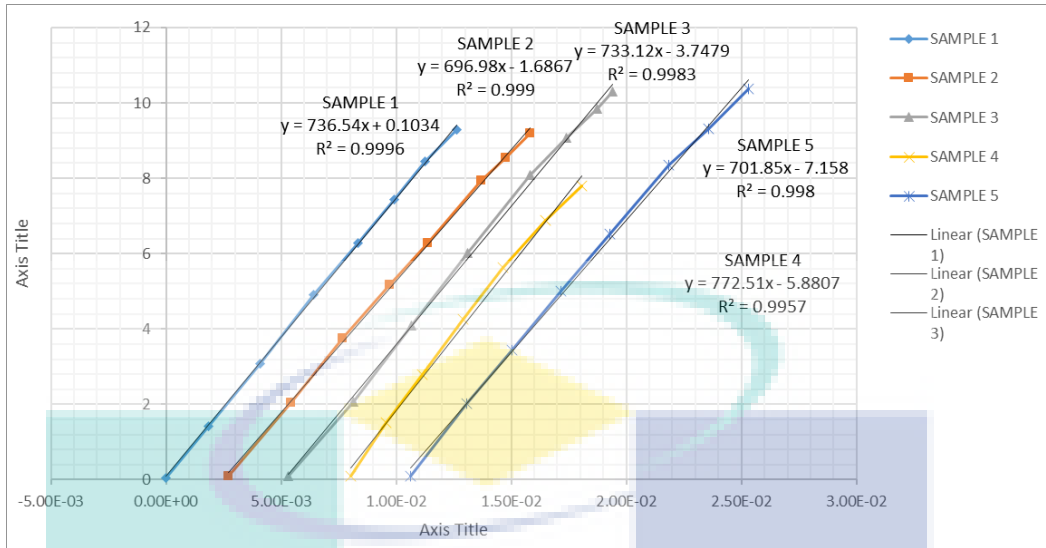




UMP

## APPENDIX D MODULUS OF ELASTICITY – FILAMENT THICKNESS C





UMP